HAL
open science

Fluid-structure interaction problems involving deformable membranes : application to blood flows at macroscopic and microscopic scales

Julien Sigüenza

▶ To cite this version:

Julien Sigüenza. Fluid-structure interaction problems involving deformable membranes : application to blood flows at macroscopic and microscopic scales. Human health and pathology. Université Montpellier, 2016. English. NNT : 2016MONTT301 . hal-01487308v2

HAL Id: hal-01487308
https://theses.hal.science/hal-01487308v2

Submitted on 5 Jun 2018

HAL is a multi-disciplinary open access archive for the deposit and dissemination of scientific research documents, whether they are published or not. The documents may come from teaching and research institutions in France or abroad, or from public or private research centers.

L'archive ouverte pluridisciplinaire **HAL**, est destinée au dépôt et à la diffusion de documents scientifiques de niveau recherche, publiés ou non, émanant des établissements d'enseignement et de recherche français ou étrangers, des laboratoires publics ou privés.

THÈSE

Pour obtenir le grade de

Docteur

Délivré par l'**Université de Montpellier**

Préparée au sein de l'école doctorale **I2S**
Et de l'unité de recherche **IMAG**

Spécialité: **Mathématiques et Modélisation**

Présentée par **Julien Sigüenza**

Fluid-structure interaction problems involving deformable membranes: application to blood flows at macroscopic and microscopic scales

Soutenue le 14 novembre 2016 devant le jury composé de

Franck Nicoud	IMAG - Univ. de Montpellier	Directeur
Simon Mendez	IMAG CNRS - Univ. de Montpellier	Co-encadrant
Valérie Deplano	IRPHE - Marseille	Rapporteur
Jean-Frédéric Gerbeau	INRIA - Paris	Rapporteur
Patrick Segers	Ghent University - Belgique	Président du jury
Vincent Moureau	CORIA CNRS - Rouen	Examinateur
Damien Isèbe	Horiba Medical SAS - Montpellier	Invité

Abstract

This thesis deals with several scientific aspects inherent to the numerical simulation of fluid-structure interaction problems involving thin deformable membranes. Two specific cases relevant to cardiovascular biomechanics are considered: the interaction of the blood flow with the aortic valve (which occurs at the macroscopic scale), and the interaction of the red blood cells membrane with its inner and outer fluids (which occurs at the microscopic scale). In both cases, the fluid-structure interaction coupling is handled using an immersed boundary formalism, representing the membrane by a Lagrangian mesh moving through an Eulerian fluid mesh.

When dealing with red blood cells dynamics, the membrane is considered to be an infinitely thin and massless structure. The first question which is addressed in the present thesis work is how to model the complex microstructure of the red blood cells membrane. A possible way to characterize a suitable membrane model is to simulate the optical tweezers experiment, which is a well-controlled experimental configuration enabling to study the individual mechanics of an isolated red blood cell in a large range of deformation. Some relevant membrane models are identified, but the deformation characteristics measured during the optical tweezers experiment reveal to be not selective enough to be used in a validation context. Additional deformation measurements are proposed, which could allow a better characterization of the red blood cell membrane mechanics.

Regarding the macroscopic configurations, an innovative numerical method is proposed to handle numerical simulations of 3D continuum membranes, still within the immersed boundary formalism. In this method, called immersed thick boundary method, the membrane has a finite thickness. The accuracy and robustness of the method are demonstrated through a variety of well-chosen test cases. Then, the proposed method is applied to a realistic fluid-structure interaction problem, namely the interaction of a pulsatile (blood) flow with a biomimetic aortic valve. A combined experimental and numerical study is led, showing that the method is able to capture the global dynamics of the valve, as well as the main features of the flow downstream of the valve.

All the developments were performed within the YALES2BIO solver (http://www.math.univ-montp2.fr/~yales2bio/) developed at IMAG, which is thus available for further improvements, validations and applicative studies.

Keywords: Fluid-structure interaction, Membranes, Immersed boundary method, Blood flows, Red blood cells, Aortic valve.

Résumé

Cette thèse traite plusieurs aspects scientifiques inhérents à la simulation numérique de problèmes d'interaction fluide-structure impliquant de fines membranes déformables. Deux cas spécifiques relatifs à la biomécanique cardiovasculaire sont considérés : l'interaction de l'écoulement sanguin avec la valve aortique (qui se produit à l'échelle macroscopique), et l'interaction de la membrane des globules rouges avec ses fluides interne et externe (qui se produit à l'échelle microscopique). Dans les deux cas, le couplage fluide-structure est géré par l'intermédiaire d'un formalisme de frontières immergées, en représentant la membrane par un maillage Lagrangien se mouvant au travers d'un maillage fluide Eulérien.

Lorsque l'on traite la dynamique des globules rouges, la membrane est considérée comme étant une structure sans masse et infiniment fine. La première question à laquelle on s'intéresse dans cette thèse est la manière de modéliser la microstructure complexe de la membrane des globules rouges. Un moyen possible pour caractériser un modèle de membrane adapté est de simuler l'expérience des pinces optiques, qui consiste en une configuration expérimentale bien controlée qui permet d'étudier la mécanique individuelle d'un globule rouge isolé dans une large gamme de déformations. Plusieurs modèles pertinents sont identifiés, mais les caractéristiques de déformation mesurées durant l'expérience des pinces optiques se révèlent n'être pas assez sélectives pour être utilisées dans un contexte de validation. Des mesures de déformation additionnelles sont proposées, qui pourraient permettre une meilleure caractérisation de la mécanique de la membrane des globules rouges.

En ce qui concerne les configurations macroscopiques, une méthode numérique innovante est proposée afin de gérer des simulations numériques de membranes 3D continues, en conservant le formalisme de frontières immergées. Dans cette méthode, appelée méthode des frontières immergées épaisses, la membrane a une épaisseur finie. La précision et la robustesse de la méthode sont démontrées par l'intermédiaire d'une variété de cas tests bien choisis. La méthode proposée est ensuite appliquée à un problème d'interaction fluide-structure réaliste, à savoir l'interaction d'un écoulement (sanguin) pulsé avec une valve aortique biomimétique. Une étude combinée expérimentale et numérique est menée, montrant que la méthode est capable de capturer la dynamique globale de la valve, ainsi que les principales caractéristiques de l'écoulement en aval de la valve.

Tous les développements ont été effectués dans le solveur YALES2BIO (http://www.math.univ-montp2.fr/~yales2bio/) développé à l'IMAG, qui est donc disponible pour toutes autres améliorations, validations et études applicatives.

Mots clefs : Interaction fluide-structure, Membranes, Méthode des frontières immergées, Écoulements sanguins, Globules rouges, Valve aortique.

Acknowledgements

Remerciements

Je souhaiterais en premier lieu remercier les acteurs qui ont rendu cette thèse possible. L'entreprise Horiba Medical, à travers le projet DAT@DIAG, ainsi que l'organisme BPIFrance. Un grand merci également au Labex Numev, au CINES, et bien évidemment à l'Institut Montpelliérain Alexander Grothendieck et l'Université de Montpellier.

Je remercie également les membres de mon jury de thèse : Vincent Moureau, Patrick Segers, Damien Isèbe, et plus particulièrement Valérie Deplano et Jean-Frédéric Gerbeau qui ont accepté la lourde tâche de rapporter mon travail de thèse. C'est un trés grand honneur que ces chercheurs et professionnels de haut niveau me font de juger mon travail.

Je souhaite à présent remercier tous ceux qui ont contribué à faire de moi le scientifique que je suis aujourd'hui. Mes premières pensées vont bien entendu vers mes deux encadrants de thèse, mes deux mentors : Franck Nicoud et Simon Mendez. Je ne trouve même pas les mots pour exprimer la gratitude que j'ai envers eux, tant ils m'ont apporté et appris. Ce sont deux personnes que je porte trés haut dans mon estime, autant sur le plan scientifique que sur le plan humain. Le désir de les satisfaire et d'être à la hauteur de leurs exigences a été un moteur considérable pour moi, et pour cela un grand merci à eux. Je tiens également à remercier deux personnes qui ont joué un rôle prépondérant lors de mon ascension vers ce titre de docteur : Christophe Chnafa et Damien Isèbe. Ils ont su me guider lorsque je n'étais encore qu'un "jeune et insouciant" étudiant d'école d'ingénieur, et constituent à mes yeux des exemples de réussite que j'ai toujours cherché à suivre jusqu'à aujourd'hui.

Un grand merci également à tous ceux avec qui j'ai eu la chance de collaborer durant cette thèse. Je pense en premier lieu aux actuels et anciens membres de l'équipe YALES2BIO : Franck Nicoud, Simon Mendez, Christophe Chnafa, Étienne Gibaud, Marco Martins Afonso, Vladeta Zmijanovic, Rebecca Contal, Anthony Larroque, Rodrigo Méndez, Stephanie Lindsey, Thomas Puiseux, Pierre Taraconat, Thierry Mignon, Rajnesh Lal et Bijan Mohammadi. L'équipe LMGC90 : Frédéric Dubois, Dominique Ambard, Rémy Mozul et Franck Jourdan, qui ont grandement participé à l'aboutissement de ce travail de thèse. Nos camarades allemands du Helmholtz Institute : Désirée Pott, Simon Sonntag et Ulrich Steinseifer, avec qui nous avons mené une fructueuse collaboration. Nos amis du CBS : Manouk Abkarian et Luca Lanotte, qui m'ont fait bénéficier de leur expertise sur les globules rouges. Je remercie également la team Sim&Cure, et plus particulièrement Mathieu Sanchez, co-fondateur de cette startup innovante que j'ai vu grandir durant ma thèse, et dont j'ai la chance de faire aujourd'hui partie.

Je remercie à présent l'ensemble des membres de l'IMAG avec qui j'ai partagé mon quotidien professionnel et personnel durant ces trois années. Le pense tout d'abord à Christophe et Étienne, et au trio magique que l'on formait lorsque l'on partageait le même bureau : la Chnaf', la Gib' et la Sig'. J'ai vraiment passé des moments inoubliables avec eux, entre les dilemmes loufoques d'Étienne et les histoires toujours plus improbables de Christophe. J'ai également une pensée particulière pour les autres membres de l'équipe YALES2BIO avec qui j'ai eu l'occasion de construire de réels liens d'amitié : Rodrigo, Stéphanie, Thomas, Pierre, Anthony et Rebecca. J'aimerais également exprimer toute ma gratitude à l'ensemble des doctorants, parmi lesquels j'ai fait des rencontres formidables : Vincent, Yousri, Julien, Guillaume, Antoine, Myriam, Gautier, Joubine, Coralie, Christian, Mickael, Florent, Michele (spéciale dédicace pour vous deux les gars, je n'oublierai pas nos petites aventures crêtoises). La liste est encore longue, je ne les citerai donc pas tous, mais j'ai vraiment apprécié partager cette expérience de thèse avec chacun d'entre eux. Je remercie également l'ensemble des chercheurs que j'ai eu la chance de cotoyer, particulièrement Vanessa et Mathieu. J'ai également une pensée pour les nombreux stagiaires qui sont venus séjourner au labo, et avec qui j'ai toujours eu un grand plaisir à échanger et partager. Je remercie enfin l'ensemble du personnel technique et administratif, notamment Bernadette et Baptiste qui m'ont impressionné de par leur capacité à me porter assistance.

C'est à présent ma famille que je souhaite remercier du plus profond de mon coeur. Ils ont toujours cru en moi, et les savoir fiers de moi aujourd'hui constitue ma plus grande source de satisfaction. Merci à ma mère pour les valeurs qu'elle m'a inculquées au cours de mon éducation, et qui font de moi la personne que je suis aujourd'hui. Merci à mon père qui m'a toujours poussé à donner le meilleur de moi même. Merci également à mon frérot ainsi qu'à ma petite Mamie pour le soutien sans faille qu'ils m'ont apporté.

Je remercie également mes amis proches qui m'ont souvent permis de me sortir du quotidien parfois usant de la thèse. Je pense particulièrement à Hélian, Alain, Johan, Max, Jessyca, Adeline, Seb, Samantha, Guillaume, Étienne et Christophe. Sans eux je ne serais certainement pas allé jusqu'au bout de cette expérience éprouvante.

Et pour finir je tiens à remercier ma moitié, ma chérie, mon amour : Mélanie. Elle n'a cessé de me répéter qu'elle croyait en moi dans les moments de doute, et la rencontrer est certainement la meilleure chose qui me soit arrivée dans ma vie.

Montpellier, le 14 novembre 2016 J. S.

Contents

Abstract (English/Français) **iii**

Acknowledgements **vii**

Contents **x**

Chapter 1 Introduction **1**
1.1 Motivations . . . 2
1.1.1 The cardiovascular system . . . 2
1.1.2 Blood description . . . 9
1.1.3 Scientific challenges . . . 10
1.2 Numerical methods for fluid-structure interaction . . . 13
1.3 The YALES2 flow solver . . . 15
1.3.1 Numerical method . . . 15
1.3.2 Turbulence modeling . . . 18
1.3.3 Validation test case . . . 20
1.4 From YALES2 to YALES2BIO . . . 24
1.5 Chapters contents . . . 27

Chapter 2 Red blood cells modeling **29**
2.1 Introduction . . . 30
2.2 Numerical method . . . 31
2.2.1 Membrane forces computation . . . 32
2.2.2 Navier-Stokes equations solver . . . 34
2.3 Optical tweezers modeling . . . 34
2.3.1 Computational setup . . . 35
2.3.2 Validation . . . 36
2.4 Influence of the membrane modeling . . . 39
2.4.1 Comparison of axial and transverse diameters . . . 40
2.4.2 Characterization of the RBC shape . . . 40
2.4.3 Area variations . . . 42
2.5 Discussion . . . 43

Chapter 3 The immersed thick boundary method **45**
3.1 Introduction . . . 47
3.2 Numerical method . . . 48
3.2.1 Computation of the mechanical force . . . 49
3.2.2 Forces regularization . . . 51
3.2.3 Navier-Stokes equations resolution . . . 55
3.2.4 Membrane convection . . . 55
3.2.5 Discretization . . . 55

3.2.6 Volume correction 55
3.3 Verification and validation 58
3.3.1 Non-linear bending of an elastic plate 58
3.3.2 Inflation of a spherical capsule 61
3.3.3 Capsule in a linear shear flow 64
3.3.4 Red blood cell stretched by optical tweezers 66
3.3.5 Flow-induced vibration of an elastic beam behind a cylinder . 68
3.4 Application: flow through an aortic valve 76
3.5 Conclusion 78

Chapter 4 Application to aortic valve computation 81
4.1 Introduction 82
4.2 Materials and Methods 83
4.2.1 Numerical method 83
4.2.2 Experimental setup 85
4.2.3 Computational setup 88
4.3 Results 89
4.3.1 Valve dynamics 89
4.3.2 Leaflets stress distribution 92
4.3.3 Flow dynamics 93
4.4 Discussion 97
4.5 Supplementary material 98
4.5.1 Overall PIV-vs-CFD comparison 98
4.5.2 Transvalvular pressure gradient 104

Chapter 5 Conclusion 107
5.1 Red blood cells modeling 107
5.2 The immersed thick boundary method 108
5.2.1 Aortic valve computation 109
5.2.2 Perspectives 110

Bibliography 113

Chapter 1

Introduction

Chapter contents

1.1 Motivations 2
1.1.1 The cardiovascular system 2
1.1.2 Blood description 9
1.1.3 Scientific challenges 10
1.2 Numerical methods for fluid-structure interaction 13
1.3 The YALES2 flow solver 15
1.3.1 Numerical method 15
1.3.2 Turbulence modeling 18
1.3.3 Validation test case 20
1.4 From YALES2 to YALES2BIO 24
1.5 Chapters contents 27

This thesis attempts to treat the complex subject entitled:

Fluid-structure interaction problems...
Interactions of some movable or deformable elastic structure with an internal or surrounding fluid flow.

...involving deformable membranes:...
The deformable elastic structures that are considered are membranes (i.e. structures having a very small thickness).

...application to blood flows...
The fluid flows that are considered are blood flows (e.g. the circulation of the blood in the cardiovascular system).

...at macroscopic and microscopic scales
Fluid-structure interactions are investigated at both macroscopic (blood flow interacting with heart valves) and microscopic (blood cells interacting with their carrying fluid flow) scales.

This introductory chapter first aims at motivating the subject of this thesis. An introduction to the cardiovascular system is first provided, before going deeper into the blood constitution. This is a way to introduce the objects of interest of the present thesis, that are the subject of fluid-structure interaction (FSI) problems which involve deformable membranes:

- The aortic valve, whose the leaflets interact with the blood flow, at the macroscopic scale.
- The red blood cells, whose the membrane interacts with both the carrying and internal fluids, at the microscopic scale.

The scientific challenges behind these FSI problems are explained, attempting to highlight the interest of the numerical simulation to address these challenges. This is followed by a short review of the different existing FSI numerical methods. Then the YALES2 flow solver is introduced, which constitutes the basis of this thesis work. The numerical method is briefly described, and a basic test case is presented to illustrate the operation of the solver. Finally, the strategy employed to integrate within the YALES2 solver the possibility to perform FSI simulations of flowing red blood cells is presented. This is the opportunity to introduce the YALES2BIO solver, which is strongly based on YALES2.

1.1 Motivations

1.1.1 The cardiovascular system

The blood is continuously circulating in the cardiovascular system thanks to the heart which acts as a pump. The human heart consists of four chambers split into two sides: the left and right sides, each having an upper chamber (atrium) and lower chamber (ventricle) (see Fig. 1.1). The cardiovascular system can be seen as a closed loop composed of two distinct but linked circuits: the pulmonary and systemic circuits (see Fig. 1.1). The right side of the heart pumps the oxygen-poor blood (parts in blue in Fig. 1.1) into the pulmonary circuit, which returns to the left side of the heart after oxygenation to be pumped into the systemic circuit for oxygenation of the body tissues (parts in red in Fig. 1.1). The cardiac cycle comprises two phases:

- The systole, during which the heart contracts and ejects the blood. At rest, it lasts in average one third of the whole cardiac cycle.
- The diastole, during which the heart relaxes and refills with blood following systole.

The unidirectional circulation of the blood through the cardiovascular system is ensured by the heart valves, which are all made of a very thin biological tissue (membrane) which interacts with the blood flow, alternatively opening and closing during the blood circulation. Figure 1.2 shows a top view of the four heart valves:

- The tricuspid valve, which separates the right atrium from the right ventricle.
- The mitral valve, which separates the left atrium from the left ventricle.
- The aortic valve, which separates the left ventricle from the aorta.
- And the pulmonary valve, which separates the right ventricle from the pulmonary artery.

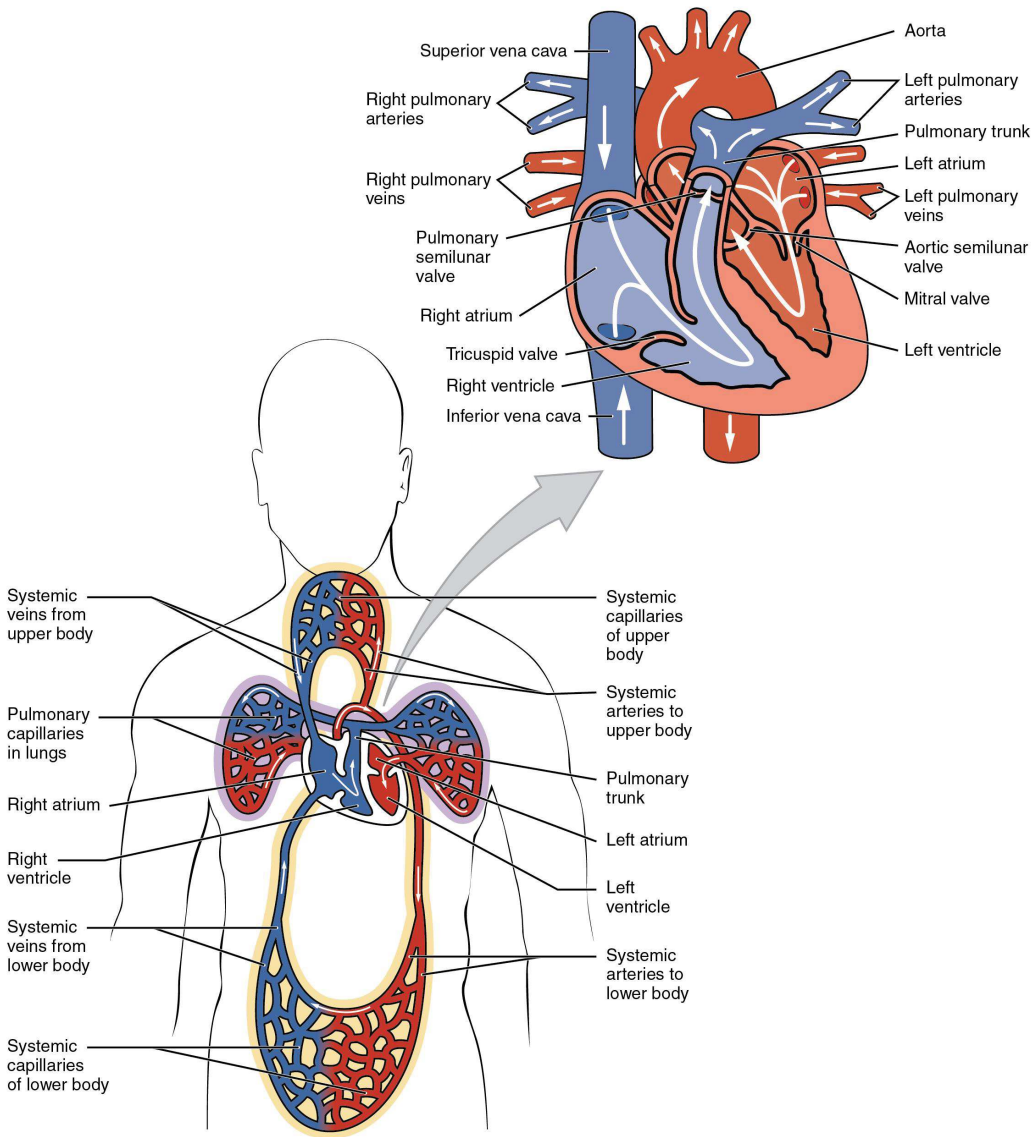

Figure 1.1: Sketch of the cardiovascular system and human heart (image from [16]).

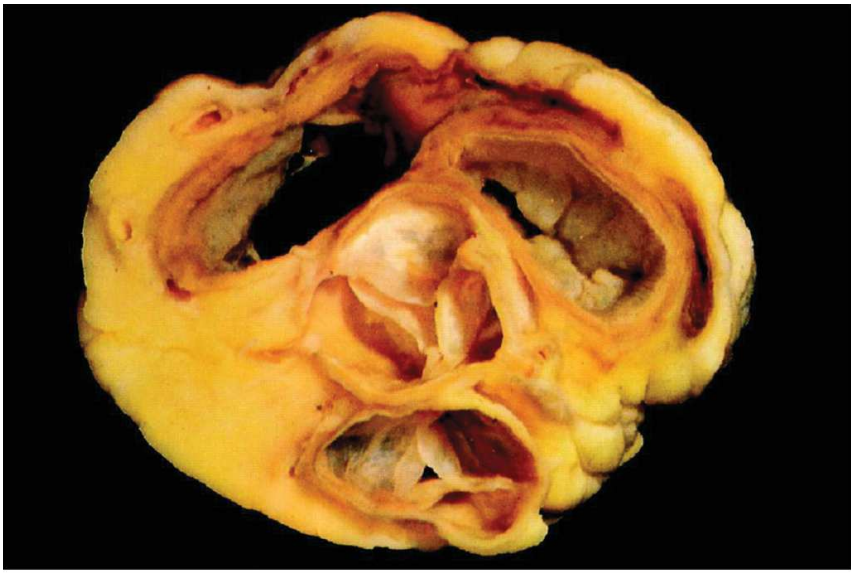

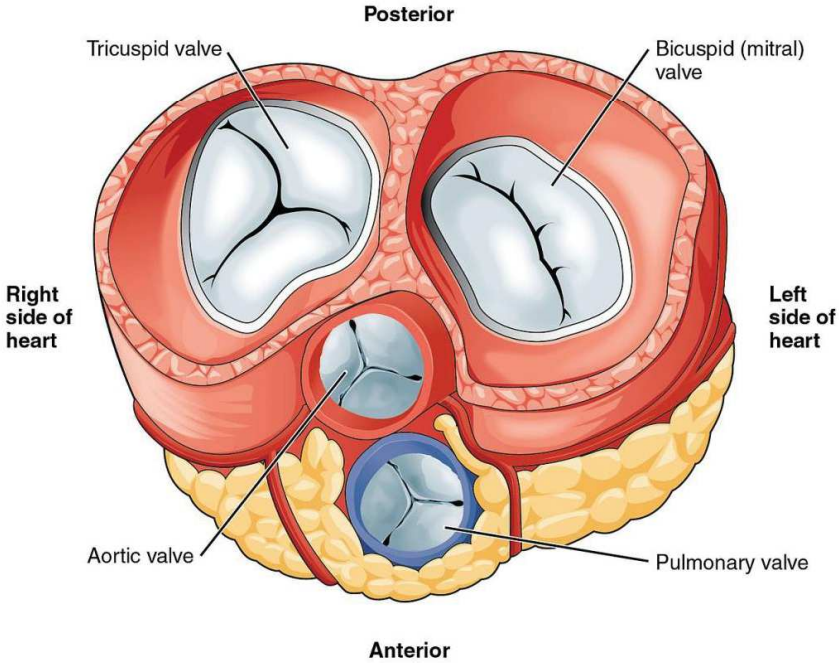

Figure 1.2: Top view of the four heart valves (top, image from [133]), with schematic representation (bottom, image from http://teachmeanatomy.info).

The aortic valve

The aortic valve thus forms the anatomic boundary between the left ventricle and the aorta, and is integrated in the aortic root. Figure 1.3 (top view) shows a sketch of the aortic root structures after longitudinal opening of the root. First, it is seen that the aortic root is composed of three almost symmetrical bulges, called sinuses of Valsalva. Two of the sinuses give rise to the coronary arteries, which irrigate the heart muscle. The central structures of the aortic valve are the three semilunar leaflets: the left coronary leaflet, the right coronary leaflet, and the non-coronary leaflet. Four layers of tissue can be identified within the valve leaflets: arterialis, fibrosa, spongiosa, and ventricularis (see Fig. 1.3, bottom view).

At each contraction of the heart, the stroke volume contained in the left ventricle is pumped through the aortic valve into the aorta, delivering oxygenated blood to the rest of the body. Figure 1.4 (first column) illustrates the flow conditions through the aortic valve (in terms of aortic pressure (AP), left ventricular pressure (LVP), and flow rate) observed in the healthy individual.

The opening/closing mechanism of the aortic valve can be better understood by considering the pressure conditions at both the ventricular and aortic sides of the valve. During the diastole, the aortic pressure (typically around 80 mmHg) is higher than the ventricular pressure (typically around 0 mmHg). There is thus a transvalvular pressure gradient (TPG)[1] of about -80 mmHg acting from the aortic side on the aortic valve, which is tightly closed to prevent blood flowing back into the left ventricle. During the heart contraction, the pressure in the ventricle increases until the TPG becomes positive (the ventricular pressure becomes higher than the aortic pressure), thus leading to the aortic valve opening. Then, both ventricular and aortic pressures increase (typically until 120 mmHg) as the stroke volume is driven into the aorta. Finally once the heart starts relaxing at the beginning of the diastole, the ventricular pressure decreases and the TPG reverses again, leading to the valve closure. It is interesting to note that if the aortic valve can resist to negative TPG of about 80 mmHg without valve regurgitation, the TPG required to drive the blood through the aortic valve is of the order of only few mmHg.

In some cases, the aortic valve tissue degenerates, leading to the calcification of the valve (see Fig. 1.5). This tissue degeneration may cause either a narrowing of the valve (stenosis) or a poor closure of the valve (insufficiency), or eventually both. In the case of aortic valve stenosis, the reduced orifice area of the valve is characterized by a higher resistance to forward flow, which results in an increase of the systolic ventricular pressure and a slight decrease of the systolic aortic pressure (see Fig. 1.4, second column). The systolic TPG is thus drastically increased, meaning that the heart has to provide more energy to drive the blood flow through the aortic valve. The narrowing of the valve orifice also induces higher velocities downstream

[1] The transvalvular pressure gradient is defined as being TPG=LVP−AP. Note that the quantity which is measured in practice by medical doctors is a pressure difference, but is commonly called pressure gradient, and is expressed in mmHg.

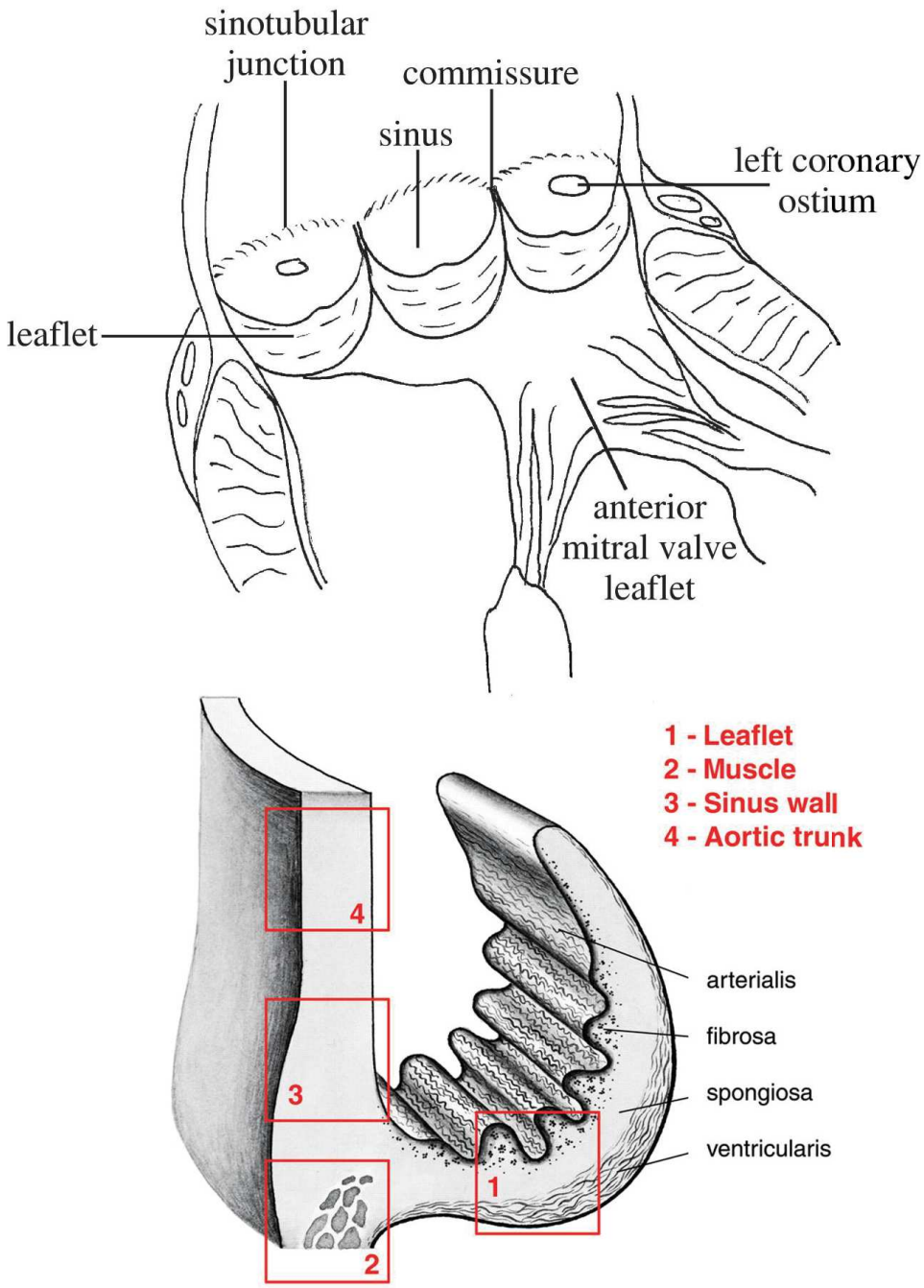

Figure 1.3: Sketch of the aortic root structures after longitudinal opening of the root (top, image from [133]) and of the valve leaflets microstructure (bottom, image from [167]).

of the valve, which may lead to turbulence. In the case of aortic valve insufficiency, the valve is not able to close properly, and valve leakage is thus observed during the diastole (see the flow rate curve in Fig. 1.4, third column). This valve leakage has two implications: 1) because the ventricle is being filled from two sources (aorta and left atrium), the stroke volume ejected by the heart at each contraction is increased, thus leading to higher systolic ventricular and aortic pressures; 2) the valve is no longer able to maintain the diastolic TPG, leading to a decreased diastolic aortic pressure and an increased diastolic ventricular pressure.

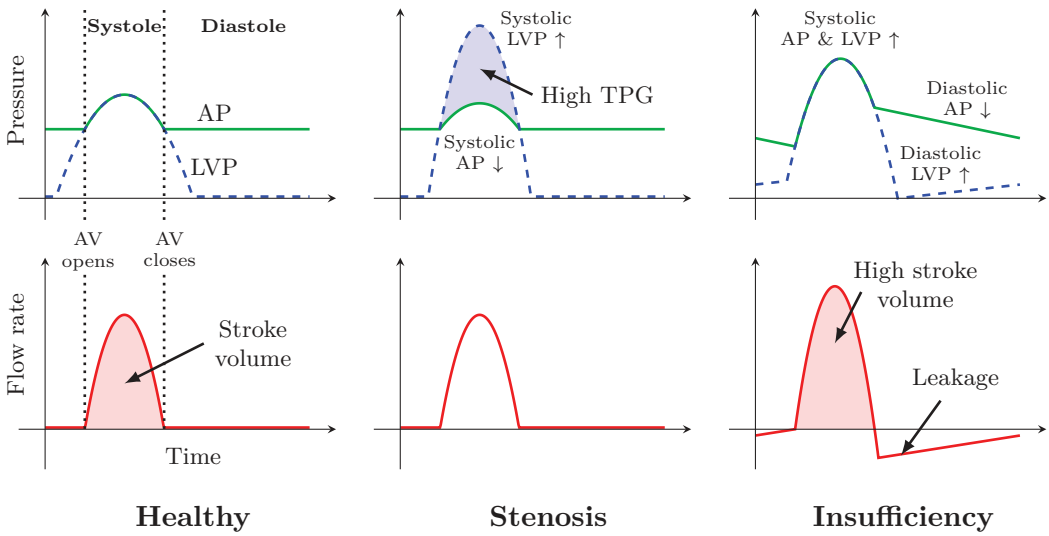

Figure 1.4: Sketch of the aortic pressure (AP), left ventricular pressure (LVP), and flow rate in the case of a healthy aortic valve (first column), aortic valve stenosis (second column), and aortic valve regurgitation (third column).

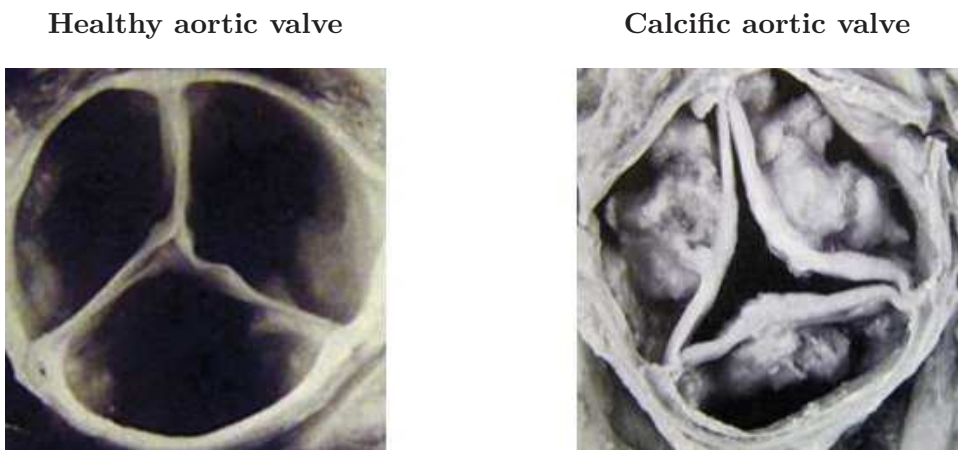

Figure 1.5: Degeneration of the aortic valve tissue, from the healthy aortic valve (left) to the calcific aortic valve (right) (images from http://teomankilic.com).

Aortic valve replacement

These pathologies may have dramatic implications on the life of the patient. Most of the time, the best option is to replace the diseased valve by an artificial valve. There are two main types of artificial valves that can be used for valve replacement, the mechanical and tissue valves. Mechanical valves are designed to replicate the primary function of the natural valve, which is to maintain unimpeded unidirectional flow through the valve. They are characterized by the fact that they are made of rigid parts interacting with the blood flow. The three main types of mechanical valve are the caged-ball, the tilting-disk and the bileaflet valve (see Fig. 1.6). By opposition to the mechanical valves, the tissue valves are made of three deformable leaflets, and are thus closer to the native aortic valve anatomy. They can be either made of a biological tissue (e.g. from a pig heart valve) or engineered tissue (e.g. with polyurethane leaflets) (see Fig. 1.7).

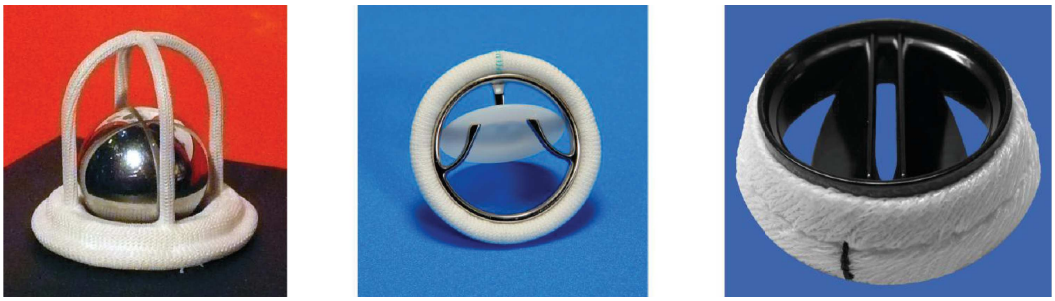

Figure 1.6: Three main types of mechanical valve, from the left to the right: the caged-ball valve, the tilting-disk valve, and the bileaflet valve (images from https://en.wikipedia.org).

Figure 1.7: Two main types of tissue valve: with biological tissue (left, image from http://www.medtronic.com), and with engineered tissue (right, image from http://ejcts.oxfordjournals.org).

Each type of artificial valves has its own drawbacks. Mechanical valves are prone to blood coagulation and require lifelong treatment with anticoagulants. Conversely, tissue valves provide better hemodynamic properties, but have a limited lifespan, lasting in average 15 years before requiring replacement.

1.1.2 Blood description

If the blood can macroscopically be seen as a homogeneous fluid, an observation at the microscopic scale shows that it is actually composed of cellular elements suspended in a carrying fluid (see Fig 1.8, left). An illustration of the blood composition is shown in Fig. 1.8 (right). About 55% of the total blood volume is composed of a fluid called the plasma. This plasma fluid is mainly composed of water (around 92%) in which substances are dissolved or suspended, mostly proteins. The remaining 45% of the blood are the cellular elements, composed of platelets, white blood cells and mostly red blood cells (99% of the cellular elements).

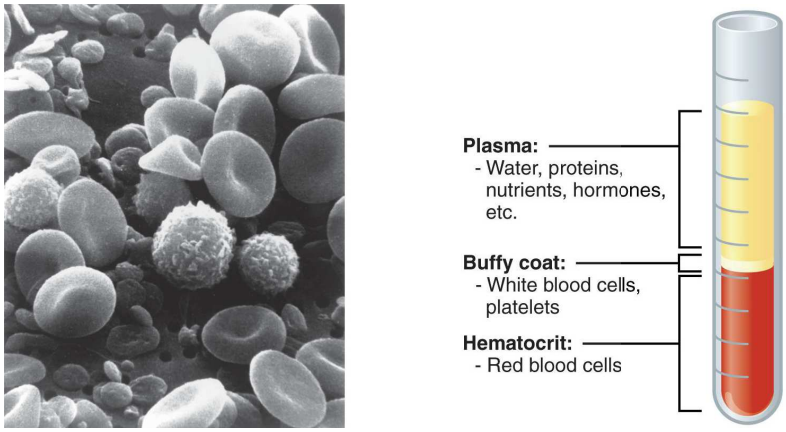

Figure 1.8: Scanning electron microscope image of circulating human blood (left, image from https://en.wikipedia.org), and illustration of the blood composition (right, image from [16]).

The red blood cells

The red blood cells, or erythrocytes, are anucleate cells constituted by a membrane enclosing an internal fluid, the cytoplasm. The cytoplasm contains water and haemoglobin, which is the substance that carries and releases oxygen from the respiratory organs to the rest of the body. At rest, red blood cells have a discocyte shape whose average dimensions were notably measured by Evans and Fung [59] (see Fig. 1.9).

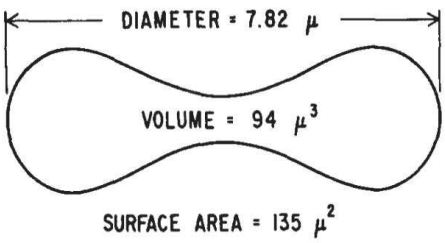

Figure 1.9: Average dimensions of the human red blood cell as reported by Evans and Fung [59] (image from [59]).

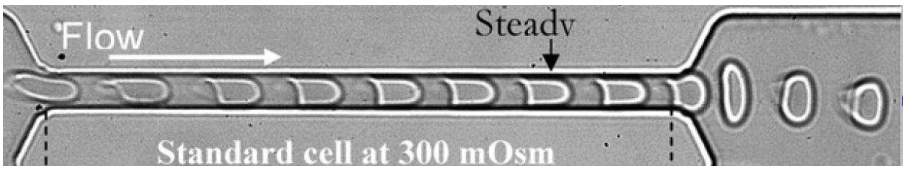

Figure 1.10: Time-lapse sequence of the deformation of a healthy red blood cell in a 5 μm channel (image from [1]).

Red blood cells are subjected to high deformation when passing through the multiple vessels of the cardiovascular system, able to squeeze through capillaries having a diameter more than twice smaller than their characteristic size (as illustrated in Fig. 1.10). This remarkable deformability of the red blood cells has two explanations: 1) their geometrical nature, with a membrane area greater than the one of a sphere with the same volume, resulting in their deflated aspect; 2) the composite structure of the membrane, which confers to the red blood cells very specific mechanical properties. As shown in Fig. 1.11, this structure is composed of a lipid bilayer and an underlying protein network, the cytoskeleton, both linked via embedded transmembrane proteins. These two structures constituting the membrane are responsible for the complex mechanics associated to the deformation of red blood cells:

- The lipid bilayer resists to bending deformation and is quasi-incompressible (highly resists to area-dilatation).
- The cytoskeleton resists to shear deformation and slightly resists to area-dilatation.

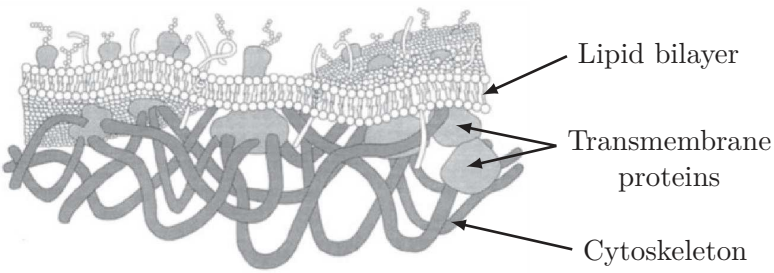

Figure 1.11: Schematic representation of the red blood cell membrane (image from [134]).

1.1.3 Scientific challenges

Aortic valve diseases & replacement

During the cardiac cycle, blood exerts a continuous loading on the aortic valve, which experiences compression, stretching, and bending stresses [164]. Conversely, the interaction of the pulsatile blood flow with the aortic valve gives rise to complex flow structures in the vicinity of the valve (see Fig. 1.12), which could eventually lead to transition to turbulence [176].

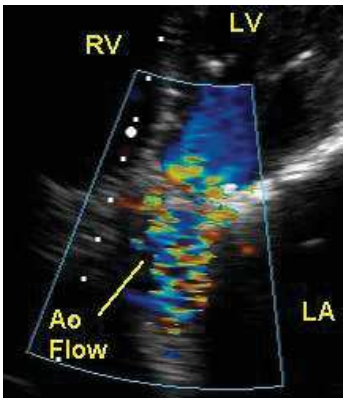

Figure 1.12: Echocardiogram showing complex flow patterns (mosaic color patterns) downstream of a prosthetic aortic valve indicating a turbulent flow (image from https://cardiophile.org.

Assessing these complex structural and flow features could ultimately allow to improve the understanding of the degeneration process leading to aortic valve calcification, but also drastically help the design of artificial aortic valves. Indeed, there are many ex vivo studies which suggest that mechanical factors such as pressure, leaflets tension, and fluid shear stresses play an important role in the activation of the inflammatory pathways leading to the aortic valve calcification [9, 10, 23, 72, 130, 175, 178, 182, 183, 204]. On the other side, it is well known that artificial valve designs should be optimized both in terms of structure and hemodynamics. Mechanical features such as valve durability, pressure drops (systolic TPG), regurgitation volumes, flow turbulence, fluid shear stresses, blood stagnation and flow separation regions have been pointed out as being relevant indicators to evaluate the performances of artificial aortic valves [38, 208].

Hemorheology

It has been shown that the blood is a suspension of cellular elements, mostly red blood cells, carried by a plasma fluid. Red blood cells are responsible for the non-Newtonian behavior of the blood, which is characterized by a shear rate dependence of its viscosity. The hypothesis of blood Newtonian behavior is generally made in large arteries [101], where red blood cells are very small as compared to the characteristic size of the blood vessel. In smaller vessels and in some specific flow configurations like in carotid bifurcation [81], arterial stenosis [192], and abdominal aortic aneurysm [48], the non-Newtonian behavior of the blood is however suspected to play an important role in the hemodynamics. Chien [30] showed that the shear thinning of the blood viscosity can be mainly attributed to the shear-dependent behavior of the red blood cells (see Fig. 1.13): at low shear rate, red blood cells aggregate, leading to a higher apparent viscosity; at high shear rate, red blood cells deform, leading to a lower apparent viscosity. The processes leading to the red blood cells aggregation or deformation are governed by the interaction between the red blood cells and their carrying plasma fluid, which thus appears to be a primary key point for a full understanding of the blood rheology.

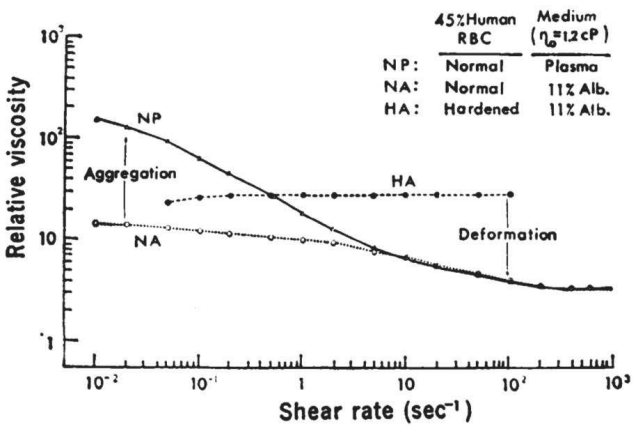

Figure 1.13: Logarithmic relation between viscosity and shear rate in three types of red blood cells suspensions. Viscosity was determined in a coaxial cylinder viscometer (image from [30]).

Medical devices

There are numerous medical devices within which blood is circulating. One can cite among others: ventricular assist devices, extracorporeal circulation and blood analyzers. These medical devices often generate non-physiological flow conditions which may lead to mechanical forces that can cause cell damage, such as hemolysis (rupture of the red blood cell membrane). In blood analyzers for example, the geometries within which the blood circulates are way more singular and complex than the geometry of the blood vessels. Red blood cells are induced to pass through abrupt narrowing, thus experiencing high velocity gradients and extensional deformation (see Fig. 1.14). This points out the extreme necessity to fully control the integrity and the deformation characteristics of the red blood cells when designing medical devices in contact with blood. Again, this requires a complete understanding of the complex interaction between the red blood cells and their carrying fluid (which in the case of medical devices, can be a fluid other than the plasma).

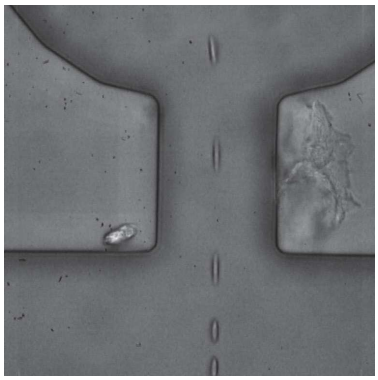

Figure 1.14: Time-lapse sequence of the deformation of a healthy red blood cell passing through an abrupt channel narrowing characteristic from blood analyzer devices (experiment by M. Abkarian, L. Lanotte and D. Isèbe).

Understanding fluid-structure interactions

Understanding the complex FSI problems in which the aortic valve and the red blood cells are involved is thus of major interest. A full understanding of these FSI problems however requires to be able to test a wide variety of flow configurations, with detailed analysis of both structural and flow features. Meeting these requirements is not possible without the use of the numerical simulation. Computational Fluid Dynamics (CFD), for example, has proven to be practical and efficient, and appears to be a reliable tool for investigating blood flow configurations with complex flow patterns, with eventual transitions to turbulence. FSI simulations are however much more challenging than CFD simulations, since they require solving both the structure and the flow, as well as their complex interaction.

1.2 Numerical methods for fluid-structure interaction

Over the last decades, many numerical methods have been developed in order to simulate FSI problems. Hou *et al.* (2012) [90] classified these various approaches into different categories (see Tab. 1.1).

				References
Methods	Monolithic			[93], [129], [163]
	Partitioned	Conforming mesh		[5], [25], [46], [60], [61], [71], [191], [202], [211]
		Non-conforming mesh	Immersed Boundary Method	[150], [151], [152]
			Immersed Domain Method	[118], [119], [195], [196], [197], [209], [210]

Table 1.1: Classification of the different existing FSI numerical methods, by Hou *et al.* (2012) [90].

A first classification can be done between the monolithic approach and the partitioned approach. The monolithic approach treats both the fluid and the solid in the same mathematical framework. The entire problem is formed by a single system of equations which is solved simultaneously by a unified algorithm. Even if this approach can provide better accuracy, its main drawback is that it requires more resources and expertise to develop and maintain such a specialized code. In contrast, the partitioned approach treats the fluid and the solid separately, each physical problem being solved with their respective numerical algorithm. A motivation of this last approach is to integrate avalaible specialized algorithms already validated on fluid or structural problems, thus reducing the code development time.

Another distinction for partitioned FSI methods is based upon the treatment of the meshes: the conforming mesh methods and the non-conforming mesh methods. The conforming mesh methods consider the interface conditions as physical boundary conditions, and require meshes to conform at the interface. The deformation and displacements of the solid structure can thus require frequent re-meshing procedures, which can be very time consuming when dealing with large displacements applications. Most of the recent developments in FSI methods are the non-conforming mesh methods. In this case, the boundary location and the related interface conditions are treated as constraints imposed on the model equations. Non-conforming meshes can then be used, enabling to solve independently the fluid and solid equations with their respective grids, and avoiding time consuming re-meshing. The reader is referred to the work of Fernández and Gerbeau [70] for an extensive description of partitioned FSI algorithms in the context of blood flows, including both conforming and non-conforming meshes.

The two most popular non-conforming mesh methods are known to be the Immersed Boundary Method (IBM) and the Immersed Domain Method (IDM). When using the IBM, the fluid equations are solved with an additional source term, the FSI force, which mimics the action of the immersed boundary on the fluid. The FSI force is calculated from the deformation state of the structure, updated by the surrounding fluid velocity. The IBM has been developed to deal with structures that do not occupy volumes, such as infinitely thin membranes. To represent the interaction between a fluid and a bulk structure, the IDM was introduced. An artificial fluid is defined, which fills the volume of the bulk structure. Then the FSI force is imposed to every grid point in the artificial fluid domain.

Deformable membranes

Both the reduced development time provided by partitioned approaches and the ability of non-conforming mesh methods to handle large displacements of the structure make the immersed boundary method (IBM) very attractive to simulate FSI of deformable membranes. The IBM was originally developed by Peskin [150, 151, 152] to simulate blood flow through the heart and heart valves, and has since been used and adapted in a wide variety of applications, including heart valves dynamics [21, 82, 83, 84, 85, 198] and deformable particles such as capsules, vesicles and red blood cells [6, 7, 8, 53, 99, 107, 108, 109, 206].

Although the IBM appears to be the numerical method that offers the broadest field of application regarding FSI of deformable membranes, other more specific methods can be found in the literature and should be mentioned in the present review. For heart valves simulations, one can cite the fictitious domain method [4, 42, 43, 44, 45, 55], the operator splitting method (similar to the fictitious domain method) implemented in the LS-DYNA commercial software [159, 184, 199, 200], and the immersogeometric FSI methodology developed by Kamensky *et al.* [91, 92, 96]. Also very popular for simulating deformable particles are the boundary integral

methods (BIM) [11, 12, 17, 20, 54, 77, 105, 149, 155, 156, 158, 190, 194, 203, 212, 213] which provide high precision results in Stokes flows, and the particle methods which use dissipative particle dynamics (DPD) [63, 64, 65, 66, 67, 68, 69, 148, 154] or multiparticle collision dynamics (MPC) [125, 126, 144, 145, 146, 147] for multiscale modeling of blood flows.

1.3 The YALES2 flow solver

The YALES2[2] solver is a massively parallel unstructured finite-volume flow solver for incompressible Navier-Stokes equations. Figure 1.15 illustrates the capacities of the YALES2 flow solver, which has initially been developed for solving two-phase combustion on massive complex meshes, from primary atomization to pollutant prediction [139, 140, 141].

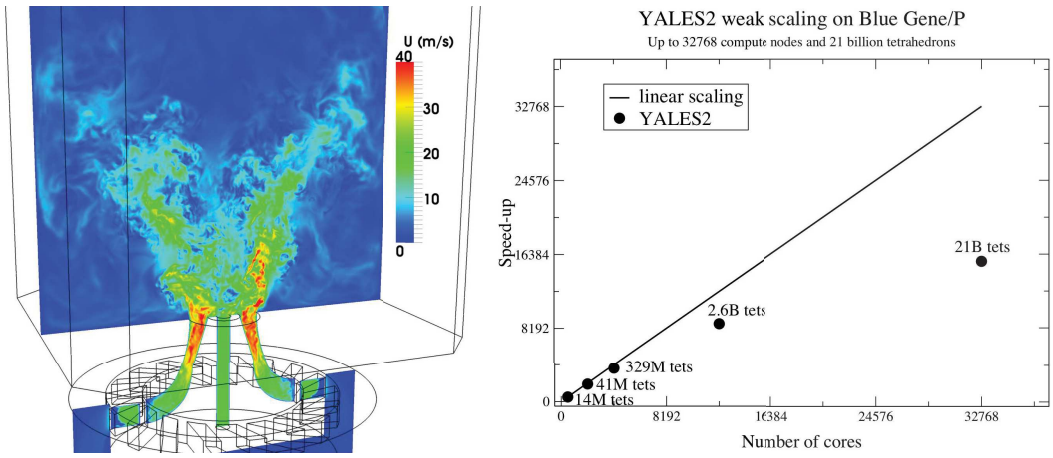

Figure 1.15: Illustration of the capacities of the YALES2 flow solver. Left image shows a simulation of a swirl burner using a mesh of 382 millions tetrahedrons, and right plot shows the scalability of the solver up to 32 768 processors and 21 billion elements (images from https://www.coria-cfd.fr).

1.3.1 Numerical method

In the case of an incompressible flow and assuming a Newtonian fluid, the Navier-Stokes equations and the mass conservation equation read:

$$\begin{cases} \dfrac{\partial \vec{v}}{\partial t} + \vec{\nabla}.(\vec{v} \otimes \vec{v}) = -\dfrac{\vec{\nabla} p}{\rho} + \nu \Delta \vec{v} + \dfrac{\vec{f}}{\rho} \\ \\ \vec{\nabla}.\vec{v} = 0 \end{cases} \tag{1.1}$$

where $\vec{v}$ is the velocity vector, p the pressure, and $\vec{f}$ a possible volumetric force. ρ and ν are the fluid properties, respectively the density and the kinematic viscosity.

[2]YALES2 was developed from 2007 to 2010 by V. Moureau and is maintained since 2011 by V. Moureau and G. Lartigue at CORIA, CNRS UMR 6614. More information can be found here: https://www.coria-cfd.fr/index.php/YALES2.

The projection method

A projection method [37] is used to numerically solve Eq. (1.1). One can write the following time semi-discrete form of Eq. (1.1), considering an Euler explicit scheme:

$$\begin{cases} \dfrac{\overrightarrow{v}^{n+1} - \overrightarrow{v}^{n}}{\Delta t} = -\overrightarrow{\nabla}.\left(\overrightarrow{v}^{n} \otimes \overrightarrow{v}^{n}\right) - \dfrac{\overrightarrow{\nabla} p^{n+1}}{\rho} + \nu \Delta \overrightarrow{v}^{n} + \dfrac{\overrightarrow{f}}{\rho} \\ \\ \overrightarrow{\nabla}.\overrightarrow{v}^{n+1} = 0 \end{cases} \tag{1.2}$$

To advance both the velocity $\overrightarrow{v}^{n+1}$ and the pressure p^{n+1}, the velocity $\overrightarrow{v}^{*}$ is first advanced considering the pressure p^{n} at the previous time step:

$$\frac{\overrightarrow{v}^{*} - \overrightarrow{v}^{n}}{\Delta t} = -\overrightarrow{\nabla}.\left(\overrightarrow{v}^{n} \otimes \overrightarrow{v}^{n}\right) - \frac{\overrightarrow{\nabla} p^{n}}{\rho} + \nu \Delta \overrightarrow{v}^{n} + \frac{\overrightarrow{f}}{\rho} \tag{1.3}$$

This first estimation of the velocity $\overrightarrow{v}^{*}$ is then substracted to the final velocity $\overrightarrow{v}^{n+1}$, which gives:

$$\overrightarrow{v}^{n+1} - \overrightarrow{v}^{*} = -\Delta t \frac{\overrightarrow{\nabla}\left(p^{n+1} - p^{n}\right)}{\rho}. \tag{1.4}$$

Finally, taking the divergence of Eq. (1.4) and applying the mass conservation constraint ($\nabla.\overrightarrow{v}^{n+1} = 0$) leads to:

$$\frac{\Delta\left(p^{n+1} - p^{n}\right)}{\rho} = \frac{\overrightarrow{\nabla}.\overrightarrow{v}^{*}}{\Delta t}. \tag{1.5}$$

The pressure p^{n+1} is thus advanced by solving the Poisson equation of Eq. (1.5), using a Deflated Preconditioned Conjugate Gradient (DPCG) algorithm [123, 140]. The first estimation of the velocity $\overrightarrow{v}^{*}$ is then corrected by the calculated pressure p^{n+1} (using Eq. (1.4)), yielding the final velocity $\overrightarrow{v}^{n+1}$:

$$\overrightarrow{v}^{n+1} = \overrightarrow{v}^{*} - \Delta t \frac{\overrightarrow{\nabla}\left(p^{n+1} - p^{n}\right)}{\rho}. \tag{1.6}$$

Time advancement

The time advancement of the velocity $\overrightarrow{v}^{*}$ is performed using a 4th-order Runge-Kutta scheme in time (RK4)[3] [201]. Rewritting Eq. (1.3) as:

$$\frac{\overrightarrow{v}^{*} - \overrightarrow{v}^{n}}{\Delta t} = f\left(\overrightarrow{v}^{n}, p^{n}\right), \tag{1.7}$$

the velocity $\overrightarrow{v}^{*}$ is advanced such as:

$$\begin{cases} \overrightarrow{v}^{(1)} = \overrightarrow{v}^{n} + \dfrac{1}{4}\Delta t f\left(\overrightarrow{v}^{n}, p^{n}\right), \\ \overrightarrow{v}^{(2)} = \overrightarrow{v}^{n} + \dfrac{1}{3}\Delta t f\left(\overrightarrow{v}^{(1)}, p^{n}\right), \\ \overrightarrow{v}^{(3)} = \overrightarrow{v}^{n} + \dfrac{1}{2}\Delta t f\left(\overrightarrow{v}^{(2)}, p^{n}\right), \\ \overrightarrow{v}^{*} = \overrightarrow{v}^{n} + \Delta t f\left(\overrightarrow{v}^{(3)}, p^{n}\right). \end{cases} \tag{1.8}$$

[3] Note that other time schemes are available in YALES2, such as the TFV4A scheme, but are not presented here.

Finite-volume spatial discretization

The finite-volume method (FVM) is used for the spatial discretization, which is based on the integration of the equations on small polyhedral control volumes, called dual volumes. The definition of the dual volume V_j associated to node j of an unstructured hybrid mesh is illustrated in Fig. 1.16.

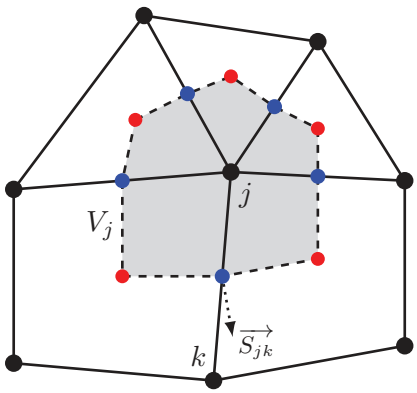

Figure 1.16: Dual volume V_j created around the node j of an unstructured hybrid mesh by linking the centroids of the neighboring elements (red dots) and the centers of the edges containing node j (blue dots).

The integration of a quantity ϕ over the dual volume V_j is expressed as:

$$\phi_{V_j} = \frac{1}{V_j} \int_{V_j} \phi \, dV. \tag{1.9}$$

Integrating the momentum equation over each dual volume V_j gives:

$$\frac{\partial \overrightarrow{v_{V_j}}}{\partial t} - \frac{\overrightarrow{f_{V_j}}}{\rho} = \frac{1}{V_j} \int_{V_j} \overrightarrow{\nabla}. \left[-(\overrightarrow{v} \otimes \overrightarrow{v}) - \frac{p}{\rho} \mathbb{I} + \nu \left(\overline{\overline{\nabla}} \overrightarrow{v} + \overline{\overline{\nabla}} \overrightarrow{v}^T \right) \right] dV, \tag{1.10}$$

where $\mathbb{I}$ is the identity matrix. Using the Green-Ostrogradski theorem, Eq. (1.10) can be written as:

$$\frac{\partial \overrightarrow{v_{V_j}}}{\partial t} - \frac{\overrightarrow{f_{V_j}}}{\rho} = \frac{1}{V_j} \oint_{S_j} \overline{\overline{\psi}}. \overrightarrow{n} \, dS, \tag{1.11}$$

with:

$$\overline{\overline{\psi}} = -(\overrightarrow{v} \otimes \overrightarrow{v}) - \frac{p}{\rho} \mathbb{I} + \nu \left(\overline{\overline{\nabla}} \overrightarrow{v} + \overline{\overline{\nabla}} \overrightarrow{v}^T \right).$$

S_j represents the surface bordering the dual volume V_j and $\overrightarrow{n}$ the vector normal to this surface. The surface integral of the flux $\overline{\overline{\psi}}$ represents a transport of momentum towards neighboring control volumes, and illustrates the conservative nature of the Navier-Stokes equations. The right-hand side of Eq. (1.11) is approximated as follow:

$$\frac{1}{V_j} \oint_{S_j} \overline{\overline{\psi}}. \overrightarrow{n} \, dS = \frac{1}{V_j} \sum_{k \leftrightarrow j} \overline{\overline{\psi_{jk}}} \, . \, \overrightarrow{S_{jk}}, \tag{1.12}$$

where $\overrightarrow{S_{jk}}$ represents the non-normalized vector normal to the surface patch of the dual volume V_j attributed to the pair (j, k), and $\overline{\overline{\psi_{jk}}}$ the flux through this surface

patch, which can be basically expressed as:

$$\overline{\overline{\psi_{jk}}} = \overline{\overline{\psi}}\left(\overrightarrow{v_{jk}}, p_{jk}\right) = \frac{\overline{\overline{\psi}}\left(\overrightarrow{v_{V_j}}, p_{V_j}\right) + \overline{\overline{\psi}}\left(\overrightarrow{v_{V_k}}, p_{V_k}\right)}{2}. \tag{1.13}$$

This expression of the flux $\overline{\overline{\psi_{jk}}}$ makes the scheme second-order accurate for regular meshes, and only first-order accurate for irregular meshes [189], potentially implying important diffusion and dispersion errors. High-order schemes enable to reduce these numerical errors, and are thus generally less dissipative.

A fourth-order and low-dissipative spatial scheme has thus been developed within the YALES2 flow solver. It is based on a deconvolution of the finite-volume integration [122]. Indeed, when using the FVM, the nodal values ϕ_j associated to the quantity ϕ are not directly known, only their integral ϕ_{V_j} over the control volumes V_j are known. The development of a high-order scheme however requires writing this nodal value ϕ_j in an accurate way. The deconvolution thus enables to write the nodal value ϕ_j as a function of the integrated quantity ϕ_{V_j} and its successive derivatives, using a Taylor-series development. The nodal values ϕ_j and ϕ_k are then used to express the value ϕ_{jk} associated to the surface patch of the dual volume V_j attributed to the pair (j, k). The high-order scheme necessitates to pre-calculate the derivatives of ϕ at the nodes, which increases the stencil of the spatial scheme.

1.3.2 Turbulence modeling

In fluid mechanics, the flow is generally characterized by its Reynolds number Re, which is expressed as:

$$Re = \frac{inertial\,forces}{viscous\,forces} = \frac{\rho v L}{\mu}, \tag{1.14}$$

where ρ and μ are respectively the fluid density and dynamic viscosity, v the characteristic velocity, and L the characteristic length. The Reynolds number can be seen as the ratio of the inertial forces to the viscous forces, and consequently quantifies the relative importance of these two types of forces for a given flow configuration.

For large Reynolds number flows (i.e. when the inertial forces are significantly larger than the viscous forces), turbulence may arise, leading to chaotic fluctuations in the velocity/pressure fields. In turbulent flow, unsteady vortices appear at many different scales and interact with each other. Large vortices give rise to smaller vortices until reaching the scale of the smallest vortices, called the Kolmogorov scale.

When aiming to simulate turbulent flows, the most basic approach is to perform Direct Numerical Simulation (DNS). The simulation is performed on a mesh which is sufficiently fine to properly take into account the smallest scales of the flow. This method may however require large computational resources, given that the mesh resolution has to be smaller than the Kolmogorov scale.

An alternative approach is to perform Large Eddy Simulation (LES). This approach consists in filtering the Navier-Stokes equations, so that only the structures

bigger than a certain length (typically, the chosen mesh resolution) are simulated. In this case, the smallest structures are modeled using a subgrid-scale (SGS) model. Thus, the finer the mesh, the larger the range of resolved scales, and the smallest the contribution of the SGS model. Applying the filter operator $\overline{[.]}$ to Eq. (1.1) leads to[4]:

$$\begin{cases} \dfrac{\partial \overline{[\vec{v}]}}{\partial t} + \vec{\nabla}.\overline{[\vec{v} \otimes \vec{v}]} = -\dfrac{\vec{\nabla}\overline{[p]}}{\rho} + \nu \Delta \overline{[\vec{v}]} + \dfrac{\vec{f}}{\rho} \\ \vec{\nabla}.\overline{[\vec{v}]} = 0 \end{cases} \tag{1.15}$$

The nonlinear filtered advection term $\overline{[\vec{v} \otimes \vec{v}]}$ is the key point of the LES modeling. It requires knowledge of the unfiltered velocity field, which is unknown and thus needs to be modeled. One can consider the following splitting:

$$\overline{[\vec{v} \otimes \vec{v}]} = \overline{[\vec{v}]} \otimes \overline{[\vec{v}]} - \tau^r, \tag{1.16}$$

where τ^r is the residual-stress tensor which results from the unresolved subgrid-scale contributions, and can be modeled thanks to the eddy-viscosity assumption:

$$\tau^r = \nu_{SGS} \left(\overline{\overline{\nabla}}\, \overline{[\vec{v}]} + \overline{\overline{\nabla}}\, \overline{[\vec{v}]}^T \right), \tag{1.17}$$

where ν_{SGS} is the subgrid-scale kinematic viscosity. Equation (1.15) thus reads:

$$\begin{cases} \dfrac{\partial \overline{[\vec{v}]}}{\partial t} + \vec{\nabla}.\left(\overline{[\vec{v}]} \otimes \overline{[\vec{v}]} \right) = -\dfrac{\vec{\nabla}\overline{[p]}}{\rho} + (\nu + \nu_{SGS}) \Delta \overline{[\vec{v}]} + \dfrac{\vec{f}}{\rho} \\ \vec{\nabla}.\overline{[\vec{v}]} = 0 \end{cases} \tag{1.18}$$

Several models were proposed over the years to represent the subgrid-scale kinematic viscosity ν_{SGS}, and most of them share the following form:

$$\nu_{SGS} = (C\Delta)^2 \, \mathcal{D}\left(\overline{[\vec{v}]} \right), \tag{1.19}$$

where C is the model constant which is usually tuned (either theoretically or numerically) so that the model produces the proper amount of dissipation in the simple case of decaying isotropic turbulence. The length scale Δ denotes the typical size of the local cell of the mesh used to solve the filtered Navier-Stokes equations (Eq. (1.18)), and $\mathcal{D}$ is a differential operator which defines the SGS model and operates on the resolved velocity field $\overline{[\vec{v}]}$. In the present thesis, the Sigma model[5] [14, 142] is used, meaning that:

$$\mathcal{D}\left(\overline{[\vec{v}]} \right) = \frac{\sigma_3 (\sigma_1 - \sigma_2)(\sigma_2 - \sigma_3)}{\sigma_1^2}. \tag{1.20}$$

In this expression, $\sigma_1 \geq \sigma_2 \geq \sigma_3 \geq 0$ are the three singular values of the local velocity gradient tensor, and can be efficiently computed [142]. The model constant

[4] It is assumed that filtering and differentiation commute.

[5] Other SGS models are available in the YALES2 solver, such as the Dynamic Smagorinsky model, but are not considered in the present thesis work.

C is chosen to be $C = 1.35$. The Sigma model is selected because it meets several useful properties relevant in terms of SGS modeling, although not shared by the other SGS models. Notably, this model results in zero SGS viscosity in a number of canonical flows, where the structure of the velocity gradient tensor indicates that the flow cannot be turbulent. The Sigma model has thus the property to better behave in laminar flows than many other models. In addition, it is suitable to intermittent flows [31].

1.3.3 Validation test case

The operation of the YALES2 flow solver is now illustrated considering a simple 2D pulsatile Poiseuille flow test case. A Newtonian fluid flows in an infinitely long channel characterized by two parallel walls spaced by a height $2h$ (see Fig. 1.17).

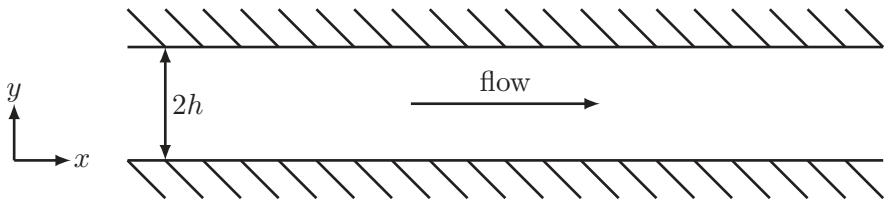

Figure 1.17: Illustration of the 2D pulsatile flow configuration. A Newtonian fluid flows in an infinitely long channel of height $2h$.

Theoretical framework

In such a simple configuration, the 2-dimensional velocity and pressure fields are expressed as:

$$\begin{pmatrix} v^x(x,y,t) \\ v^y(x,y,t) \end{pmatrix} = \begin{pmatrix} v^x(y,t) \\ 0 \end{pmatrix}, \tag{1.21}$$

$$p(x,y,t) = p(x,t). \tag{1.22}$$

Equation (1.1) can thus be simplified:

$$\begin{cases} \dfrac{\partial v^x}{\partial t} = -\dfrac{1}{\rho}\dfrac{\partial p}{\partial x} + \nu \dfrac{\partial^2 v^x}{\partial y^2} \\ \\ \dfrac{\partial v^x}{\partial x} = 0 \end{cases} \tag{1.23}$$

In the steady flow case, the temporal derivative becomes null. Assuming no-slip boundary conditions at the walls, the streamwise velocity is given by the Poiseuille solution:

$$v^x(y) = v_{max}\left(1 - \frac{y^2}{h^2}\right) \tag{1.24}$$

where h is the half height of the channel, v_{max} the maximum velocity, and $-h \leq y \leq h$. The maximum velocity and the pressure gradient are linked by the following relation:

$$-\frac{\partial p}{\partial x} = \frac{2\rho\nu v_{max}}{h^2} \tag{1.25}$$

In the case of a pulsatile flow due to an oscillatory pressure gradient $\partial p/\partial x = Ae^{i\omega t}$, the analytical solution for the streamwise velocity is [143]:

$$v^x(y,t) = \mathcal{R}\left[i\frac{A}{\rho\omega}\left(1 - \frac{\cos(\alpha y/h)}{\cos(\alpha)}\right)\right] \tag{1.26}$$

with:

$$\alpha = h\sqrt{\frac{\omega}{\nu}}e^{i3\pi/4}$$

YALES2 simulations

The configuration is simulated with the YALES2 flow solver using periodic boundary conditions in the x direction, thus representing the infinitely long channel. In this case, the pressure gradient $\partial p/\partial x$ becomes null, and a volumetric force f^x is used to drive the flow.

The use of periodic boundary conditions enables to have a numerical configuration free from border effects, usually inherent to the classical inlet/outlet boundary conditions. This allows to perform the simulations in a very short computational domain, thus reducing the computational time. In this case, simulations are performed in a rectangular computational domain with a height 20 times larger than its length, which is meshed using a cartesian mesh of 5×100 elements.

The parameters and variables useful for the simulations can be defined:

- The Womersley number $W_0 = h\sqrt{\omega/\nu}$.
- The Reynolds number $Re = f^x h^3/\rho\nu^2$.
- The maximum streamwise velocity $v_{max} = f^x h^2/2\rho\nu$.
- The non-dimensional y coordinate $\tilde{y} = y/h$.
- The non-dimensional time $\tilde{t} = t/T$, with $T = 2\pi/\omega$.
- The non-dimensional streamwise velocity $\tilde{v^x}(\tilde{y},\tilde{t}) = v^x(\tilde{y},\tilde{t})2h/\nu Re$.
- The non-dimensional analytical streamwise velocity $\tilde{v^x}_{an}(\tilde{y},\tilde{t})$.
- The non-dimensional numerical streamwise velocity $\tilde{v^x}_{num}(\tilde{y},\tilde{t})$.
- The absolute error $E(\tilde{y},\tilde{t}) = \left|\tilde{v^x}_{an}(\tilde{y},\tilde{t}) - \tilde{v^x}_{num}(\tilde{y},\tilde{t})\right|$.
- The spatial mean error $E_y(\tilde{t}) = \left[\sum_{i=1}^{n} E(\tilde{y}_i,\tilde{t})\right]/n$, averaged over n nodes within the height of the channel.
- The temporal mean error over one period $E_t = \left[\sum_{j=1}^{k} E_y(\tilde{t_k})\right]/k$, averaged over k sample times within the period.

The steady case is first simulated imposing a constant volumetric force f^x such that the Reynolds number $R_e = 100$. Figure 1.18 (left) shows the comparison of the streamwise velocity profile obtained from the YALES2 simulation with the analytical solution of Eq. (1.24). Numerical and analytical velocity profiles are in excellent agreement. The well known parabolic Poiseuille profile is accurately retrieved by the YALES2 flow solver, as indicated by the spatial mean error E_y (displayed in Fig. 1.18, right) which converges to a constant value $E_y = 8.64 \times 10^{-6}$.

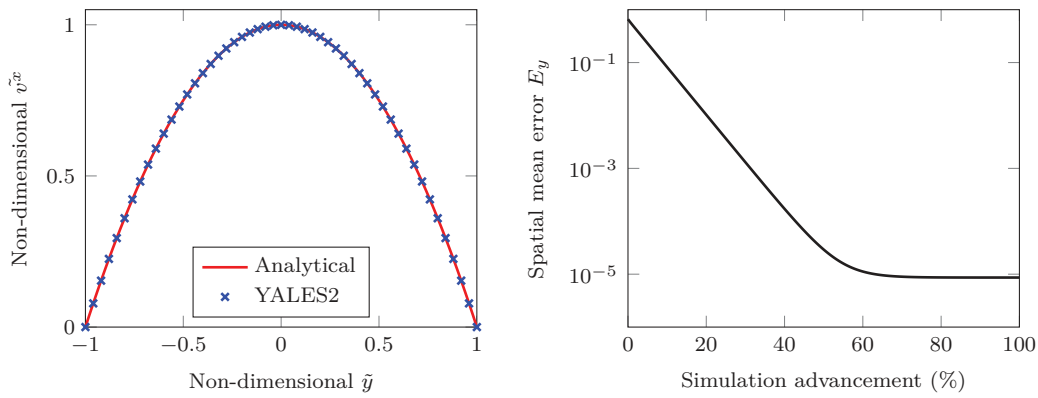

Figure 1.18: **Left:** Comparison of the streamwise velocity profile obtained from the YALES2 simulation with the analytical solution of Eq. (1.24). **Right:** Evolution of the spatial mean error over the simulation.

The pulsatile case is then simulated considering three different values of the Womersley number: $W_0 = 1$, $W_0 = 5$ and $W_0 = 10$. Figure 1.19 (left) shows the comparison of the streamwise velocity profile obtained from the YALES2 simulation with the analytical solution of Eq. (1.26). Several velocity profiles are displayed over one period of oscillation, showing an excellent agreement between the numerical and analytical profiles. It is seen that when the Womersley number W_0 is sufficiently low, the flow exhibits an oscillatory Poiseuille profile (see $W_0 = 1$ in Fig. 1.19, left). However, when the Womersley number W_0 is increased, the flow profile is no longer parabolic (see $W_0 = 5$ and $W_0 = 10$ in Fig. 1.19, left).

Figure 1.19 (right) shows the evolution of the temporal mean error E_t, which converges after a few periods. However, it is seen that the number of periods that need to be simulated before reaching convergence drastically increases with the Womersley number W_0. The converged temporal mean errors E_t obtained for each of the three considered Womersley numbers W_0 are displayed in Tab. 1.2.

	$W_0 = 1$	$W_0 = 5$	$W_0 = 10$
$E_t =$	1.29×10^{-5}	3.32×10^{-5}	3.54×10^{-5}

Table 1.2: Converged temporal mean errors.

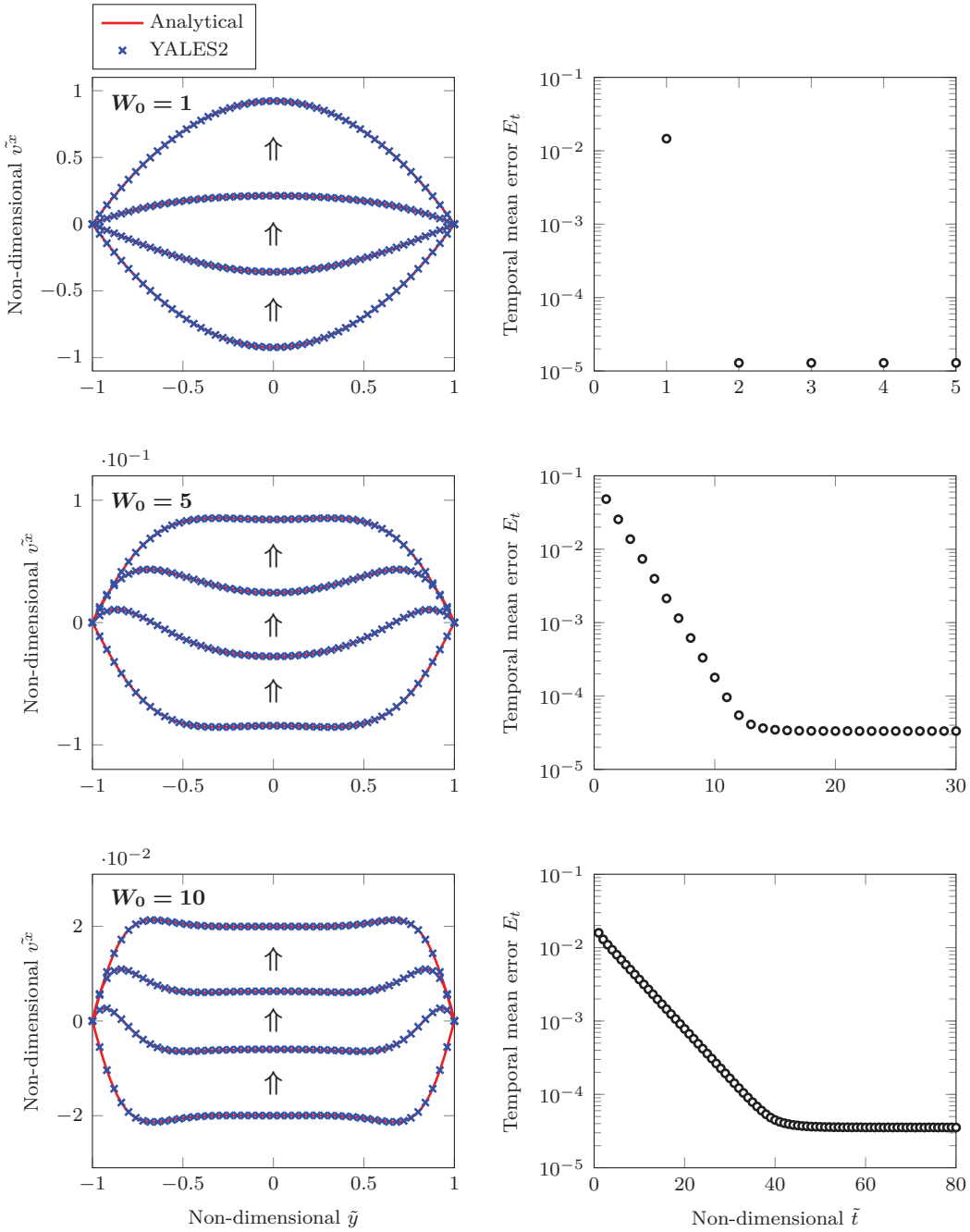

Figure 1.19: **Left:** Comparison of the streamwise velocity profiles obtained from the YALES2 simulation with the analytical solution of Eq. (1.26), over one period of oscillation. Three Womersley numbers are considered: $W_0 = 1$ (first row), $W_0 = 5$ (second row) and $W_0 = 10$ (third row). **Right:** Evolution of the temporal mean error over several periods of oscillation.

1.4 From YALES2 to YALES2BIO

The YALES2BIO[6] solver has been developed from the YALES2 flow solver for the simulation of blood flows [127], and thus inherits its massively parallel capabilities and high order finite-volume scheme for complex geometries. YALES2BIO aims at helping the analysis of medical devices in contact with blood such as flow diverters, ventricular assist devices, extracorporeal circulation, artificial heart and valves, blood analyzers, among others. Both macroscale and microscale simulations have been performed with YALES2BIO, such as the flow in a whole human left heart in the work of Chnafa *et al.* [31, 32, 33, 34, 35, 36], the flow in an idealized cardiovascular device in the work of Zmijanovic *et al.* [215], the flow of red blood cells within an industrial blood analyzer in the work of Gibaud *et al.* [78, 79, 80], and the aggregation of red blood cells in microfluidic devices in the work of Loiseau *et al.* [120].

Simulating flowing red blood cells

The YALES2BIO solver is thus able to perform FSI simulations of flowing red blood cells, which are handled using the immersed boundary method (IBM). The IBM has been chosen because of its ease of implementation within an existing computational code (in this case, the YALES2 flow solver), and its ability to handle large displacements of the red blood cell membrane.

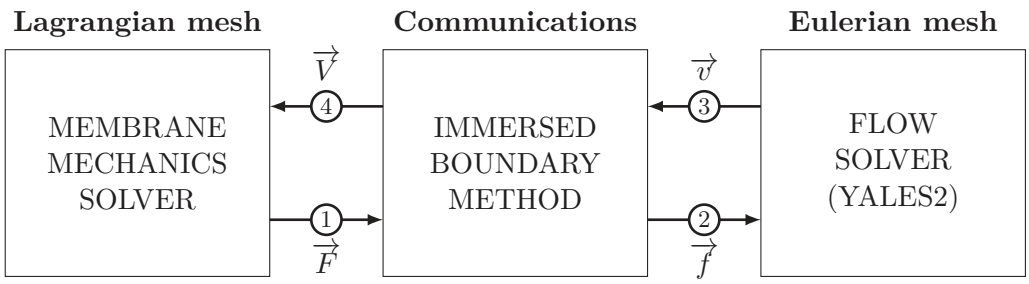

Figure 1.20: Operation of the YALES2BIO solver. The immersed boundary method (IBM) and an in-house membrane mechanics solver have been integrated within the YALES2 flow solver.

Figure 1.20 illustrates the operation of the IBM, and its integration within the YALES2 flow solver. As previously explained in section 1.2, the IBM is a non-conforming mesh method which independently solves the fluid and solid equations with their respective mesh discretization. The fluid equations are thus solved on a fixed Eulerian mesh, which is handled with the YALES2 flow solver. On top of this, a Lagrangian mesh characterized by a set of triangulated markers is immersed in the Eulerian fluid mesh. This triangulation of Lagrangian markers is used to represent an infinetely thin massless membrane which deforms and moves on top of the Eulerian fluid mesh. The membrane velocity $\vec{V}$ is imposed by the surrounding fluid velocity $\vec{v}$ thanks to the Dirac function δ, which enables communications between the fluid

[6] http://www.math.univ-montp2.fr/~yales2bio/

and solid non-conforming meshes:

$$\overrightarrow{V}\left(\overrightarrow{X},t\right)=\int_{\Omega_f}\overrightarrow{v}\left(\overrightarrow{x},t\right)\delta\left(\overrightarrow{x}-\overrightarrow{X}\right)dx, \tag{1.27}$$

where $\overrightarrow{x}$ and $\overrightarrow{X}$ respectively denote the coordinates vectors of the Eulerian fluid nodes and Lagrangian markers, and Ω_f is the volumetric fluid domain. Conversely, a fluid volumetric force $\overrightarrow{f}$ is generated by the membrane force $\overrightarrow{F}$ resulting from the membrane deformation, thus mimicking the action of the membrane on the fluid:

$$\overrightarrow{f}\left(\overrightarrow{x},t\right)=\int_{\Omega_s}\overrightarrow{F}\left(\overrightarrow{X},t\right)\delta\left(\overrightarrow{x}-\overrightarrow{X}\right)dX, \tag{1.28}$$

where Ω_s is the surfacic solid domain. As seen in Fig. 1.20, the IBM steps are performed in the following order:

(1) The membrane force $\overrightarrow{F}$ resulting from the membrane deformation is calculated on the Lagrangian mesh.

(2) The fluid volumetric force $\overrightarrow{f}$ generated by the membrane force $\overrightarrow{F}$ is calculated from Eq. (1.28).

(3) The fluid velocity $\overrightarrow{v}$ is calculated on the Eulerian mesh by solving the Navier-Stokes equations (Eq. (1.1)) (forced by the fluid volumetric force $\overrightarrow{f}$).

(4) The membrane velocity $\overrightarrow{V}$ is imposed by the surrounding fluid velocity $\overrightarrow{v}$ using (1.27).

The Dirac function δ used in Eqs. (1.27) and (1.28) is numerically represented by a smooth discrete Dirac function, which is adapted for unstructured meshes using the Reproducing Kernel Particle Method (RKPM) [128, 153, 168]. The IBM is used in steps (2) and (4) to treat the exchanges of velocities and forces between the fluid and solid non-conforming meshes, whereas steps (1) and (3) are performed with independent fluid and solid solvers. If step (3) is performed by the YALES2 flow solver, step (1) however requires the implementation of an in-house membrane mechanics solver. This solver has been implemented within the YALES2BIO solver and is described in the next section.

Membrane mechanics solver

As illustrated in Fig. 1.21, several deformation quantities are calculated on the triangulated Lagrangian markers: the local in-plane deformation is assessed by calculating the in-plane principal stretches λ_1 and λ_2 on the triangular faces; and the local curvature is assessed by calculating the mean curvature H, Gaussian curvature K, and surface Laplacian of the curvature $\Delta_{LB}H$ on the Lagrangian markers.

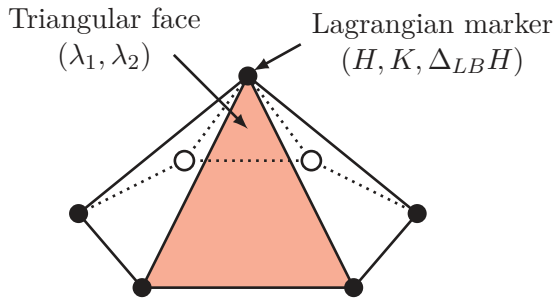

Figure 1.21: Illustration of the deformation quantities calculated on the triangulated Lagrangian markers. The in-plane principal stretches λ_1 and λ_2 are calculated for each triangular face. The mean curvature H, Gaussian curvature K, and Laplacian of the curvature $\Delta_{LB}H$ are calculated for each Lagrangian marker.

The elastic force $\overrightarrow{F_E}$ is calculated from the in-plane principal stretches λ_1 and λ_2, which is widely used to represent the local resistance of the membrane cytoskeleton to shear and area-dilatation [51, 52, 53, 57, 179, 180, 181]. This elastic force $\overrightarrow{F_E}$ is derived from the strain energy function W, following the method of Charrier *et al.* [27]. In the case of a Neo-Hookean material[7], the strain energy function W reads:

$$W = \frac{E_s}{2}\left(\lambda_1^2 + \lambda_2^2 + \lambda_1^{-2}\lambda_2^{-2} - 3\right), \tag{1.29}$$

where E_s represents the in-plane shear modulus (expressed in N/m). Given that the triangular faces of the triangulated set of Lagrangian markers remain triangular during the membrane deformation, the state of deformation is homogeneous and the in-plane principal stretches λ_1 and λ_2 are constant within each face. One considers a triangular face f composed of three markers f_1, f_2 and f_3. The in-plane x and y components[8] of the elastic force resulting from the deformation of the triangular face f, and acting on the three markers f_1, f_2, f_3, are expressed as:

$$\begin{aligned}
\begin{pmatrix} {F_E}^x|_{f_1} \\ {F_E}^x|_{f_2} \\ {F_E}^x|_{f_3} \end{pmatrix} &= S_f \frac{\delta W}{\delta \lambda_1} \begin{pmatrix} \delta\lambda_1/\delta\, U^x|_{f_1} \\ \delta\lambda_1/\delta\, U^x|_{f_2} \\ \delta\lambda_1/\delta\, U^x|_{f_3} \end{pmatrix} + S_f \frac{\delta W}{\delta \lambda_2} \begin{pmatrix} \delta\lambda_2/\delta\, U^x|_{f_1} \\ \delta\lambda_2/\delta\, U^x|_{f_2} \\ \delta\lambda_2/\delta\, U^x|_{f_3} \end{pmatrix}, \\
\begin{pmatrix} {F_E}^y|_{f_1} \\ {F_E}^y|_{f_2} \\ {F_E}^y|_{f_3} \end{pmatrix} &= S_f \frac{\delta W}{\delta \lambda_1} \begin{pmatrix} \delta\lambda_1/\delta\, U^y|_{f_1} \\ \delta\lambda_1/\delta\, U^y|_{f_2} \\ \delta\lambda_1/\delta\, U^y|_{f_3} \end{pmatrix} + S_f \frac{\delta W}{\delta \lambda_2} \begin{pmatrix} \delta\lambda_2/\delta\, U^y|_{f_1} \\ \delta\lambda_2/\delta\, U^y|_{f_2} \\ \delta\lambda_2/\delta\, U^y|_{f_3} \end{pmatrix},
\end{aligned} \tag{1.30}$$

where S_f is the original face area, and $\left(U^x|_{f_1}, U^x|_{f_2}, U^x|_{f_3}\right)$, $\left(U^y|_{f_1}, U^y|_{f_2}, U^y|_{f_3}\right)$ denote the in-plane x and y components of the displacement of markers f_1, f_2, f_3. Forces are then gathered at each marker by summing the contributions of the connected faces.

[7]This Neo-Hookean expression of the strain energy function W is one possible description among others of the membrane in-plane elasticity, and is only provided as an example.
[8]x and y denote the local cartesian frame associated to the plane of the triangular face f.

The bending resistance of the membrane lipid bilayer is represented by an additional force which is calculated from the local curvature of the membrane. This force is derived from the bending energy $\mathcal{E}_b$ proposed by Helfrich [88]:

$$\mathcal{E}_b = \frac{\kappa_b}{2} \int_S (2H - c_0)^2 \, dS, \tag{1.31}$$

with κ_b the bending modulus (expressed in N.m) and c_0 a possible spontaneous curvature. The derived bending force reads:

$$\overrightarrow{F_b} = \kappa_b \left[(2H - c_0) \left(2H^2 - 2K + c_0 H \right) + 2\Delta_{LB} H \right] \overrightarrow{n}, \tag{1.32}$$

with $\overrightarrow{n}$ the outward normal vector to the surface. The terms of the bending force are calculated by local fitting of a quadratic approximation of the surface. The method is similar to the one used by Farutin *et al.* [62].

Another force can be calculated to control the global area variation of the red blood cell membrane, thus modeling the quasi-incompressibility of the lipid bilayer. This force is derived from the global area conservation energy, which reads:

$$\mathcal{E}_S = \frac{\kappa_S}{2} \frac{(S - S_0)^2}{S_0}, \tag{1.33}$$

with κ_S the area modulus (expressed in N/m), S the area of the membrane and S_0 its target area (typically, the initial surface area of the membrane). The equivalent force reads:

$$\overrightarrow{F_S} = -2\kappa_S \frac{(S - S_0)}{S_0} H \, \overrightarrow{n}. \tag{1.34}$$

1.5 Chapters contents

The research contribution of the present thesis work gave rise to the writing of three articles which have been published/submitted in different journals, and constitute the three following chapters of this thesis. These three chapters are thus independent and can be read separately.

Chapter 2 corresponds to an article entitled "How should the optical tweezers experiment be used to characterize the red blood cell membrane mechanics" [170] which has been submitted in *Biomechanics and Modeling in Mechanobiology*. This chapter constitutes a numerical study in which an experiment involving red blood cells, the optical tweezers experiment, is simulated with the YALES2BIO solver. The general objective of this study is to provide some insights helpful for the characterization of the red blood cell membrane mechanics.

Chapter 3 corresponds to an article entitled "Validation of an immersed thick boundary method for simulating fluid-structure interactions of deformable membranes" [168] which has been published in the *Journal of Computational Physics*. This chapter seeks to extend the features of the YALES2BIO solver to FSI simulations of 3D continuum membranes having a finite thickness, keeping the IBM formalism implemented in the YALES2BIO solver and presented in section 1.4. This

innovative method, called immersed thick boundary method (ITBM), is described and extensively validated in this chapter.

Chapter 4 corresponds to an article entitled "A combined experimental and numerical study of a polymeric aortic valve model" [171] which has been submitted in *Cardiovascular Engineering and Technology*. The contents presented in this chapter result from a collaboration with the Helmholtz Institute (Aachen University, Germany) which aimed at investigating, both experimentally and numerically, the complex FSI problem involved when the blood flows out of the left ventricle, passing through the aortic valve. The experiment performed at the Helmholtz Institute is simulated using the YALES2BIO solver, and especially the immersed thick boundary method (ITBM) presented in the previous chapter.

Chapter 2

Red blood cells modeling

Chapter contents

2.1 Introduction 30
2.2 Numerical method 31
2.2.1 Membrane forces computation 32
2.2.2 Navier-Stokes equations solver 34
2.3 Optical tweezers modeling 34
2.3.1 Computational setup 35
2.3.2 Validation 36
2.4 Influence of the membrane modeling 39
2.4.1 Comparison of axial and transverse diameters 40
2.4.2 Characterization of the RBC shape 40
2.4.3 Area variations 42
2.5 Discussion 43

Preliminary remarks

This chapter corresponds to an article entitled "How should the optical tweezers experiment be used to characterize the red blood cell membrane mechanics" [170] which has been submitted in *Biomechanics and Modeling in Mechanobiology*. In this chapter, the well known optical tweezers experiment, designed to investigate the complex mechanical behavior of red blood cells, is simulated using the YALES2BIO solver. The YALES2BIO numerical method is thus briefly reminded in section 2.2, before presenting the computational setup and results. This chapter raises relevant questions about the ability of the optical tweezers experiment to characterize and validate a suitable mechanical model of the red blood cell membrane. It also attempts to answer these questions, giving possible tracks of improvements of the optical tweezers experimental setup.

2.1 Introduction

Blood is a complex substance consisting in a suspension of platelets, white blood cells and red blood cells (RBCs) in a Newtonian fluid, the plasma. The RBCs, which typically represent 40-45% of the whole blood volume, are composed of a membrane enclosing an internal fluid, the cytoplasm. The RBC membrane is a composite structure composed of a lipid bilayer and a two-dimensional elastic cytoskeleton, both linked through temporary tethering sites thanks to transmembrane proteins embedded in the lipid bilayer. This complex structure confers to the RBC membrane very specific mechanical properties: the cytoskeleton provides a resistance to shear sollicitations and slightly resists to area-dilatation, while the lipid bilayer provides to the membrane its bending stiffness and quasi-incompressibility. The RBCs have a biconcave discocyte shape at rest with a remarkable deformability, because of the excess of surface area enclosing the inner volume. RBCs are thus able to undergo very large deformation preserving their area, squeezing through capillaries with inner diameter less than 3 μm, although the average large diameter of a RBC is about 8 μm. As mentioned by Mohandas and Gallagher [135], the normal RBC can deform with linear extensions of up to 250%, but a 3% to 4% increase in surface area results in cell lysis.

So far, there is no universal model to describe the mechanical behavior of the RBC membrane. The local elasticity of the RBC membrane is generally described using either continuum models [62, 100, 111, 173] or molecular models [28, 40, 64, 67, 114, 154], which can be complemented with other global models to treat the quasi-incompressibility of the lipid bilayer [64, 154]. Detailed experimental investigations of the RBC mechanics are nonetheless needed in order to: 1) characterize and validate a numerical model of the RBC membrane; 2) once validated, determine the mechanical parameters of the model.

To gain insight into the mechanical behavior of RBCs, experimental techniques were developed for measurements of the RBC membrane properties [2]. Micropipette aspiration [58] and optical tweezers [89, 131] are the most popular ones, and were notably used to determine the shear modulus of the RBC membrane. The optical tweezers experiment by Mills *et al.* [131] provides a useful means for the analysis of the single cell mechanics under a variety of well-controlled stress states, where stretching of an isolated RBC is generated by means of attached silica microbeads and optical trap. Using a continuum model of the RBC membrane based on the Yeoh constitutive law [207] to solve the deformation of the RBC subjected to optical stretching, they successfully matched the force-extension data obtained from the experiment, and were able to extract the shear modulus of the RBC membrane.

A recent work of Dimitrakopoulos [49] showed that large differences of shear modulus reported in various studies may be explained based on the different membrane models used to fit the experimental data. He demonstrated that when using a continuum description of the RBC membrane, the only constitutive law able to

match well the wide variety of experimental data avalaible in the literature is the Skalak law, specifically developed by Skalak *et al.* to represent the in-plane elasticity of the RBC membrane [174]. Based on this finding, he stated that Mills *et al.* [131] found the shear modulus that represents the Yeoh law, but not the true shear modulus of the RBC membrane.

As a consequence, the numerical results of Mills *et al.* [131] were successfully matched to the force-extension data obtained from optical tweezers using the Yeoh law, whereas a proper modeling of the RBC membrane should rather rely on the Skalak law. This reveals the simplistic nature of these experimental data, which was also pointed out by Dimitrakopoulos [49]. Despite this observation, optical tweezers data continue to be used as a way to validate numerical models of the RBC membrane [28, 40, 62, 64, 67, 100, 111, 114, 154, 173], notably to probe the accuracy of solvers dedicated to the study of the RBC dynamics under flow. However, a proper validation test case needs to be selective to discriminate between appropriate and inappropriate models. There is a suspiscion that computing optical tweezers experiment does not constitute a true validation test case.

The present paper constitutes a numerical study which first aims at highlighting the limitations of the optical tweezers experiment for characterizating the mechanics of the RBC membrane. The optical tweezers experiment by Mills *et al.* [131] is simulated using a numerical method dedicated to the simulation of the dynamics of RBCs under flow. After a brief description of this numerical method, an easy-to-implement computational setup is presented and validated against the numerical results of Mills *et al.* [131]. Then, different membrane continuum models are investigated, based on various combinations of strain, area conservation and bending energies. Detailed analysis of the shape of the stretched RBC are carried out in order to identify which kind of additional experimental data could be helpful to better characterize the mechanics of the RBC membrane.

2.2 Numerical method

The present numerical method is very similar to the one developed by Mendez *et al.* [128] and Sigüenza *et al.* [168] for fluid-structure interactions (FSI) of deformable membranes, and is based on the immersed boundary method (IBM) introduced by Peskin [152]. Two independent meshes are considered to discretize the RBC membrane and the fluid. The RBC membrane is discretized by a moving Lagrangian mesh, and the fluid is discretized by a fixed Eulerian unstructured mesh. The different steps of the present method are the following:

(1) The membrane force $\overrightarrow{F}$ is calculated on the Lagrangian mesh, which depends on the membrane deformation and on the models used to represent the membrane rheology.

(2) The forces exerted by the membrane on the fluid are represented by the fluid volumetric force $\overrightarrow{f}$, calculated on the Eulerian mesh by regularizing the mem-

brane force $\overrightarrow{F}$ such as

$$\overrightarrow{f}\left(\overrightarrow{x},t\right)=\int_{\Omega_s}\overrightarrow{F}\left(\overrightarrow{X},t\right)\delta\left(\overrightarrow{x}-\overrightarrow{X}\right)dX,$$

where $\overrightarrow{x}$ and $\overrightarrow{X}$ respectively denote the coordinates vectors of the Eulerian fluid nodes and Lagrangian nodes, Ω_s denotes the solid domain defining the RBC membrane, and δ is the well known Dirac function.

(3) The fluid velocity $\overrightarrow{v}$ is calculated on the Eulerian mesh by solving the Navier-Stokes equations (forced by the source term $\overrightarrow{f}$).

(4) The membrane velocity $\overrightarrow{V}$ is calculated on the Lagrangian mesh by interpolating the fluid velocity $\overrightarrow{v}$ such as

$$\overrightarrow{V}\left(\overrightarrow{X},t\right)=\int_{\Omega_f}\overrightarrow{v}\left(\overrightarrow{x},t\right)\delta\left(\overrightarrow{x}-\overrightarrow{X}\right)dx,$$

where Ω_f denotes the fluid domain.

The Dirac function δ used in the procedures of regularization and interpolation of steps (2) and (4) is numerically represented by a smooth dicrete Dirac function, which is adapted to unstructured meshes using the Reproducing Kernel Particle Method [128, 153, 168]. Interpolation of the fluid velocity on the membrane Lagrangian mesh leads to small mass conservation errors. A specific algorithm has been developed to perfectly conserve the volume of the RBC during the calculations [128, 168].

2.2.1 Membrane forces computation

In the present method, the RBC membrane is considered to be infinitely thin, and is represented by a triangulated surface. The membrane force is derived from a combination of strain, area conservation and bending energies. Resistances to shear and area-dilatation are modeled thanks to a hyperelastic strain energy function W, which is written as a function of the local in-plane principal values of strain λ_1 and λ_2, following the method of Charrier *et al.* [27, 52, 57, 180]. Several hyperelastic models are investigated in the present study:

- The Neo-Hookean law,

$$W_{NH}=\frac{E_s}{2}\left(\lambda_1^2+\lambda_2^2+\lambda_1^{-2}\lambda_2^{-2}-3\right), \tag{2.1}$$

where E_s stands for the membrane in-plane shear modulus.

- The Yeoh law,

$$W_{YE}=\frac{E_s}{2}\left(\lambda_1^2+\lambda_2^2+\lambda_1^{-2}\lambda_2^{-2}-3\right)+C_3\left(\lambda_1^2+\lambda_2^2+\lambda_1^{-2}\lambda_2^{-2}-3\right)^3, \tag{2.2}$$

which is an extension of the previous Neo-Hookean model, with the addition of a non-linear term driven by the non-linear modulus C_3.

- The law introduced by Skalak *et al.* [174] for red blood cells,

$$W_{SK} = \frac{E_s}{4}\left[\left(\lambda_1^2+\lambda_2^2-2\right)^2 + 2\left(\lambda_1^2+\lambda_2^2-\lambda_1^2\lambda_2^2-1\right)\right] + \frac{E_a}{4}\left(\lambda_1^2\lambda_2^2-1\right)^2, \quad (2.3)$$

where shear resistance and area dilatation resistance are separately taken into account through the shear modulus E_s and the area-dilatation modulus E_a, respectively. It can also be written with the ratio of the area dilatation modulus to the shear modulus, $C = E_a/E_s$,

$$W_{SK} = \frac{E_s}{4}\left[\left(\lambda_1^2+\lambda_2^2-2\right)^2 + 2\left(\lambda_1^2+\lambda_2^2-\lambda_1^2\lambda_2^2-1\right) + C\left(\lambda_1^2\lambda_2^2-1\right)^2\right]. \quad (2.4)$$

Although the Skalak law can be used to control area variations of the RBC membrane, another approach consists in using a global area conservation energy:

$$\mathcal{E}_S = \frac{\kappa_S}{2}\frac{(S-S_0)^2}{S_0}, \quad (2.5)$$

with κ_S the area modulus, S the area of the membrane and S_0 its target area. This energy is actually already used in other formulations based on discrete approaches [64, 154] or in shape predictions by energy minimization [115, 116]. Conveniently, the force applied by the membrane on the fluid, associated to the energy term $\mathcal{E}_S$ can be expressed explicitly:

$$\overrightarrow{F_S} = -2\kappa_S\frac{(S-S_0)}{S_0}H\,\overrightarrow{n}, \quad (2.6)$$

with H the mean curvature and $\overrightarrow{n}$ the outward normal vector to the surface.

In addition, the bending resistance of the membrane can be represented using the bending energy $\mathcal{E}_b$, proposed by Helfrich [88]:

$$\mathcal{E}_b = \frac{\kappa_b}{2}\int_S (2H-c_0)^2\,dS, \quad (2.7)$$

with $\kappa_b = 2.0\times10^{-19}$ N.m [115, 116] the bending modulus, and c_0 a possible spontaneous curvature (which is set to zero in the present study). The bending force applied by the membrane on the fluid reads:

$$\overrightarrow{F_b} = \kappa_b\left[(2H-c_0)\left(2H^2-2K+c_0H\right)+2\Delta_{LB}H\right]\overrightarrow{n}, \quad (2.8)$$

where Δ_{LB} denotes the surface Laplacian operator [214] (also called the Laplace-Beltrami operator) and K is the local Gaussian curvature of the surface. The terms of the bending force are calculated by local fitting of a quadratic approximation of the surface. The method is similar to the one used by Farutin *et al.* [62]. Table 2.1 summarizes the three energies introduced, with the associated parameters. Every combination of these energies (W, $\mathcal{E}_S$, $\mathcal{E}_b$) can be used to model the RBC membrane.

W		$\mathcal{E}_S$	$\mathcal{E}_b$
NH:	E_s (N/m)	κ_S (N/m)	κ_b (N.m)
YE:	E_s (N/m) C_3 (N/m)		
SK:	E_s (N/m) C		

Table 2.1: Different energies available to model the RBC membrane and associated notations of mechanical moduli.

2.2.2 Navier-Stokes equations solver

The fluid inside and outside the RBC is supposed to be incompressible and Newtonian. The YALES2BIO flow solver is used [34, 128, 168, 215] to solve the forced Navier-Stokes equations over the Eulerian unstructured mesh by using a projection method [37]. The momentum conservation equations reads:

$$\frac{\partial \vec{v}}{\partial t} + \vec{\nabla}.(\vec{v} \otimes \vec{v}) = -\frac{\vec{\nabla} p}{\rho} + \nu \Delta \vec{v} + \frac{\vec{f}}{\rho}, \tag{2.9}$$

where $\vec{v}$ and p are the velocity vector and the pressure, ρ the density and ν the kinematic viscosity. For an incompressible fluid, the mass conservation equation becomes:

$$\vec{\nabla}.\vec{v} = 0 \tag{2.10}$$

The fluid velocity is advanced using a 4th-order centred scheme in space and a 4th-order Runge-Kutta scheme in time. A divergence-free velocity field is obtained at the end of the time-step by solving a Poisson equation for pressure and correcting the predicted velocity. A Deflated Preconditioned Conjugate Gradient (DPCG) algorithm is used to solve this Poisson equation [123, 140].

The YALES2BIO solver was validated in several test cases where reference data (either experimental, analytical or numerical) are available. This is described in previous publications, where the reader can also find additional implementation details [124, 128, 168, 169, 215].

2.3 Optical tweezers modeling

The purpose of this section is to establish a computational setup allowing the computation of the optical tweezers experiment by Mills *et al.* [131]. The computational setup presented in this section is built heavily on the one developed by Dao *et al.* [41], which has also been used in [131] to simulate the optical tweezers experiment. Figure 2.1(a) illustrates the experimental setup used in [131] to perform the stretching of the RBC. Two silica microbeads, of diameter 4.12 μm, are attached to the cell at diametrically opposite points. The left bead is anchored to the surface of a glass slide while the right bead is trapped by a laser beam. The trapped bead remaining at rest, moving the slide and attached left bead stretches the cell. Then, the axial

diameter D_A (in the direction of the stretching), and the transverse diameter D_T (orthogonal to the stretching direction) are measured on the stretched RBC.

2.3.1 Computational setup

The analytical model of the RBC biconcave shape proposed by Evans and Fung [59] is used to define the RBC geometry:

$$z = \pm 0.5 R_0 \left[1 - \frac{x^2 + y^2}{R_0^2} \right] \left[A_1 + A_2 \frac{x^2 + y^2}{R_0^2} + A_3 \left(\frac{x^2 + y^2}{R_0^2} \right)^2 \right] \tag{2.11}$$

where $R_0 = 3.91$ μm is the average RBC radius, $A_1 = 0.207161$, $A_2 = 2.002558$, and $A_3 = -1.122762$.

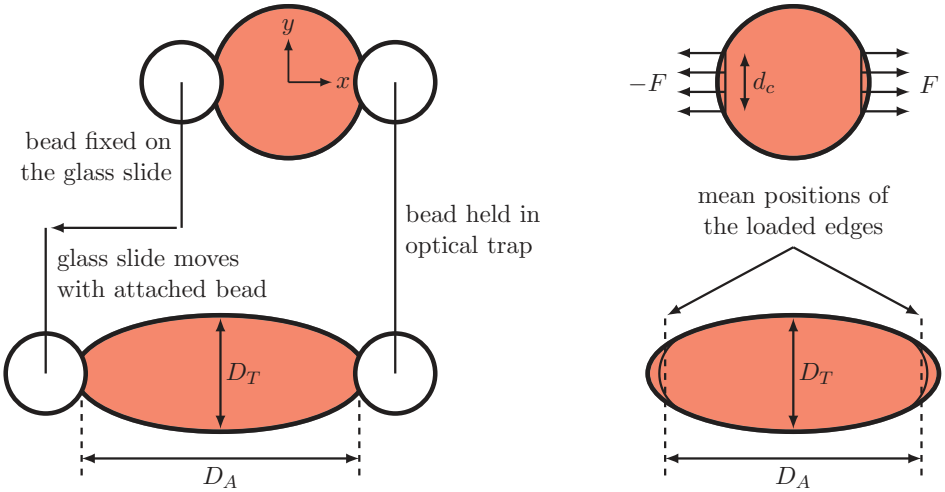

(a) Experimental setup **(b)** Computational setup

Figure 2.1: **(a)** Illustration of the experimental setup of [131]. The axial (D_A) and transverse (D_T) diameters of the stretched RBC are measured. **(b)** Computational setup used to simulate the optical tweezers experiment. A stretching force F is applied over the two circular edges delimitating the contact areas between the RBC and the beads, with a contact size $d_c = 2$ μm.

Rather than explicitly solving the contact between the beads and the RBC (as Dao *et al.* [41] and Mills *et al.* [131]), most of the works simulating the optical tweezers experiment consider pure Neumann loading conditions to simulate the RBC stretching, applying a constant stretching force F over a certain percentage of nodes at the extremities of the RBC [28, 62, 67, 100, 111, 173]. The drawback of this approach was nonetheless pointed out by Klöppel and Wall [100]: the rigidity of the beads is not properly taken into account, leading to a larger axial diameter (D_A), and thus a higher estimation of the in-plane shear modulus. An alternative use of Neumann loading conditions which mimics the beads rigidity is introduced, within a three-step strategy:

- The contact areas between the beads and the RBC are properly defined following the procedure of Dao *et al.* [41]. As shown in Fig. 2.1(b), these contact areas are defined by intersecting the surface of the RBC with two opposite planes perpendicular to the stretching direction. The position of these planes is chosen such that the contact size between the beads and the RBC is $d_c = 2\ \mu$m [41].

- Rather than applying the stretching force F over all the nodes of the contact areas, the force is applied only on the nodes located on the edges delimiting the contact areas (see Fig. 2.1(b)).

- Instead of evaluating the axial diameter (D_A) as the distance between the extremities of the stretched RBC, the axial diameter is determined by calculating the mean position of each loaded edge, which are deformed during the RBC stretching (as sketched in Fig. 2.1(b)).

Consistently with the numerical framework described in section 2.2, the computation of the RBC stretching consists in solving a transient fluid-structure interaction problem until stabilization of the shape. The RBC is immersed in a fluid box extended from $-4R_0$ to $4R_0$ in the x direction (direction of the stretching), from $-2R_0$ to $2R_0$ in the y direction (direction orthogonal to the stretching), and from $-R_0$ to R_0 in the z direction (direction perpendicular to the plane of the RBC). The fluid mesh is composed of 881 992 tetrahedral elements, with a constant mesh resolution of $R_0/12.5$. The RBC membrane is composed of 6 434 nodes, with a constant mesh resolution of $R_0/25$.

The stretching force is applied on the RBC membrane as an external force, with a time-dependent ramp ranging from 0 to the desired value of F. This external force is seen by the fluid which starts moving, and deforms the RBC. After a transient phase, the mechanical forces inside the membrane and the applied external force balance, and a steady deformation is obtained. The choice of the fluid properties and the size of the computational domain may affect the transient phase, but have no influence on the steady deformation of the RBC and calculated axial and transverse diameters. Only the final stabilized shapes are postprocessed.

2.3.2 Validation

With the aim to validate the present computational setup, the optical tweezers experiment by Mills *et al.* [131] is simulated, and the present simulations are compared with the numerical simulations performed in [131]. Two cases are simulated, corresponding to different modeling of the in-plane elasticity of the membrane. These two cases are summarized in Tab. 2.2. For both cases, only the local in-plane elasticity is considered. The membrane is assumed to follow the Neo-Hookean law (Eq. (2.1)) in case 1, and the Yeoh law (Eq. (2.2)) in case 2.

	$\boldsymbol{W}$	$\boldsymbol{\mathcal{E}_S}$	$\boldsymbol{\mathcal{E}_b}$
Case 1	NH: $E_s = 7.3\ \mu$N/m	X	X
Case 2	YE: $E_s = 7.3\ \mu$N/m $C_3 = E_s/30$	X	X

Table 2.2: Cases simulated with the present computational setup and compared with the results of Mills *et al.* [131].

Figure 2.2 shows both axial (D_A) and transverse (D_T) diameters of the RBC stretched by optical tweezers, as a function of the applied force, for cases 1 and 2. As the cell is more and more elongated when increasing the stretching force, it is seen that the axial diameter D_A increases. The elongation of the cell leads to its contraction in the orthogonal direction, resulting in a decrease of the transverse diameter D_T.

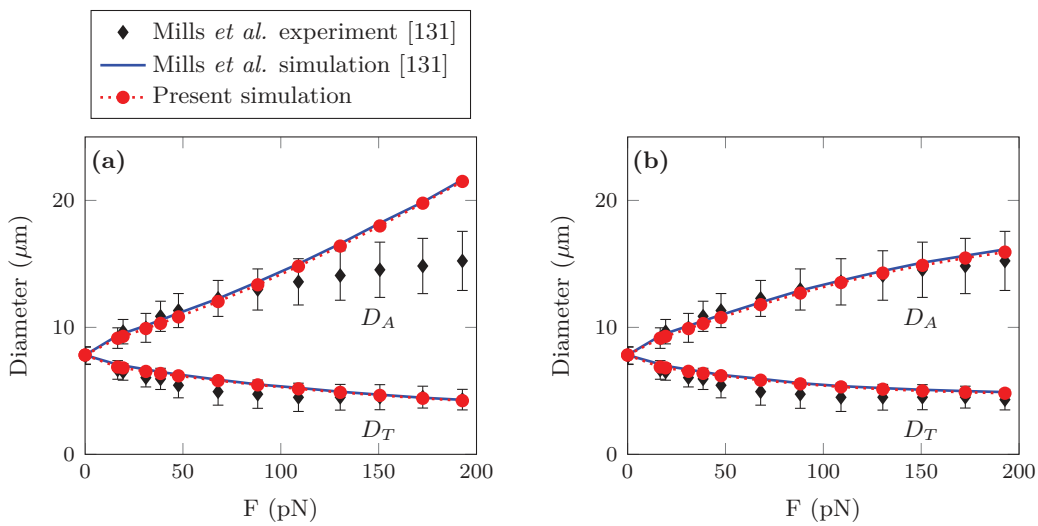

Figure 2.2: Axial (D_A) and transverse (D_T) diameters of the RBC stretched by optical tweezers. Comparison with the experimental and numerical data from Mills *et al.* [131]. **(a)** The RBC membrane is assumed to follow the Neo-Hookean law, corresponding to case 1. **(b)** The RBC membrane is assumed to follow the Yeoh law, corresponding to case 2.

When using pure Neumann loading conditions to simulate the RBC stretching [28, 62, 67, 100, 111, 173], the rigidity of the beads used in the optical tweezers experiment is neglected, which is known to strongly influence the deformation of the stretched RBC, especially the estimation of the axial diameter (D_A) [100]. The present results however show that it is possible to mimic the beads rigidity using a customized computational setup based on pure Neumann loading conditions, which is seen to faithfully reproduce the numerical results obtained by Mills *et al.* [131], who explicitly solved the contact between the beads and the RBC.

As pointed out by Mills *et al.* [131], comparison of the numerical results of case 1 with the experimental data shows that the Neo-Hookean law is not adapted to describe the behavior of the RBC membrane. Indeed, experimental trends are well captured over the range of 0-88 pN. However, the model deviates gradually for loadings higher than 88 pN, showing a strain-softening behavior under large deformation [13]. Conversely, the Yeoh law provides accurate predictions of diameters over the entire range of experimental data. The strain-hardening behavior of RBCs under large deformation is thus well transcribed by the model. Regarding the mechanical response of the stretched RBC in terms of axial and transverse diameters, the membrane modeling corresponding to case 2 provides a good description of the membrane mechanical behavior.

Figure 2.3 shows the deformation of the RBC for different values of the stretching force F, which ranges from 0 to 193 pN. A detailed analysis of the shape of the RBC shows that as the cell is elongated when increasing the force, a large fold is appearing, as also observed in the numerical simulations of Mills *et al.* [131]. Occurence of such a folding is however not investigated in the experiment.

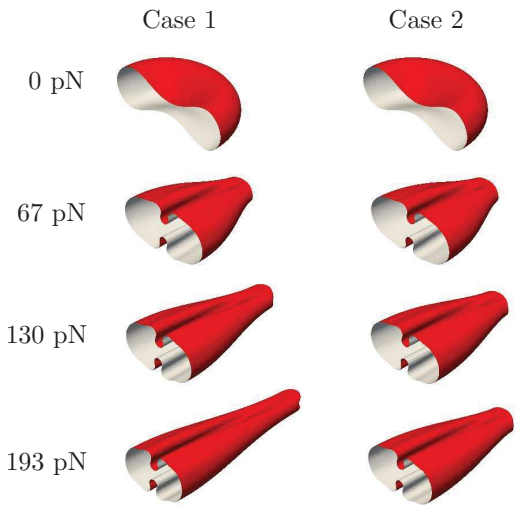

Figure 2.3: Visualization of the red blood cell deformation over the entire range of stretching force, for both cases 1 and 2. Only half of the cell is displayed.

In order to investigate the influence of the mesh resolution, two meshes were constructed from the mesh used in Fig. 2.2: a coarse mesh whose resolution is twice coarser than the reference mesh resolution, and a fine mesh whose resolution is twice finer than the reference mesh resolution. Axial (D_A) and transverse (D_T) diameters obtained from these three meshes are compared in Tab. 2.3 with the diameters obtained from numerical simulations of Mills *et al.* [131] for the largest loading $F = 193$ pN. The mesh resolution has almost no influence on the prediction of the axial diameter, and only few influence on the prediction of the transverse diameter. This proves that the reference mesh is sufficiently refined, and can thus be used in the remainder of this study.

	Mills simulation	Coarse mesh	Reference mesh	Fine mesh
D_A (μm)	16.14	15.92	15.93	15.93
D_T (μm)	4.90	4.94	4.81	4.72

Table 2.3: Influence of the mesh resolution for case 2, at the maximum imposed force of 193 pN.

2.4 Influence of the membrane modeling

The present computational setup is now used to investigate different continuum models of the RBC membrane. With the present numerical method, the different mechanical properties of the RBC membrane can be modeled by a combination of strain, area conservation and bending energies. Four new cases are summarized in Tab. 2.4.

	$\boldsymbol{W}$	$\boldsymbol{\mathcal{E}_S}$	$\boldsymbol{\mathcal{E}_b}$
Case 3	YE: $E_s = 7.3\ \mu$N/m, $C_3 = E_s/30$	X	$\kappa_b = 2.0 \times 10^{-19}$ N.m
Case 4	SK: $E_s = 3.65\ \mu$N/m, $C = 0.5$	X	$\kappa_b = 2.0 \times 10^{-19}$ N.m
Case 5	SK: $E_s = 3.65\ \mu$N/m, $C = 100$	X	$\kappa_b = 2.0 \times 10^{-19}$ N.m
Case 6	SK: $E_s = 3.65\ \mu$N/m, $C = 0.5$	$\kappa_S = 1.0\ 10^3\ \mu$N/m	$\kappa_b = 2.0 \times 10^{-19}$ N.m

Table 2.4: Summary of different continuum models of the RBC membrane investigated by means of optical tweezers simulations (see Tab. 2.2 for cases 1 and 2).

Note that the bending stiffness of the lipid bilayer was neglected in cases 1 and 2, but is accounted for in the others. Using the Yeoh law (Eq. (2.2)) to describe the local in-plane elasticity of the RBC membrane was seen to provide a good agreement with the optical tweezers experiment (see Fig. 2.2(b)). Case 3 thus appears to be a first obvious candidate to model the mechanics of the RBC membrane. As stated by Dimitrakopoulos [49], the RBC membrane should rather be modeled by the Skalak law instead of the Yeoh law. Cases 4 and 5 are thus introduced, with two different values of the ratio C (low value in case 4, and high value in case 5). Note however that when using the Skalak law to model the local in-plane elasticity of the RBC membrane, a high value of C should be considered to restrain the area variations of the RBC membrane, thus modeling the quasi-incompressibility of the lipid bilayer. Consequently, case 4 does not constitute a potential candidate to model the mechanics of the RBC membrane, but is only introduced to investigate the influence of the ratio C on the mechanical response of the RBC subjected to optical stretching. Finally, case 6 proposes a hybrid modeling of the RBC membrane,

dissociating the cytoskeleton and the lipid bilayer: the Skalak law with low ratio C is used to model the local in-plane elasticity of the cytoskeleton, allowing local area changes of the cytoskeleton; on top of this, the global area conservation energy is used to model the reorganisation of the quasi-incompressible lipid bilayer, sliding along the cytoskeleton. It is noticed that a twice smaller shear modulus E_s is considered when using the Skalak law in cases 4, 5, and 6, as compared to case 3. In the following, it will be shown that this reduction of the shear modulus E_s is required to have a good comparison with the optical tweezers experiment, which is consistent with the analysis of Dimitrakopoulos [49].

2.4.1 Comparison of axial and transverse diameters

Figure 2.4 shows the numerical predictions of the axial and transverse diameters for the different modeling cases introduced in Tab. 2.4. All cases provide a good comparison with the experimental results of Mills *et al.* [131]. Cases 5 and 6 are in a slightly better agreement with the experiment, especially regarding the transverse diameter (D_T) in the higher range of imposed stretching force. However, differences between all the modeling cases are contained within the experimental error bars. It is interesting to note that increasing the resistance to area-dilatation of the RBC membrane between case 4 and case 5 (by increasing the ratio C) has very few influence on the predictions of the axial and transverse diameters, which was also observed in previous works [169, 173]. In addition, restraining the area variation of the RBC membrane either locally (in case 5) or globally (in case 6) leads to almost identical predictions of the axial (D_A) and transverse (D_T) diameters.

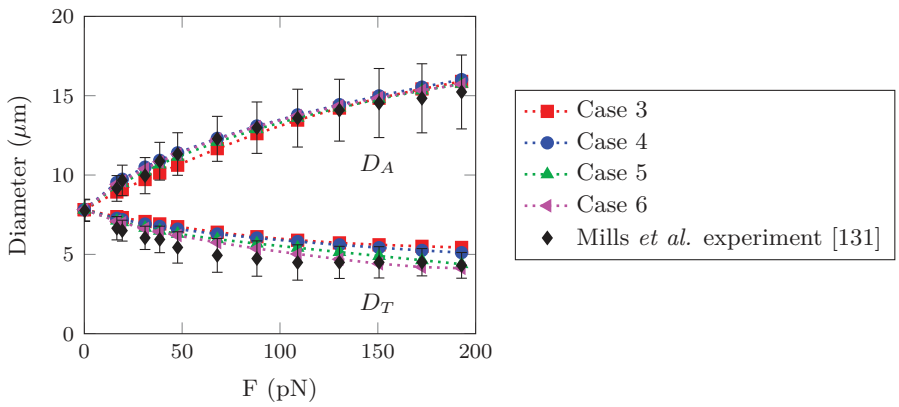

Figure 2.4: Comparison of the axial (D_A) and transverse (D_T) diameters of the RBC stretched by optical tweezers for the different modeling cases introduced in Tab. 2.4.

2.4.2 Characterization of the RBC shape

The deformation of the stretched RBC at different stretching forces is displayed in Fig. 2.5. First, it is seen that the shapes obtained in case 3 differ from the ones obtained in case 2 (see Fig. 2.3), which also uses the Yeoh law to model the local in-plane elasticity of the RBC membrane. The large fold which appears during the

RBC stretching in case 2 is restrained in case 3 by the bending stiffness of the lipid bilayer, modeled by the bending energy (neglected in case 2). The fold is however still visible during the stretching, but much smoother. In case 4, when switching the hyperelastic model to the Skalak law, the RBC tends to lose its biconcave shape with increasing stretching. This phenomenon is even more pronounced and faster in case 5, when the area-dilatation resistance is increased, leading to a more rounded shape at maximum stretching. Finally, case 6 exhibits a very similar behavior of case 5, with a faster transition from the biconcave to the rounded shape (see shapes at $F = 67$ pN in Fig. 2.5), and a more circular shape at maximum stretching.

In the light of these observations, it appears relevant to introduce two additional lengths measured on the deformed RBC: the in-plane length L_P, defined as being the height in the direction perpendicular to the plane of the RBC (see Fig. 2.5); the folding length L_F, also aligned with the direction perpendicular to the plane of the RBC, but evaluated at the fold location (see Fig. 2.5). As shown in Fig. 2.6(a), the discrimination between the different modeling cases is more obvious when analysing the evolution of the in-plane (L_P) and folding (L_F) lengths than the classical analysis made on the axial (D_A) and transverse (D_T) diameters (in Fig. 2.4). Previous observations of Fig. 2.5 can be highlighted: in case 3, the in-plane (L_P) and folding (L_F) lengths show parallel evolutions, meaning that the RBC keeps its biconcave shape for the whole range of stretching force; in case 4, lengths get closer with increasing stretching force, showing that the RBC progressively loses its biconcave shape when subjected to stretching; in cases 5 and 6, a transition from a biconcave folded shape to a rounded shape occurs when the two lengths become identical (for $F = 109$ pN in case 5, and $F = 88$ pN in case 6), and the shape of the RBC becomes more and more circular as the lengths increase with the stretching force.

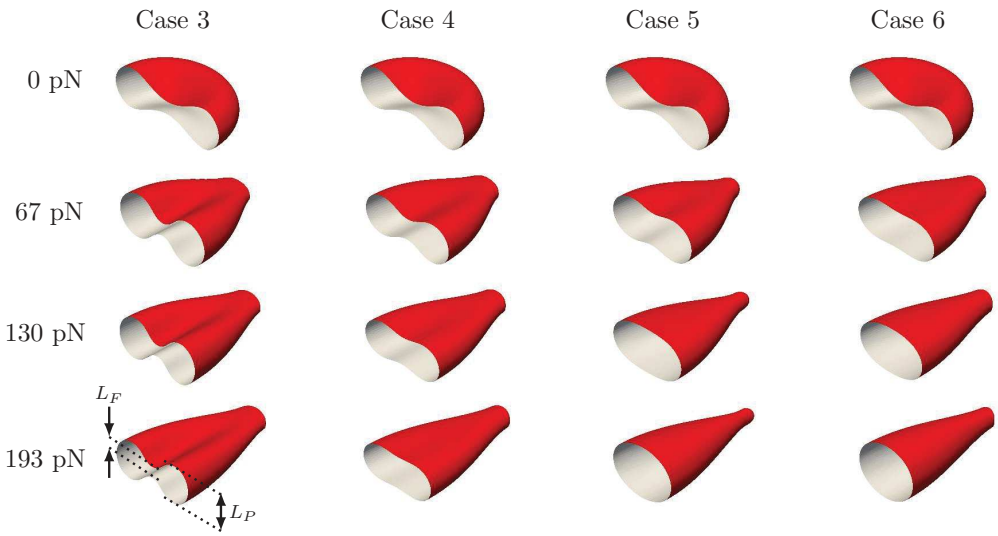

Figure 2.5: Visualization of the red blood cell deformation over the entire range of stretching force, for the different modeling cases introduced in Tab. 2.4. Only half of the cell is displayed.

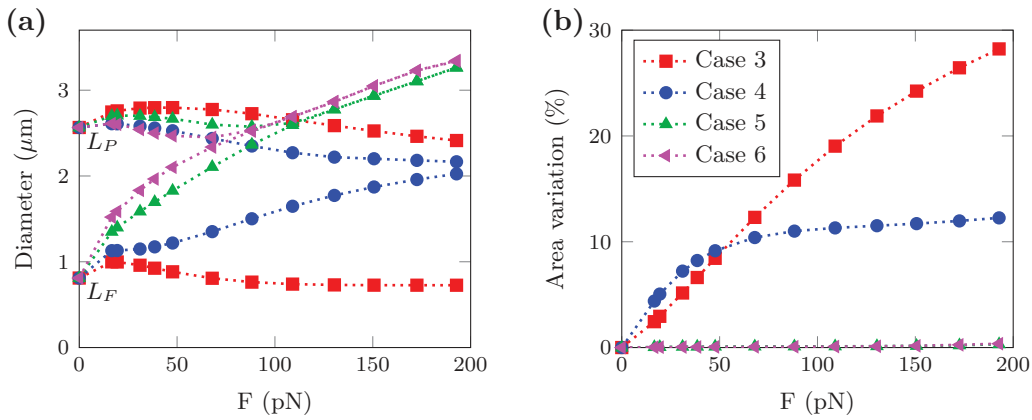

Figure 2.6: **(a)** Evolution of the in-plane (L_P) and folding (L_F) lengths as a function of the imposed stretching force F. **(b)** Global area variation of the red blood cell membrane for the different modeling cases introduced in Tab. 2.4.

2.4.3 Area variations

The ability of the quasi-incompressible lipid bilayer to restrain area variations during the RBC deformation is an important mechanical feature of the RBC membrane [135]. Figure 2.6(b) shows the evolution of the global area variation of the RBC membrane during stretching for the different modeling cases introduced in Tab. 2.4. In case 3, the area increase reaches 28%, since the Yeoh law is not designed to restrain area variations of the RBC membrane. Using the Skalak law in case 4 enables to restrain the area variation to a maximum value of 12%. Area variations are even more restrained when increasing the resistance to area-dilatation in cases 5 (0.3%) and 6 (0.4%).

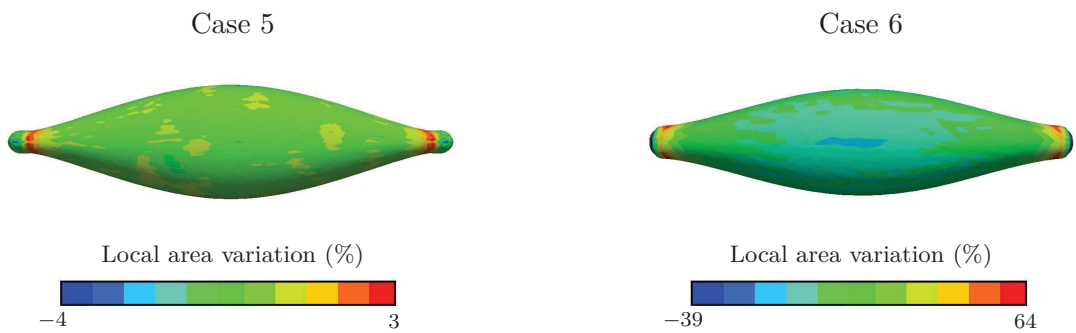

Figure 2.7: Comparison of the local area variations of the red blood cell membrane at the maximum stretching force $F = 193$ pN for the modeling approaches of cases 5 and 6.

Figure 2.7 shows the local area variation of the RBC membrane for modeling cases 5 and 6. In case 5, the use of the Skalak law with high ratio C allows very small local area variations of the RBC membrane. In case 6, the quasi-incompressibility of the lipid bilayer is independently modeled using the global area conservation energy, whereas the Skalak law with lower ratio C is used to model the own area-dilatation

resistance of the cytoskeleton. This results in higher local area variations, which correspond to the deformation of the cytoskeleton. In both cases, the maximum local area variations are obtained at the extremities of the cell, near to the bead/RBC contact areas. These regions of high stretching may thus be the locations where the RBC is the most prone to lysis. Note that variation of cytoskeleton area was measured by Disher *et al.* [50] in a micropipette aspiration experiment, but the authors are not aware of similar measurements in optical tweezers experiment.

2.5 Discussion

In the present paper, the optical tweezers experiment by Mills *et al.* [131] is simulated using a numerical method dedicated to the simulation of the dynamics of RBCs under flow. A computational setup for simulating the RBC stretching is presented, which is seen to perfectly reproduce the numerical results obtained by Mills *et al.* [131]. Influence of the RBC membrane modeling is then investigated, introducing different continuum models to describe the membrane mechanics.

Comparison of the numerical results with the force-extension data provided by the experiment (i.e. the axial (D_A) and transverse (D_T) diameters of the stretched RBC) shows that all modeling approaches are able to reproduce the mechanical response of the RBC subjected to optical stretching (see Fig. 2.4). An adjustment of the shear modulus E_s is however required depending if the RBC membrane is described using the Yeoh law or the Skalak law (E_s is twice smaller when using the Skalak law). It is also seen that some of these models allow non-physiological area variations of the RBC membrane during stretching (see Fig. 2.6(b)), especially the Yeoh law which was considered in previous works as a suitable model of the RBC membrane [131, 185]. Consistently with the findings of Dimitrakopoulos [49], this indicates that the Yeoh law should not be used to describe the mechanical behavior of the RBC membrane. This also indicates that the single analysis of the axial (D_A) and transverse (D_T) diameters of the stretched RBC is not a sufficient indicator for characterizing the mechanics the RBC membrane, and cannot be used alone to validate numerical models of the RBC membrane.

Detailed analysis of the shape of the stretched RBC reveal different behaviors among the investigated models (see Fig. 2.5). A transition of the RBC shape from a biconcave folded shape to a rounded shape is observed when restraining the area variations of the RBC membrane, either locally or globally. This observation may be due to the fact that the RBC tends to lose its biconcave shape when subjected to optical stretching, to prevent area variations of the RBC membrane. Note that such ellipsoidal shapes were also reported in previous numerical studies [62, 100, 114].

This transition from a biconcave folded shape to a rounded shape can be characterized by introducing two additional lengths measured in the direction perpendicular to the plane of the RBC: the in-plane length L_P, and the folding length L_F (see Fig. 2.6(a)). Experimental measurements of such lengths could thus be

of prime interest to make the optical tweezers experimental setup more helpful to characterize the mechanics of the RBC membrane.

More sophisticated measurements of the shape of the stretched RBC must however be performed with reasonable experimental uncertainties. One of the main source of uncertainty is expected to come from the contact areas between the beads and the RBC, which may vary from one experiment to the other. In the present computational setup, these contact areas are defined by the contact size d_c which is initially chosen to be $d_c = 2$ μm, as in the computations of Mills *et al.* [131]. Figure 2.8(a) shows the influence of this contact size on the numerical predictions of the axial (D_A) and transverse (D_T) diameters of the stretched RBC (using the modeling case 5), when the contact size is successively set to $d_c = 1$ μm, $d_c = 2$ μm and $d_c = 3$ μm.

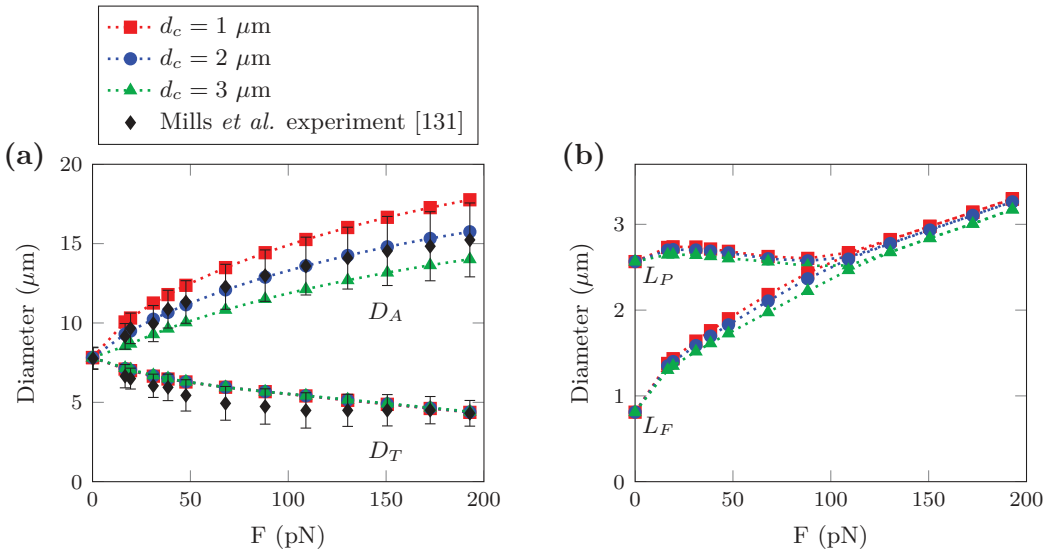

Figure 2.8: Influence of the bead-RBC contact area for the modeling case 5. **(a)** Axial (D_A) and transverse (D_T) diameters. **(b)** In-plane (L_P) and folding (L_F) lengths.

It is seen that the contact size strongly influences the prediction of the axial diameter (D_A), showing a more rigid behavior with increasing d_c, but has no influence on the prediction of the transverse diameter (D_T). This may explain the large and increasing error bars obtained by Mills *et al.* [131] in the experimental measurements of the axial diameter (D_A), as compared to the smaller and monotonous error bars obtained for the transverse diameter (D_T). Figure 2.8(b) shows that the contact size has only a little influence on the predictions of the in-plane (L_P) and folding (L_F) lengths, which means that comparison between computed and measured values of these quantities would be robust to the uncertainties related to the bead/RBC contact areas. The authors hope that these findings will arouse an interest for updated optical tweezers experiments.

Chapter 3

The immersed thick boundary method

Chapter contents

3.1 Introduction 47
3.2 Numerical method 48
3.2.1 Computation of the mechanical force 49
3.2.2 Forces regularization 51
3.2.3 Navier-Stokes equations resolution 55
3.2.4 Membrane convection 55
3.2.5 Discretization 55
3.2.6 Volume correction 55
3.3 Verification and validation 58
3.3.1 Non-linear bending of an elastic plate 58
3.3.2 Inflation of a spherical capsule 61
3.3.3 Capsule in a linear shear flow 64
3.3.4 Red blood cell stretched by optical tweezers 66
3.3.5 Flow-induced vibration of an elastic beam behind a cylinder . 68
3.4 Application: flow through an aortic valve 76
3.5 Conclusion 78

Preliminary remarks

This chapter corresponds to an article entitled "Validation of an immersed thick boundary method for simulating fluid-structure interactions of deformable membranes" [168] which has been published in the *Journal of Computational Physics*, and seeks to extend the features of the YALES2BIO solver to FSI simulations of 3D continuum membranes. Indeed, the membrane mechanics solver introduced in section 1.4 is especially dedicated for solving the red blood cell membrane mechanics, attempting to model its complex microscructure (detailed in section 1.1.2). It notably uses segregated numerical models to take into account the different mechanical properties of the red blood cell membrane, dissociating for example its in-plane

elasticity (coming from the cytoskeleton) to its bending resistance (coming from the lipid bilayer). Such a strategy is however not adapted when modeling 3D continuum membranes, for which all the mechanical effects are coupled and should be taken into account in one single numerical model. A limitation of the IBM is however that it is originally restricted to infinitely thin membranes, making difficult the representation of the bending stiffness. The basic idea is here to flout this limitation, and see how the method performs when the membrane is explicitely represented as a 3D continuum having a finite thickness. Still, the IBM formalism used to communicate between the fluid and solid non-conforming meshes, using the smooth discrete Dirac function, remains identical. The main distinction with the original IBM is that instead of having a triangulated set of Lagrangian markers which represents an infinitely thin membrane, the set of Lagrangian markers defines a 3-dimensional mesh on which the membrane force is solved using the classical finite element method (FEM). A great advantage of this approach is that it does not require to implement a specialized membrane mechanics solver, since the FEM is very common and is implemented in many existing solid mechanics solvers. In this case, the membrane mechanics is solved using the open source LMGC90[1] solver, which is coupled with the YALES2BIO solver, and operates in a reversed way. Indeed, solid mechanics solvers generally solve the displacement of a structure in response to an imposed loading or boundary displacement. In the present IBM framework, the displacement of the whole membrane is prescribed by the surrounding fluid flow, and the solid mechanics solver is used to compute the membrane force relative to this displacement. Adaptation of the IBM framework in the context of 3D structures would be classified as being an immersed domain method (IDM). However, the present approach should rather be considered to be in between the IBM and the IDM, since it attempts to deal with the particular case where the 3D structure is a thin membrane, which raises some relevant questions:

- How robust and accurate is the method when dealing with very thin membranes?
- Does the flexural rigidity of the membrane can be properly taken into account with reasonable mesh resolutions?
- Does the membrane can still be considered as a massless structure despite of its finite thickness?

The present method, referred to as the immersed thick boundary method (ITBM), is described and extensively validated in this chapter. The method is fully described in section 3.2, where the different steps of the IBM are reminded. The smooth discrete Dirac function used to communicate between the fluid and solid non-conforming meshes is notably widely detailed in section 3.2.2, since it constitutes a primary key point in the coupling between the LMGC90 solver and the YALES2BIO solver. A possible application to the simulation of the blood flow through the aortic valve is briefly presented at the end of the chapter, and is further investigated in chapter 4.

[1] https://git-xen.lmgc.univ-montp2.fr/lmgc90/lmgc90_user/wikis/home

3.1 Introduction

Solving the fluid-structure interaction (FSI) problem involved when a membrane is deformed by a flow is a scientific challenge which has been tackled for several decades, due to its wide range of applications. When dealing with numerical simulation of flow-induced deformation of membranes, the state of the art is extremely varied. Different communities work on the topic, focusing on various applications. A large part of these applications are considering deformable particles such as capsules, vesicles or cells. All these systems are constituted by a liquid droplet enclosed by a very thin structure (its thickness is much smaller than the size of the object). This structure can be a polymer structure for capsules, a phospholipid bilayer for vesicles, or a more complex biological membrane in the case of red blood cells [132]. Due to their small size, computations of flows of these deformable particles are often based on boundary integral methods (BIM) [155]. This method can be used for low Reynolds number flows, when the flow is well described by the Stokes equations. The BIM is a very popular technique to compute flows of capsules [11, 12, 54, 105, 158, 194, 203], vesicles [17, 20, 77, 190, 213] and red blood cells [149, 156, 212], because of its precision and its relatively moderate computational cost (only the membranes and boundaries need to be discretized). When the flow is governed by the Navier-Stokes equations, methods with the fluid grid following the deformation of the interface, based on the Arbitrary Lagrangian-Eulerian (ALE) formalism are developed [22, 73, 100]. However, they are not the most popular, as they involve frequent remeshing. Authors generally prefer one-fluid formalisms, where the fluid equations are solved everywhere, over a fixed Eulerian grid. The membrane location is computed by advecting either a function as the level-set function or a second Lagrangian grid following the membrane displacement. One can cite the advected-field approach [15, 18], level-set methods [39, 103, 121, 165] and immersed boundary or immersed interface methods [7, 99, 107, 109, 110, 112, 152, 195].

The immersed boundary method (IBM) was originally developed by Peskin *et al.* [150] and has since been extensively studied and applied to a wide variety of FSI problems. In a previous work, Mendez *et al.* [128] used the IBM to study fluid-structure interaction of deformable particles in flows at arbitrary Reynolds numbers, in the context of complex geometries often encountered when dealing with medical artificial devices. Since this work was only considering the 2D resolution, the main purpose of the present work is to extend it to 3D. The IBM being originally developed to deal with zero volume structures, a membrane-like structure with an infinitely thin thickness can be considered, neglecting the bending stiffness of the membrane. Although suitable when modeling very thin capsules under flow [6, 53], this approach reaches its limitations when considering membranes having a significant bending rigidity. To capture bending effects, an additional model based on the Helfrich energy [88] can be introduced (also used by Mendez *et al.* [128]), and has been notably used to model flowing capsules and red blood cells [8, 206]. Another approach is the one introduced by Le and Tan [107], where the IBM is combined with a thin-shell model to simulate the deformation of liquid capsules under flow [107, 108, 109].

In the present work, another approach to simulate flowing deformable membranes in the context of the IBM is proposed, the immersed thick boundary method (ITBM). This approach is inspired from the extended immersed boundary method (EIBM), introduced by Wang and Liu [195], and later adapted to the immersed finite element method (IFEM) [119, 209]. Instead of the volumeless immersed boundary, a submerged solid which occupies a finite volume within the fluid domain is considered. This approach constitutes an alternative to the one consisting in combining the IBM with a thin shell model. Indeed, rather than representing implicitly the thickness of the membrane using a thin shell model (as Dupont *et al.* [56]), the thickness is represented in an explicit manner, modeling the membrane as a 3D continuum using the classical finite-element method. A full description of the ITBM is done in section 3.2. The use of a classical finite-element framework in the IBM is not generally employed for thin membranes. As a consequence, the present work presents an extensive validation work in section 3.3, in order to thoroughly determine the real limitations of such an approach. The case of very thin membranes will be treated with particular attention. Note that the present approach is not limited to closed membranes. Both closed membranes and open membranes can be simulated using the ITBM, and an application to the flow through a tri-leaflet aortic valve is presented in section 3.4.

3.2 Numerical method

In the IBM framework, two independent meshes are considered to discretize the solid domain Ω_s and the fluid domain Ω_f. The solid is discretized by a moving Lagrangian mesh, and the fluid is discretized by a fixed Eulerian mesh, which can be either structured or unstructured (Fig. 3.1). The different steps of the IBM are the following, as introduced by Peskin [152]:

(1) Knowing the displacement $\overrightarrow{U_m}$ of each solid node, the mechanical force $\overrightarrow{F_m}$ resulting from the membrane deformation is calculated.

(2) The mechanical force $\overrightarrow{F_m}$ is regularized on the fluid mesh, giving the volumetric force $\overrightarrow{f_j}$ on each fluid node.

(3) The Navier-Stokes equations (forced by the regularized mechanical forces) are solved on the fluid mesh, yielding the velocity of the fluid $\overrightarrow{v_j}$ on each fluid node.

(4) The velocity of the membrane $\overrightarrow{V_m}$ on each solid node is interpolated from the $\overrightarrow{v_j}$ field, enabling to deduce the new position $\overrightarrow{X_m}$ from the position at the previous timestep $\overrightarrow{X_m}^{previous}$, such as $\overrightarrow{X_m} = \overrightarrow{X_m}^{previous} + \Delta t \overrightarrow{V_m}$. The displacement is then updated $\overrightarrow{U_m} = \overrightarrow{X_m} - \overrightarrow{X_m^0}$, where $\overrightarrow{X_m^0}$ stands for the initial stress-free position, also referred to as the reference position.

In the present study, step (1) is performed by the LMGC90 solid mechanics solver [157], while steps (2)-(4) are performed by the YALES2BIO numerical tool [34, 128, 215], based on a massively parallel unstructured finite volume flow solver for the incompressible Navier-Stokes equations [140]. Note however that steps (2) and (4)

could be handled by a dedicated coupling program, in the case where modifications in the fluid solver cannot be easily performed. YALES2BIO being an in-house solver, this option was not considered further.

The main distinction between the IBM and the ITBM is that instead of having a cluster of solid nodes spread over a surface, the cluster defines a volume mesh (see Fig. 3.1). The different steps of the ITBM are detailed below.

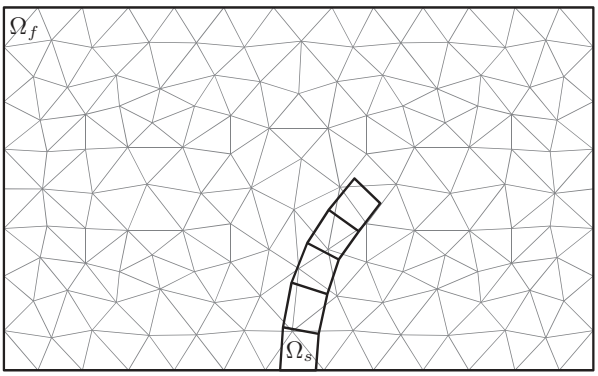

Figure 3.1: Schematic representation of the discretized problem in 2D.

3.2.1 Computation of the mechanical force

When considering immersed volumetric objects, as this is the case with the EIBM [195], the actual structural force to regularize is commonly composed of the internal mechanical force $\overrightarrow{F_m}$ resulting from the static deformation of the structure, and the inertial force $M\overrightarrow{\ddot{U}_m}$ resulting from the dynamics of the structure, the mass matrix M being written as:

$$M = (\rho_s - \rho)\, V, \tag{3.1}$$

where ρ_s and ρ stand for the solid and fluid densities, respectively, and V the volume matrix. When regularizing the structural force, the inertial force should thus be neglected as long as the fluid-to-solid density ratio is close to unity ($\rho_s \simeq \rho$). This assumption is even more true when the solid phase is a very thin membrane ($V \simeq 0$).

The mechanical force $\overrightarrow{F_m}$ is calculated over the three-dimensional mesh representing the solid domain, thanks to the classical finite-element method. Let σ be the cauchy stress tensor, and ϵ the Eulerian-Almansi strain tensor. Using the virtual works principle, it is possible to identify:

$$\overrightarrow{F_m}.\overrightarrow{U_m} = \int_{\Omega_s} \sigma : \epsilon \; d\Omega. \tag{3.2}$$

By using the transformation between the current and the reference configuration of the domain Ω_s^0, the total Lagrangian formulation of the previous equation gives:

$$\overrightarrow{F_m}.\overrightarrow{U_m} = \int_{\Omega_s^0} \mathbb{S} : \mathbb{E} \; d\Omega^0, \tag{3.3}$$

where $\mathbb{S}$ is the 2nd Piola-Kirchhoff stress tensor, and $\mathbb{E}$ is the Green-Lagrangian strain tensor, which reads:

$$\mathbb{E} = \frac{1}{2}\left(\mathbb{C} - \mathbb{I}\right), \tag{3.4}$$

with $\mathbb{C} = \mathbb{F}^T\mathbb{F}$ the Right Cauchy-Green deformation tensor, and $\mathbb{F} = \mathbb{I} + \overline{\overline{\nabla}}\,\overrightarrow{U_m}$ the deformation gradient tensor. The right-hand side of Eq. (3.3) can be rewritten as the scalar product of the equivalent vector forms of $\mathbb{S}$ and $\mathbb{E}$:

$$\overrightarrow{F_m}.\overrightarrow{U_m} = \int_{\Omega_s^0} \overrightarrow{S}.\overrightarrow{E}\; d\Omega^0. \tag{3.5}$$

Introducing the gradient matrix $\mathcal{B}$ which contains the spatial derivatives of the shape functions, Eq. (3.5) becomes:

$$\overrightarrow{F_m}.\overrightarrow{U_m} = \int_{\Omega_s^0} \overrightarrow{S}.\;\mathcal{B}\;\overrightarrow{U_m}\; d\Omega^0. \tag{3.6}$$

Eliminating $\overrightarrow{U_m}$ on both sides and discretizing the domain as a sum of elements $\Omega_s^0 = \cup\,\Omega_{el}^0$, one finally obtains:

$$\overrightarrow{F_m} = \sum_{\Omega_{el}^0} \left[\int_{\Omega_{el}^0} \overrightarrow{S}.\;\mathcal{B}\; d\Omega^0\right]. \tag{3.7}$$

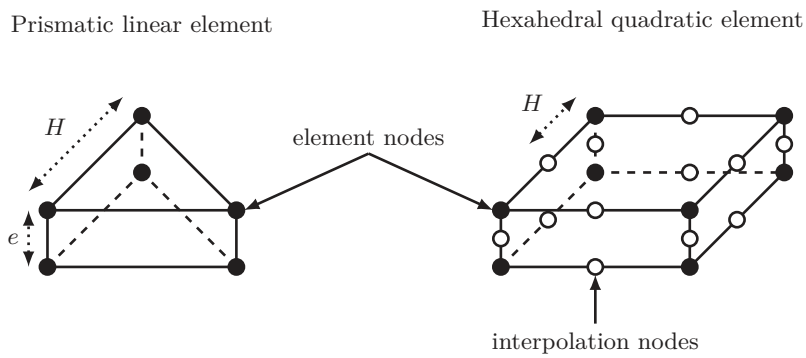

Figure 3.2: **Left:** Prismatic linear element where linear shape functions are defined between two element nodes. **Right:** Hexahedral quadratic element. Interpolation nodes are needed to define the quadratic shape functions.

In the present work, both prismatic linear elements (see Fig. 3.2, left) and hexahedral quadratic elements (see Fig. 3.2, right) are tested. In the case of linear elements, the linear shape function is defined between two elements nodes. And in the case of quadratic elements, an interpolation node between two element nodes is needed to define the quadratic shape function. The effective resolution H of the elements is introduced, as being the biggest distance between two nodes (between two element nodes in the case of linear elements, and between one element node and one interpolation node in the case of quadratic elements). Note that in the case of linear elements, the effective resolution H is equal to the element resolution, and to half of the element resolution in the case of quadratic elements. If the membrane

thickness e is smaller than the element resolution (as this is the case in Fig. 3.2), the membrane is meshed only with one element in the thickness. But if the element resolution is smaller than the membrane thicknes e, the number of elements in the thickness is greater than one.

Constitutive laws

The LMGC90 computational code features a wide library of constitutive laws. Only a few of them are used in the present work:

- The compressible Saint-Venant Kirchoff law

$$\mathbb{S} = \frac{2G\nu}{1-2\nu}\,\mathrm{Tr}\,(\mathbb{E})\,\mathbb{I} + 2G\mathbb{E}, \tag{3.8}$$

where G and ν are the shear modulus and the Poisson coefficient, respectively.

- The compressible Neo-Hookean law, as introduced by Simo and Pister [172]

$$\begin{cases} \mathbb{S} = 2\dfrac{\partial W}{\partial \mathbb{C}} \\ W = \dfrac{G}{2}\left(I_1 - 3\right) - G\ln J + \dfrac{G\nu}{1-2\nu}\left(\ln J\right)^2 \end{cases} \tag{3.9}$$

where W is the strain energy density function. $J = \det \mathbb{F} = \lambda_1\lambda_2\lambda_3$ is the Jacobian of the transformation, expressed as the product of the principal stretches λ_i and I_1 is the first invariant of the Right Cauchy-Green deformation tensor $\mathbb{C}$, which reads:

$$I_1 = \lambda_1^2 + \lambda_2^2 + \lambda_3^2. \tag{3.10}$$

- The quasi-incompressible Yeoh law

$$\begin{cases} \mathbb{S} = 2\dfrac{\partial W}{\partial \mathbb{C}} \\ W = C_1\left(\bar{I}_1 - 3\right) + C_2\left(\bar{I}_1 - 3\right)^2 + C_3\left(\bar{I}_1 - 3\right)^3 + \dfrac{G\left(1+\nu\right)}{3\left(1-2\nu\right)}\left(\ln J\right)^2 \end{cases} \tag{3.11}$$

where C_i are material constants and $\bar{I}_1$ is the first invariant of the isochoric Right Cauchy-Green deformation tensor $\bar{\mathbb{C}}$, such as $\bar{I}_1 = J^{-2/3}I_1$. The quantity $2C_1$ can be interpreted to be the shear modulus G, and when C_2 and C_3 are chosen to be $C_2 = C_3 = 0$, this leads to the quasi-incompressible Neo-Hookean law.

3.2.2 Forces regularization

The force per unit volume applied on the fluid by the membrane is computed from the mechanical forces on the solid nodes, through the process of force regularization:

$$\overrightarrow{f_j} = \sum_{m=1}^{M}\left[\overrightarrow{F_m} \times w\left(\frac{||\overrightarrow{x_j} - \overrightarrow{X_m}||}{h}\right)\right], \tag{3.12}$$

where w is a discrete Dirac function allowing to regularize the mechanical force at the neighboring fluid nodes from the mechanical force at the solid node location (Fig. 3.3).

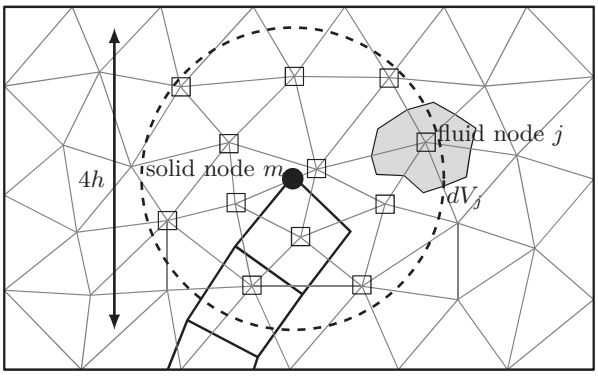

Figure 3.3: Schematic representation of the procedure to compute the window function w.

When using a regular Cartesian mesh of constant mesh size h, the discrete Dirac function w can be easily defined as the product of one-dimensional delta functions:

$$w\left(\frac{||\overrightarrow{x_j}-\overrightarrow{X_m}||}{h}\right)=D\left(\frac{x_j-X_m}{h}\right)D\left(\frac{y_j-Y_m}{h}\right)D\left(\frac{z_j-Z_m}{h}\right). \tag{3.13}$$

The cosine representation is often used, as introduced by Peskin [152]:

$$D(r)=\begin{cases}\dfrac{1}{4h}\left[1+\cos\left(\dfrac{\pi r}{2}\right)\right] & \text{if } |r|<2\\[2ex] 0 & \text{if } |r|\geq 2\end{cases} \tag{3.14}$$

When using unstructured meshes, the Cartesian version of w cannot be used. Adaptation of the immersed boundary formalism to unstructured meshes relies on the Reproducing Kernel Particle Method [117, 128, 153]. The intensity and the point of application of the force to regularize have to be ensured by the chosen discrete Dirac function w. To this respect, it proves useful to introduce the moments of the window function w at the location of the solid node m:

$$\begin{aligned}m_{a,b,c}(\overrightarrow{X_m})=\sum_{j=1}^{J}\Bigg[&\left(\frac{x_j-X_m}{h}\right)^a\left(\frac{y_j-Y_m}{h}\right)^b\left(\frac{z_j-Z_m}{h}\right)^c\\ &\times w\left(\frac{||\overrightarrow{x_j}-\overrightarrow{X_m}||}{h}\right)dV_j\Bigg].\end{aligned} \tag{3.15}$$

For a unit point force applied at coordinates $\overrightarrow{X_m}$, moments calculated at $\overrightarrow{X_m}$ are known: the first moment $m_{0,0,0}$ is 1, and the following ones are all 0.

When using unstructured meshes, the following isotropic extension of Eqs. (3.13)-(3.14) is naturally introduced:

$$w\left(\frac{||\overrightarrow{x_j}-\overrightarrow{X_m}||}{h}\right)=w(r)=\begin{cases}\frac{1}{2^{dim-1}}\frac{1}{4h}\left[1+\cos\left(\frac{\pi r}{2}\right)\right] & \text{if } |r|<2\\ 0 & \text{if } |r|\geq 2\end{cases} \tag{3.16}$$

Since the resulting regularized force $\overrightarrow{f_j}$ does not meet the moment condition ($m_{a,b,c}=0$ except $m_{0,0,0}=1$), a modified weight function for regularization is introduced:

$$\begin{aligned}\overline{w}\left(\frac{||\overrightarrow{x_j}-\overrightarrow{X_m}||}{h}\right)&=w\left(\frac{||\overrightarrow{x_j}-\overrightarrow{X_m}||}{h}\right)\times\left[\beta_0+\beta_1\frac{x_j-X_m}{h}\right.\\&\left.+\beta_2\frac{y_j-Y_m}{h}+\beta_3\frac{z_j-Z_m}{h}\right],\end{aligned} \tag{3.17}$$

where β_k are the coefficients of the polynomial correction of the original window function. The moments of the modified window function are then given by:

$$\begin{aligned}\overline{m_{a,b,c}}(\overrightarrow{X_m})&=\sum_{j=1}^{J}\left[\left(\frac{x_j-X_m}{h}\right)^a\left(\frac{y_j-Y_m}{h}\right)^b\left(\frac{z_j-Z_m}{h}\right)^c\right.\\&\left.\times\overline{w}\left(\frac{||\overrightarrow{x_j}-\overrightarrow{X_m}||}{h}\right)dV_j\right].\end{aligned} \tag{3.18}$$

By plugging the definition of $\overline{w}$ into Eq. (3.18), one easily obtains that:

$$\begin{pmatrix}\overline{m_{0,0,0}}\\ \overline{m_{1,0,0}}\\ \overline{m_{0,1,0}}\\ \overline{m_{0,0,1}}\end{pmatrix}=\begin{pmatrix}m_{0,0,0} & m_{1,0,0} & m_{0,1,0} & m_{0,0,1}\\ m_{1,0,0} & m_{2,0,0} & m_{1,1,0} & m_{1,0,1}\\ m_{0,1,0} & m_{1,1,0} & m_{0,2,0} & m_{0,1,1}\\ m_{0,0,1} & m_{1,0,1} & m_{0,1,1} & m_{0,0,2}\end{pmatrix}\begin{pmatrix}\beta_0\\ \beta_1\\ \beta_2\\ \beta_3\end{pmatrix}=\mathcal{M}\begin{pmatrix}\beta_0\\ \beta_1\\ \beta_2\\ \beta_3\end{pmatrix}, \tag{3.19}$$

where $\mathcal{M}$ contains the moments of the isotropic window function w (Eq. (3.16)). The first moments of the modified window function can then be imposed to their expected values $(1,0,0,0)$ by calculating β_k such as:

$$\begin{pmatrix}\beta_0\\ \beta_1\\ \beta_2\\ \beta_3\end{pmatrix}=\mathcal{M}^{-1}\begin{pmatrix}\overline{m_{0,0,0}}\\ \overline{m_{1,0,0}}\\ \overline{m_{0,1,0}}\\ \overline{m_{0,0,1}}\end{pmatrix}=\mathcal{M}^{-1}\begin{pmatrix}1\\ 0\\ 0\\ 0\end{pmatrix}. \tag{3.20}$$

In this case, the modified window function ensures that the moment of order 0 is equal to 1, and the moments of order 1 are equal to 0. To also impose the moments of order 2 to 0, the original window function has to be corrected with a quadratic

correction leading to the calculation of 10 β_k coefficients [153]:

$$\begin{aligned}
\overline{w}\left(\frac{||\overrightarrow{x_j}-\overrightarrow{X_m}||}{h}\right) &= w\left(\frac{||\overrightarrow{x_j}-\overrightarrow{X_m}||}{h}\right)\times\Bigg[\beta_0+\beta_1\frac{x_j-X_m}{h} \\
&+\beta_2\frac{y_j-Y_m}{h}+\beta_3\frac{z_j-Z_m}{h}+\beta_4\left(\frac{x_j-X_m}{h}\right)\left(\frac{y_j-Y_m}{h}\right) \\
&+\beta_5\left(\frac{y_j-Y_m}{h}\right)\left(\frac{z_j-Z_m}{h}\right)+\beta_6\left(\frac{z_j-Z_m}{h}\right)\left(\frac{x_j-X_m}{h}\right) \\
&+\beta_7\left(\frac{x_j-X_m}{h}\right)^2+\beta_8\left(\frac{y_j-Y_m}{h}\right)^2+\beta_9\left(\frac{z_j-Z_m}{h}\right)^2\Bigg],
\end{aligned} \tag{3.21}$$

leading to:

$$\begin{pmatrix}\overline{m_{0,0,0}}\\ \overline{m_{1,0,0}}\\ \overline{m_{0,1,0}}\\ \overline{m_{0,0,1}}\\ \overline{m_{1,1,0}}\\ \overline{m_{0,1,1}}\\ \overline{m_{1,0,1}}\\ \overline{m_{2,0,0}}\\ \overline{m_{0,2,0}}\\ \overline{m_{0,0,2}}\end{pmatrix} = \begin{pmatrix} m_{0,0,0} & m_{1,0,0} & \cdots & m_{0,0,2}\\ m_{1,0,0} & m_{2,0,0} & \cdots & m_{1,0,2}\\ \vdots & \vdots & \ddots & \vdots\\ m_{0,0,2} & m_{1,0,2} & \cdots & m_{0,0,4}\end{pmatrix}\begin{pmatrix}\beta_0\\ \beta_1\\ \beta_2\\ \beta_3\\ \beta_4\\ \beta_5\\ \beta_6\\ \beta_7\\ \beta_8\\ \beta_9\end{pmatrix} = \mathcal{M}\begin{pmatrix}\beta_0\\ \beta_1\\ \beta_2\\ \beta_3\\ \beta_4\\ \beta_5\\ \beta_6\\ \beta_7\\ \beta_8\\ \beta_9\end{pmatrix}. \tag{3.22}$$

The coefficients β_k are thus given by:

$$\begin{pmatrix}\beta_0\\ \beta_1\\ \beta_2\\ \beta_3\\ \beta_4\\ \beta_5\\ \beta_6\\ \beta_7\\ \beta_8\\ \beta_9\end{pmatrix} = \mathcal{M}^{-1}\begin{pmatrix}\overline{m_{0,0,0}}\\ \overline{m_{1,0,0}}\\ \overline{m_{0,1,0}}\\ \overline{m_{0,0,1}}\\ \overline{m_{1,1,0}}\\ \overline{m_{0,1,1}}\\ \overline{m_{1,0,1}}\\ \overline{m_{2,0,0}}\\ \overline{m_{0,2,0}}\\ \overline{m_{0,0,2}}\end{pmatrix} = \mathcal{M}^{-1}\begin{pmatrix}1\\ 0\\ 0\\ 0\\ 0\\ 0\\ 0\\ 0\\ 0\\ 0\end{pmatrix}. \tag{3.23}$$

At the end, computing the regularized force as:

$$\overrightarrow{f_j} = \sum_{m=1}^{M}\left[\overrightarrow{F_m}\times\overline{w}\left(\frac{||\overrightarrow{x_j}-\overrightarrow{X_m}||}{h}\right)\right], \tag{3.24}$$

allows a proper representation of the membrane force location, and moments up to second order. Although possible in principle, the proper representation of higher order moments is not considered in this study.

3.2.3 Navier-Stokes equations resolution

A massively parallel unstructured finite-volume flow solver is used to solve the forced Navier-Stokes equations over the Eulerian mesh using a projection method [37]. The momentum conservation equations reads:

$$\frac{\partial \overrightarrow{v_j}}{\partial t} + \overrightarrow{\nabla}.(\overrightarrow{v_j} \otimes \overrightarrow{v_j}) = -\frac{\overrightarrow{\nabla} p_j}{\rho} + \nu \Delta \overrightarrow{v_j} + \frac{\overrightarrow{f_j}}{\rho}, \tag{3.25}$$

where $\overrightarrow{v_j}$ and p_j are the velocity vector and pressure on fluid node j, ρ the density and ν the kinematic viscosity. For an incompressible flow, the mass conservation constraint becomes:

$$\overrightarrow{\nabla}.\overrightarrow{v_j} = 0. \tag{3.26}$$

The fluid velocity is first advanced using a 4th-order central scheme in space and a 4th-order Runge-Kutta scheme in time. A divergence-free velocity field is obtained at the end of the time-step by solving a Poisson equation for pressure and correcting the predicted velocity. A Deflated Preconditioned Conjugate Gradient algorithm is used to solve this Poisson equation. More details about the employed numerical methods can be found in [123, 140].

3.2.4 Membrane convection

Adherence of the fluid over the membrane makes the fluid velocity continuous at the membrane location and equal to the membrane velocity. Thus, the velocity $\overrightarrow{V_m}$ of the solid node m is calculated by interpolating the fluid velocity at the solid nodes location from the fluid velocity at the neighboring fluid nodes:

$$\overrightarrow{V_m} = \sum_{j=1}^{J} \left[\overrightarrow{v_j} \times \overline{w} \left(\frac{||\overrightarrow{x_j} - \overrightarrow{X_m}||}{h} \right) dV_j \right]. \tag{3.27}$$

This interpolation process again involves the use of the discrete Dirac function $\overline{w}$, which is defined in the same manner as in the forces regularization process described in section 3.2.2.

3.2.5 Discretization

When using immersed boundary methods, authors generally recommend the use of similar solid and fluid mesh discretizations. Numerical experiences showed that the present method performs well when the ratio h/H between the fluid mesh resolution and the solid effective resolution is such that $0.5 < h/H < 2$. An initial ratio $h/H \approx 1$ is typically suited to start with.

3.2.6 Volume correction

The original immersed boundary method tends to suffer from a small leakage problem. Indeed, whatever the choice made for the window function, interpolation does not conserve the divergence-free character of the carrying fluid flow [152]. This issue is sometimes pointed out as a major drawback of the IBM [112].

When dealing with closed membranes, this leakage problem results in a non conservation of the volume enclosed by the flexible membrane. In this case, the volume can be corrected by using a Lagrange Multiplier method. This procedure is detailed in [128] in the case of 2D particles, and is here generalized for 3D particles. Such a correction is however not possible when dealing with open membranes. In the present ITBM, this procedure is performed by constructing a triangulation of the middle surface of the membrane, which however limits its use to linear prismatic elements, but will be later adapted for quadratic hexahedral elements.

The Lagrange Multiplier method is used to find the smallest correction that should be applied to the solid nodes location in order to ensure the conservation of the particle volume. The membrane middle surface is composed of F triangular elements, and M Lagrangian markers. Each face f has three markers f_1, f_2 and f_3. The volume enclosed by the membrane middle surface can be calculated as:

$$V\left(\underline{\underline{X}}\right) = \frac{1}{18}\sum_{f=1}^{F}\left[\overrightarrow{X_{f_1}}.\left(\overrightarrow{X_{f_2}}\times\overrightarrow{X_{f_3}}\right)+\overrightarrow{X_{f_2}}.\left(\overrightarrow{X_{f_3}}\times\overrightarrow{X_{f_1}}\right)+\right.$$
$$\left.\overrightarrow{X_{f_3}}.\left(\overrightarrow{X_{f_1}}\times\overrightarrow{X_{f_2}}\right)\right]. \tag{3.28}$$

At the beginning of the calculation, the volume of the particle V_0 is calculated. At the end of each time step, the coordinates of the Lagrangian markers $\underline{\underline{X}}$ are predicted, after time advancement of the solid nodes position. As already stated, $V\left(\underline{\underline{X}}\right) \neq V_0$ since the interpolation does not conserve the divergence-free character of the velocity field.

The aim is then to find the smallest markers displacements $\underline{\underline{\delta X}}$ in norm, so that $V\left(\underline{\underline{X}}^{corr}\right) = V_0$, where $\underline{\underline{X}}^{corr} = \underline{\underline{X}} + \underline{\underline{\delta X}}$ denotes the matrix containing the final coordinates. Introducing a Lagrange multiplier Λ, the sought correction displacements $\underline{\underline{\delta X}}$ minimize the following cost function:

$$J_\Lambda\left(\underline{\underline{\delta X}}\right) = \sum_{m=1}^{M}\left[(\delta X_m)^2+(\delta Y_m)^2+(\delta Z_m)^2\right]+\Lambda\left[V\left(\underline{\underline{X}}+\underline{\underline{\delta X}}\right)-V_0\right]. \tag{3.29}$$

Zeroing the partial derivatives of J_Λ with respect to the location correction (δX_m, δY_m, δZ_m) of the Lagrangian marker m leads to:

$$\begin{cases} 2\delta X_m + \Lambda\dfrac{\partial V\left(\underline{\underline{X}}+\underline{\underline{\delta X}}\right)}{\partial \delta X_m} = 0 \\ 2\delta Y_m + \Lambda\dfrac{\partial V\left(\underline{\underline{X}}+\underline{\underline{\delta X}}\right)}{\partial \delta Y_m} = 0 \\ 2\delta Z_m + \Lambda\dfrac{\partial V\left(\underline{\underline{X}}+\underline{\underline{\delta X}}\right)}{\partial \delta Z_m} = 0 \end{cases} \tag{3.30}$$

with:

$$\frac{\partial V\left(\underline{\underline{X}}+\underline{\underline{\delta X}}\right)}{\partial \delta X_m}=\frac{1}{6}\left[\sum_{f:\,m=f_1}\frac{\partial\left(\overrightarrow{X_{f_1}}+\overrightarrow{\delta X_{f_1}}\right)}{\partial \delta X_m}\left[\left(\overrightarrow{X_{f_2}}+\overrightarrow{\delta X_{f_2}}\right)\times\left(\overrightarrow{X_{f_3}}\right.\right.\right.$$

$$\left.\left.+\overrightarrow{\delta X_{f_3}}\right)\right]+\sum_{f:\,m=f_2}\frac{\partial\left(\overrightarrow{X_{f_2}}+\overrightarrow{\delta X_{f_2}}\right)}{\partial \delta X_m}\left[\left(\overrightarrow{X_{f_3}}+\overrightarrow{\delta X_{f_3}}\right)\times\left(\overrightarrow{X_{f_1}}+\overrightarrow{\delta X_{f_1}}\right)\right] \tag{3.31}$$

$$\left.+\sum_{f:\,m=f_3}\frac{\partial\left(\overrightarrow{X_{f_3}}+\overrightarrow{\delta X_{f_3}}\right)}{\partial \delta X_m}\left[\left(\overrightarrow{X_{f_1}}+\overrightarrow{\delta X_{f_1}}\right)\times\left(\overrightarrow{X_{f_2}}+\overrightarrow{\delta X_{f_2}}\right)\right]\right].$$

Assuming that the correction displacements are small, so that $\overrightarrow{X_m}+\overrightarrow{\delta X_m}\approx\overrightarrow{X_m}$, one obtains:

$$\overrightarrow{\delta X_m}=\Lambda\,\overrightarrow{\alpha_m}, \tag{3.32}$$

with:

$$\overrightarrow{\alpha_m}=-\frac{1}{12}\left[\sum_{f:\,m=f_1}\left(\overrightarrow{X_{f_2}}\times\overrightarrow{X_{f_3}}\right)+\sum_{f:\,m=f_2}\left(\overrightarrow{X_{f_3}}\times\overrightarrow{X_{f_1}}\right)\right.$$
$$\left.+\sum_{f:\,m=f_3}\left(\overrightarrow{X_{f_1}}\times\overrightarrow{X_{f_2}}\right)\right]. \tag{3.33}$$

When J_Λ is minimum, $\partial J_\Lambda/\partial\Lambda=0$, which means that $V\left(\underline{\underline{X}}+\underline{\underline{\delta X}}\right)=V_0$. Equations (3.28) and (3.32) thus lead to:

$$\frac{1}{18}\sum_{f=1}^{F}\left[\left(\overrightarrow{X_{f_1}}+\Lambda\,\overrightarrow{\alpha_{f_1}}\right).\left[\left(\overrightarrow{X_{f_2}}+\Lambda\,\overrightarrow{\alpha_{f_2}}\right)\times\left(\overrightarrow{X_{f_3}}+\Lambda\,\overrightarrow{\alpha_{f_3}}\right)\right]\right.$$
$$+\left(\overrightarrow{X_{f_2}}+\Lambda\,\overrightarrow{\alpha_{f_2}}\right).\left[\left(\overrightarrow{X_{f_3}}+\Lambda\,\overrightarrow{\alpha_{f_3}}\right)\times\left(\overrightarrow{X_{f_1}}+\Lambda\,\overrightarrow{\alpha_{f_1}}\right)\right] \tag{3.34}$$
$$\left.+\left(\overrightarrow{X_{f_3}}+\Lambda\,\overrightarrow{\alpha_{f_3}}\right).\left[\left(\overrightarrow{X_{f_1}}+\Lambda\,\overrightarrow{\alpha_{f_1}}\right)\times\left(\overrightarrow{X_{f_2}}+\Lambda\,\overrightarrow{\alpha_{f_2}}\right)\right]\right]-V_0=0.$$

After some algebra, the following third-order polynomial equation in Λ is obtained: $A\Lambda^3+B\Lambda^2+C\Lambda+D=0$, with:

$$A=\frac{1}{18}\sum_{f=1}^{F}\left[\overrightarrow{\alpha_{f_1}}.\left(\overrightarrow{\alpha_{f_2}}\times\overrightarrow{\alpha_{f_3}}\right)+\overrightarrow{\alpha_{f_2}}.\left(\overrightarrow{\alpha_{f_3}}\times\overrightarrow{\alpha_{f_1}}\right)+\overrightarrow{\alpha_{f_3}}.\left(\overrightarrow{\alpha_{f_1}}\times\overrightarrow{\alpha_{f_2}}\right)\right], \tag{3.35}$$

$$B=\frac{1}{6}\sum_{f=1}^{F}\left[\overrightarrow{X_{f_1}}.\left(\overrightarrow{\alpha_{f_2}}\times\overrightarrow{\alpha_{f_3}}\right)+\overrightarrow{X_{f_2}}.\left(\overrightarrow{\alpha_{f_3}}\times\overrightarrow{\alpha_{f_1}}\right)+\overrightarrow{X_{f_3}}.\left(\overrightarrow{\alpha_{f_1}}\times\overrightarrow{\alpha_{f_2}}\right)\right], \tag{3.36}$$

$$C=\frac{1}{6}\sum_{f=1}^{F}\left[\overrightarrow{\alpha_{f_1}}.\left(\overrightarrow{X_{f_2}}\times\overrightarrow{X_{f_3}}\right)+\overrightarrow{\alpha_{f_2}}.\left(\overrightarrow{X_{f_3}}\times\overrightarrow{X_{f_1}}\right)+\overrightarrow{\alpha_{f_3}}.\left(\overrightarrow{X_{f_1}}\times\overrightarrow{X_{f_2}}\right)\right], \tag{3.37}$$

$$D=V\left(\underline{\underline{X}}\right)-V_0. \tag{3.38}$$

This third-order polynomial equation is then solved numerically and Λ is computed as the real valued root (there is always one at least) of smallest amplitude. Once Λ is

found, the Lagrangian markers positions are updated to ensure volume conservation, as follows:

$$\overrightarrow{X_m} \rightarrow \overrightarrow{X_m} + \Lambda \, \overrightarrow{\alpha_m}. \tag{3.39}$$

3.3 Verification and validation

This section is dedicated to the verification and the validation of the present method. Table 3.1 summarizes the selection of the test cases considered in this respect. Test cases of sections 3.3.1 and 3.3.2 should be considered as verification test cases, whereas the other test cases are more challenging and are referred to as validation test cases.

Test case (section)	Diagram	Reference data
Non-linear bending of an elastic plate (section 3.3.1)		Numerical results from Sze *et al.* (2004) [186]
Inflation of a spherical capsule (section 3.3.2)	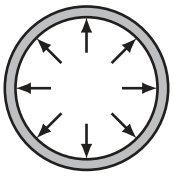	Analytical solution
Capsule in a linear shear flow (section 3.3.3)	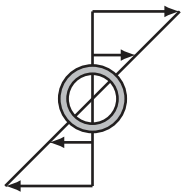	Numerical results from Lac *et al.* (2004) [104]
Red blood cell stretched by optical tweezers (section 3.3.4)	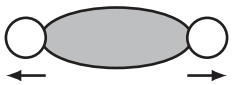	Experimental data from Mills *et al.* (2004) [131]
Flow-induced vibration of an elastic beam behind a cylinder (section 3.3.5)	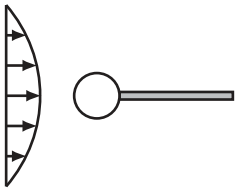	Numerical results from Turek and Hron (2006) [187] and Turek *et al.* (2010) [188]

Table 3.1: Summary of the validation test cases presented in section 3.3.

3.3.1 Non-linear bending of an elastic plate

The principle of this test case is to look at the mechanical equilibrium of a plate. As shown in Fig. 3.4, the plate is defined by its length L, width l and thickness e. One of its extremities is fixed, while the other is loaded by applying a force F, normal to the initial position of the plate. The objective is to verify that the

mechanical equilibrium obtained by the FSI computation is the same as the one from a simple structural computation, performed with the LMGC90 solid mechanics solver. Although it appears trivial, this test case is actually a good mean to verify the operation of the coupling algorithm. Indeed, FSI and structural resolutions are completely different insofar as the displacement of the structure $\overrightarrow{U_m}$ is solved during the structural computation, whereas in the FSI computation the displacement is imposed by the velocity of the fluid, the only contribution of the solid mechanics solver being to compute the mechanical force $\overrightarrow{F_m}$ resulting from this imposed displacement. In this context, the errors generated by the procedures of forces regularization (section 3.2.2) and membrane convection (section 3.2.4) could potentially impact the mechanical equilibrium of the plate.

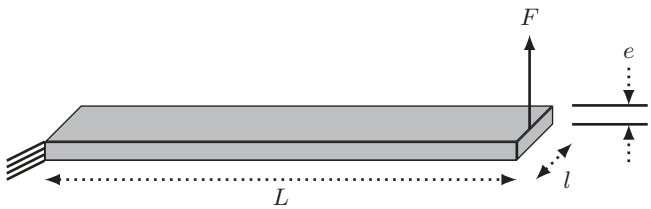

Figure 3.4: Geometrical parameters of the plate. The force F is applied over all the surface of the plate extremity.

Structural computation

The static structural problem is first solved using the LMGC90 solid mechanics solver, giving the mechanical equilibrium of the plate. The plate is modeled by a Neo-Hookean material (Eq. (3.9)). The parameters used for this computation are the same of those used in the benchmark test proposed by Sze *et al.* (2004) [186], and are given in Tab. 3.2.

F	L	l	e	E	ν
4 N	10 m	1 m	0.1 m	1.2 10^6 Pa	0

Table 3.2: Parameters of the benchmark test case proposed by Sze *et al.* (2004) [186].

In order to study the influence of the finite element interpolation, both linear hexahedral finite elements and quadratic hexahedral finite elements are compared with the reference result of Sze *et al.* (2004) [186]. Figure 3.5 (left) shows the maximal displacement (in the direction of the applied force) obtained at the extremity of the plate, for different mesh resolutions. It is seen that the chosen interpolation has a strong influence on the final result. Indeed, the numerical solution converge much faster when the quadratic interpolation is chosen. When using quadratic elements, the solution reaches a constant relative difference of 0.45% with respect to the reference result. For the linear interpolation, the solution is not yet converged when reaching the maximal number of elements, and a final relative difference of 14.15%

is obtained. It appears that, with linear elements, flexural deformation cannot be properly simulated without using very fine mesh resolutions. In contrast, quadratic elements offer a better accuracy even with a coarse mesh. Regarding the relative convergence error (see Fig. 3.5, right) calculated from the most refined computation, it is seen that the order of convergence for both the linear and the quadratic interpolation is retrieved.

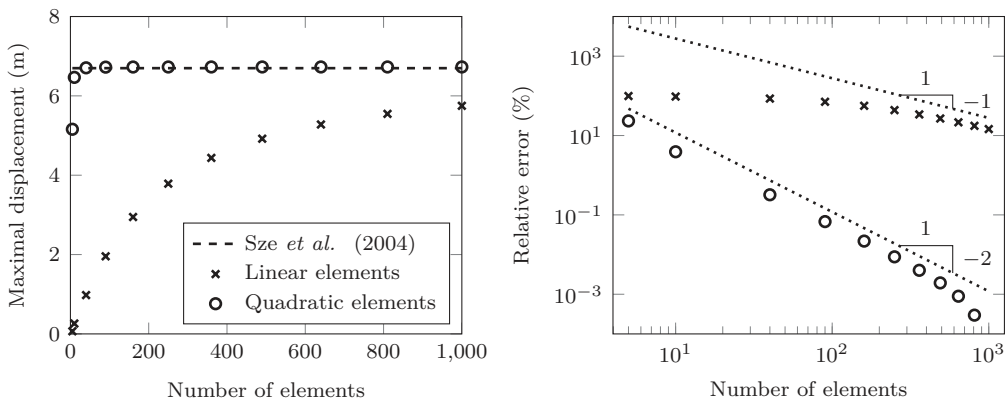

Figure 3.5: **Left:** Evolution of the maximal displacement as a function of the number of elements. Results obtained with both linear and quadratic hexahedral finite elements are compared with the result of Sze *et al.* (2004) [186]. **Right:** Error relative to the most refined computation.

Fluid-structure interaction computation

The next step is to perform a FSI computation, and compare the result with the one obtained in the structural computation. A time dependent FSI problem is solved, by immersing the plate in a fluid computational domain (Fig. 3.6, left). The fluid box is extended from 0 to $1.15L$ in length, from -$2l$ to $2l$ in width, and from -$15e$ to $85e$ in height. The fluid mesh is an unstructured tetrahedral mesh of 23 174 elements, with a constant resolution of $h = 0.5$ m. The plate is meshed using 10 quadratic hexahedral elements (second point in Fig. 3.5), with an effective resolution of $H = 0.5$ m. Note that in this case, the ratio between the fluid mesh resolution and the thickness of the membrane is $h/e = 5$.

At each iteration, the external force F is added to the calculated mechanical force $\overrightarrow{F_m}$. This external force is distributed over the solid nodes located at the extremity of the plate. As the mechanical force, the applied external force is regularized on the fluid grid (see section 3.2.2), resulting in a motion of the fluid. The displacement of the plate is then calculated during the step of membrane convection (see section 3.2.4). It is thus the motion of the fluid which enables to the plate to deform and reach the equilibrium position.

Figure 3.6 shows the deformation of the plate (left) and the time evolution of the maximal displacement of the plate extremity from the FSI computation (right). Ap-

plying the loading first puts the plate in motion until a steady state is finally reached. Once the fluid is at rest, the plate reaches its mechanical equilibrium. This equilibrium is compared with the equilibrium given by the structural computation. The comparison has been done for both first order and second order corrections for the computation of the window function (see section 3.2.2), leading to the same result: for the given rounding precision (three decimal places), the maximal displacement given by the FSI computation is strictly the same of the one from the structural computation. When increasing the ratio h/e up to 1000, FSI and structural computations still provide identical mechanical equilibriums (not shown), showing that the present method is able to simulate membranes having a thickness much smaller than the fluid mesh resolution.

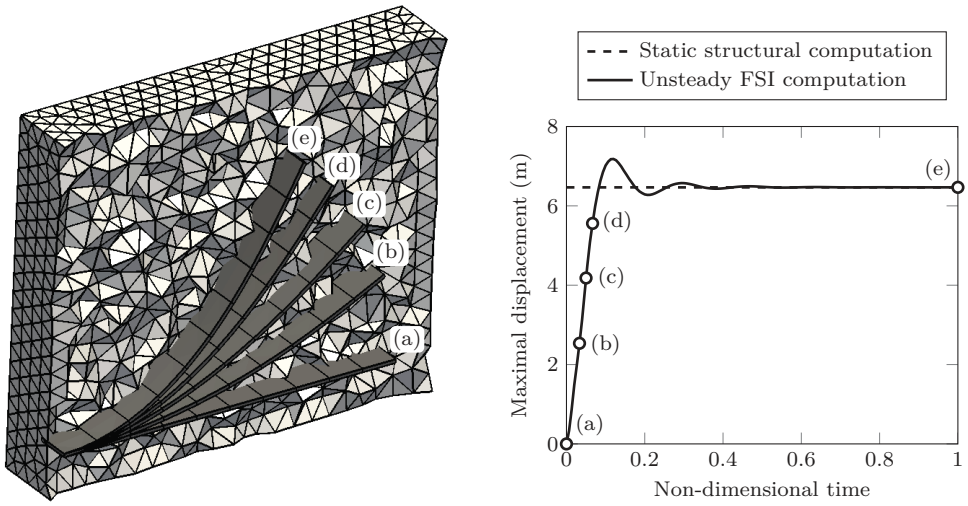

Figure 3.6: **Left:** Visualization of the plate deformation within the fluid box. **Right:** Evolution of the maximal displacement of the plate extremity. The FSI computation is compared with the structural computation.

3.3.2 Inflation of a spherical capsule

In this section, the inflation of a spherical capsule is considered. The capsule is defined by its internal and external radii, respectively R_i and R_e (Fig. 3.7, left). An elastic linear isotropic material is used, defined by its Young modulus E and Poisson coefficient ν. When submitted to an internal pressure P, the capsule deforms (Fig. 3.7, right). Within the assumption of small perturbations, it is possible to derive an analytical solution of the radial displacement of the capsule submitted to the internal pressure P:

$$U_r\left(r\right) = \frac{{R_i}^3}{{R_e}^3 - {R_i}^3}\left[\left(1-2\nu\right)r + \left(1+\nu\right)\frac{{R_e}^3}{2r^2}\right]\frac{P}{E}, \tag{3.40}$$

with $R_i < r < R_e$.

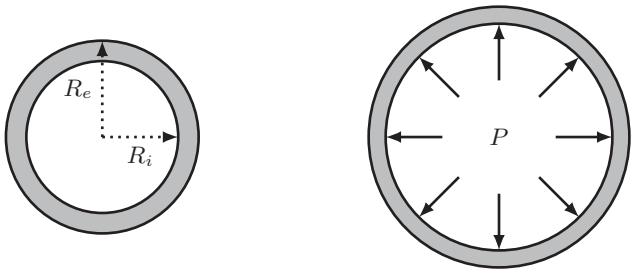

Figure 3.7: A spherical capsule of internal radius R_i and external radius R_e is inflated applying an internal pressure P.

Structural computation

As in the previous test case, the structural problem is first solved using the LMGC90 solid mechanics solver. The values of the physical parameters are given in Tab. 3.3, where e and R denote the thickness and mean radius of the capsule, respectively.

P	e	R	R_i	R_e	E	ν
500 Pa	0.05 m	0.5 m	$R - e/2$	$R + e/2$	1.5 10^6 Pa	0.4

Table 3.3: Parameters chosen for the structural computation.

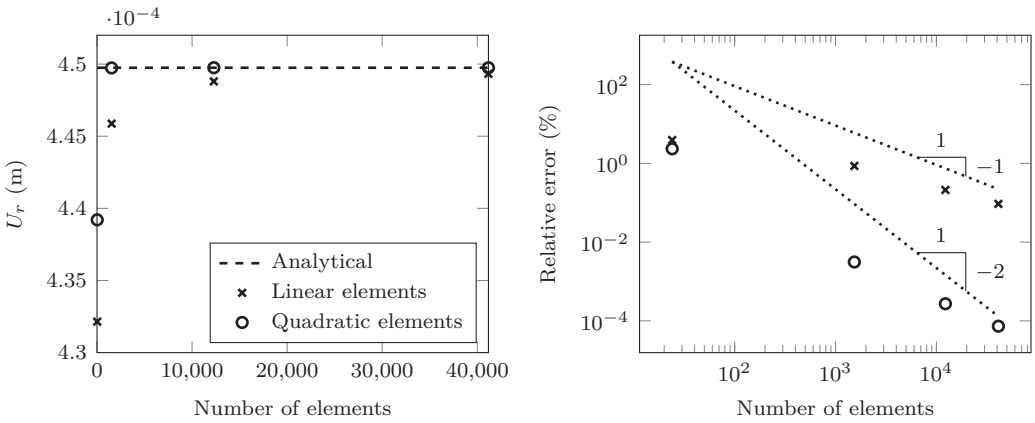

Figure 3.8: **Left:** Evolution of the radial displacement as a function of the number of elements. Results obtained with both linear and quadratic hexahedral finite elements are compared with the analytical solution. **Right:** Relative error for both linear and quadratic interpolations.

Here again, the influence of the finite-element interpolation is investigated. Both linear hexahedral finite elements and quadratic hexahedral finite elements are compared with the analytical solution. Figure 3.8 shows the radial displacement $U_r(r)$ (for $r = R_e$) and the relative error, for different mesh resolutions. The quadratic interpolation still shows a faster convergence, with a higher order of convergence regarding the relative error. But errors obtained for both linear and quadratic elements are very small, even for the coarsest mesh. Indeed, the relative error range

from 3.91% to 9.38 10^{-2}% for the linear interpolation, and from 2.34% to 7.33 10^{-5}% for the quadratic interpolation. It has been seen in section 3.3.1 that, when the mesh is not well refined, flexural deformation cannot be properly simulated using linear elements. In this case, it is demonstrated that when the deformation is purely extensional, the linear interpolation is sufficient and provides reasonable errors.

Fluid-structure interaction computation

An equivalent FSI problem can be solved by immersing the spherical capsule in a fluid computational domain (Fig. 3.9, left). The fluid box is extended from -4R to 4R in all the directions. The fluid mesh is composed of 2 101 165 tetrahedral elements, with a mesh resolution around the capsule of $h = 0.025$ m. The capsule is meshed using 1536 quadratic hexahedral elements, with an effective resolution of $H = 0.025$ m.

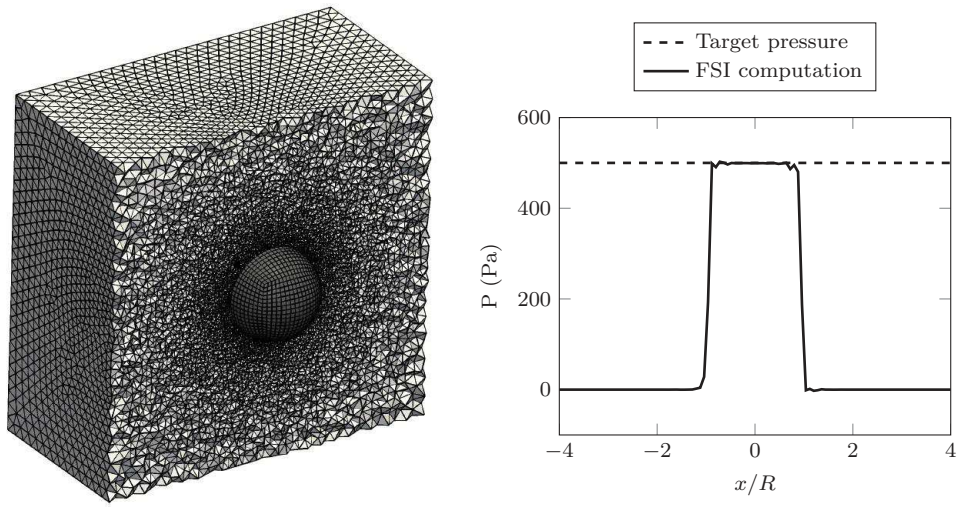

Figure 3.9: **Left:** Setup of the FSI computation, the capsule is immersed in a fluid box. **Right:** Pressure profile along the line $(-4R, 4R)$.

The capsule is thus surrounded by an outer fluid, and contains an inner fluid. Rather than applying a pressure on the capsule as for the structural problem, the capsule is inflated by imposing the analytical displacement on each solid node. This results in a pressurization of the inner fluid, and the inner pressure can then be compared to the target pressure applied in the structural computation ($P = 500$ Pa). Figure 3.9 (right) shows a pressure profile along a line which crosses the fluid computational domain. The pressure drop between the inner and the outer fluid is seen to be very close to the target pressure. Regarding the pressure at the center of the capsule, the relative error is 0.11%. The regularization process detailed in section 3.2.2 generates some oscillations near to the membrane location delimitating the inner and the outer fluids, but does not prevent to accuratly capture the pressure drop.

3.3.3 Capsule in a linear shear flow

In this test case, an initially spherical capsule of mean radius a is deposited in a linear shear flow, defined as $\vec{u} = ky\,\vec{e_x}$ (see Fig. 3.10, left). When deposited in the linear shear flow, the capsule begins to deform by changing orientation, and a steady deformation is finally reached (see Fig. 3.10, right).

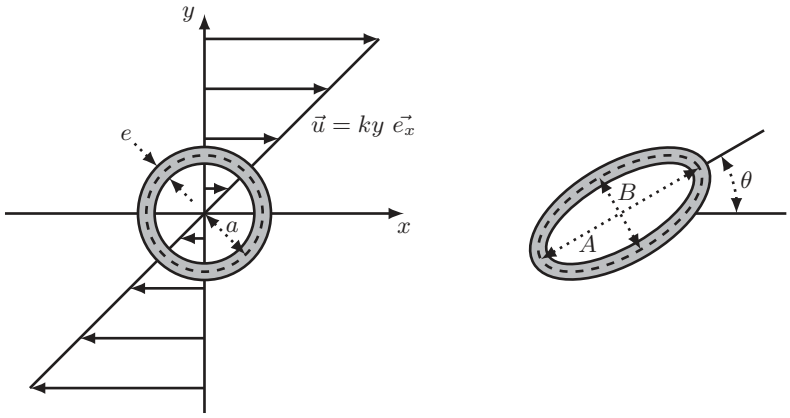

Figure 3.10: **Left:** The capsule is initially spherical, and deposited in a linear shear flow. **Right:** A steady deformation is reached, during which a tank-treading motion of the membrane is observed.

The orientation θ of the capsule, and the lengths A and B of the two principal axes of the ellipsoid of inertia in the shear plane can then be calculated. The deformation of the capsule in the shear plane is measured by the Taylor parameter:

$$D = \frac{A - B}{A + B}. \tag{3.41}$$

Capsule parameters	
Initial mean radius	a
Thickness	e
Shear modulus	G
Poisson coefficient	ν
Flow parameters	
Dynamic viscosity	μ
Density	ρ
Shear rate	k

Non-dimensional parameters	
Capillary number	$C_a = \dfrac{\mu k a}{eG}$
Reynolds number	$R_e = \dfrac{\rho k a^2}{\mu}$

Table 3.4: Definition of the capsule, flow, and non-dimensional parameters.

All the parameters relevant to the test case can be found in Tab. 3.4. The capsule-based Reynolds number R_e is chosen sufficiently low to satisfy the Stokes flow assumption, and the capillary number C_a which compares the viscous force to the membrane elastic force is successively set to 0.15; 0.3; 0.6. The membrane of the capsule is assumed to follow the Yeoh law (Eq. (3.11)), with $C_1 = G/2$ and

$C_2 = C_3 = 0$. A Poisson coefficient $\nu = 0.4995$ is chosen to insure that the membrane is quasi-incompressible. The ratio a/e between the initial mean radius of the capsule and the thickness of the membrane is chosen to be significantly high. A ratio $a/e = 1000$ is used, ensuring that the membrane is very thin compared to the size of the capsule, and making the bending resistance of the membrane almost negligible. All these conditions were selected to allow a proper comparison with the numerical results reported in Lac *et al.* (2004) [104].

The fluid domain is extended from -16a to 16a around the spherical capsule. The fluid mesh is composed of 1 924 682 tetrahedral elements with a mesh resolution at the center of the fluid box of $h = a/10$. In order to use the volume correction procedure (see section 3.2.6), the capsule is meshed using 2 906 linear prismatic elements, with an effective resolution of $H = a/10$. Figure 3.11 shows the evolution of the capsule deformation over the computation, for $C_a = 0.6$. The field displayed on the figure corresponds to the x-coordinate of the initial (reference) position of the membrane, introduced in section 3.2. From (a) to (e), the capsule deforms and reach constant deformation and orientation. From (f) to (j), the well known tank-treading behaviour of the membrane turning around the inner fluid is observed.

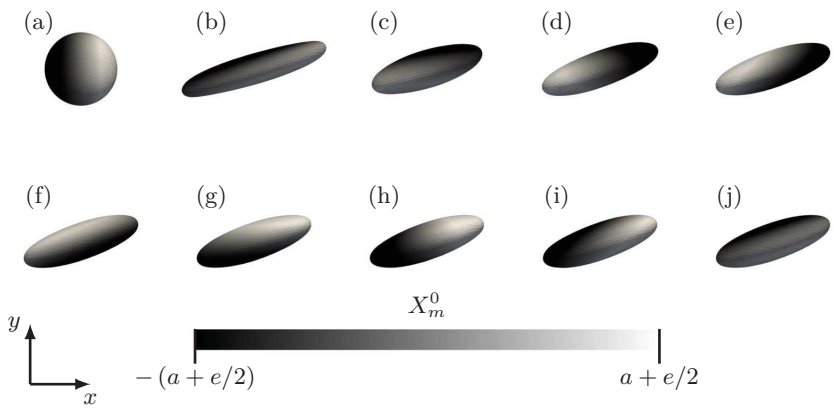

Figure 3.11: Visualisation of the capsule deformation over the computation. The x-coordinate of the initial position of the membrane nodes is displayed, enabling to visualize the tank-treading phenomenon.

The Taylor parameter D and the capsule orientation θ/π can be calculated from the steady deformation of the capsule. Figure 3.12 shows the evolution of both parameters as a function of the capillary number C_a. The present results are compared with the results of Lac *et al.* (2004) [104] where the membrane is considered to be infinitely thin and incompressible. A satisfactory comparison is obtained for both parameters. The relative error for the Taylor parameter D range from 0.18% to 1.03%, and from 0.64% to 6.08% for the capsule orientation θ/π. The maximal relative error is obtained when $C_a = 0.6$, and still increases when increasing the capillary number (not shown). This is probably due to the incompressibility of the membrane, which is not strictly insured in the present computations since using

a quasi-incompressible model. Indeed, volume variations are still allowed, and are seen to increase with the capillary number (not shown).

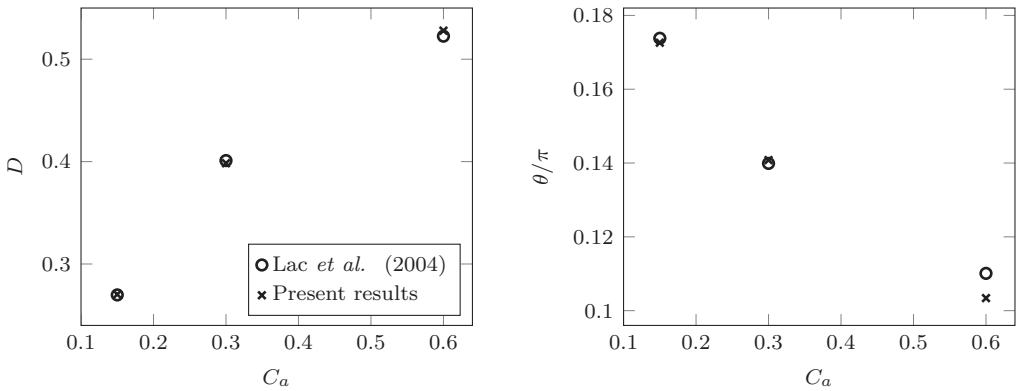

Figure 3.12: **Left:** Evolution of the Taylor parameter D as a function of the capillary number C_a. **Right:** Evolution of the capsule orientation θ/π. The present results are compared with the results of Lac *et al.* (2004) [104].

Influence of the volume correction procedure is shown in Tab. 3.5, considering the highest capillary number $C_a = 0.6$. A volume variation of 2.73% is observed when no volume correction is performed, whereas there is almost 0% volume variation when correcting the inner volume of the capsule. The influence of this volume correction procedure on the output parameters D and θ/π is however very small.

	Volume variation (%)	$\boldsymbol{D}$	$\boldsymbol{\theta/\pi}$
Volume correction	$\approx 10^{-4}$	0.5279	0.1034
No volume correction	2.73	0.5350	0.1019

Table 3.5: Influence of the volume correction on the outputs of the simulation for $C_a = 0.6$.

3.3.4 Red blood cell stretched by optical tweezers

The purpose is now to simulate the optical tweezers experiment, which consists in stretching a red blood cell (RBC) by using the optical trap principle [131]. An illustration of the experiment is given in Fig. 3.13. Two silica microbeads, each 4.12 μm in diameter, are attached to the cell at diametrically opposite points. The left bead is anchored to the surface of a glass slide while the right bead is trapped by a laser beam. The trapped bead remaining at rest, moving the slide and attached left bead stretches the cell. The experiment is simulated by applying a stretching force F to two opposite regions over the membrane in order to mimic the beads effect. For each imposed force F, the axial diameter D_A (in the direction of the stretching), and the transverse diameter D_T (orthogonal to the stretching direction) of the cell are measured (see Fig. 3.13, right) after the equilibrium has been reached (zero

velocity field over the whole computational domain).

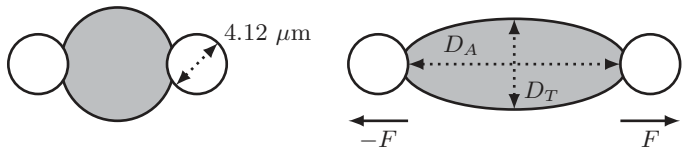

Figure 3.13: Illustration of the optical tweezers experiment. The effect of the beads is simulated by applying a stretching force to two opposite regions over the cell membrane, following the procedure of Mills *et al.* (2004) [131].

The average shape of a RBC has been determined by Evans [59], and is given by:

$$z = \pm 0.5 R_0 \left[1 - \frac{x^2 + y^2}{R_0^2} \right] \left[A + B \frac{x^2 + y^2}{R_0^2} + C \left(\frac{x^2 + y^2}{R_0^2} \right)^2 \right] \tag{3.42}$$

where $R_0 = 3.91$ μm is the average RBC radius, $A = 0.207161$, $B = 2.002558$, and $C = -1.122762$. The thickness of the RBC membrane is known to be few nanometers [113], and is here chosen to be $e = 4.0$ nm. As in the work of Mills *et al.* (2004) [131], the complex membrane of the RBC is modeled as a three-dimensional continuum, following the Yeoh law (Eq. (3.11)) with $C_1 = G/2$, $C_2 = 0$ and $C_3 = G/30$. The product between the membrane thickness e and the shear modulus G, also known as the in-plane shear modulus, is chosen to be $eG = 7.3\mu$N/m. As in the previous test case, a Poisson coefficient $\nu = 0.4995$ is chosen to insure that the membrane is quasi-incompressible.

The RBC is immersed in a fluid box extended from -3R_0 to 3R_0 in the direction of the stretching, from -2R_0 to 2R_0 in the direction orthogonal to the stretching, and from $-R_0$ to R_0 in the height of the cell. The fluid mesh is composed of 628 660 tetrahedral elements, with a constant mesh resolution of $h = R_0/12.5$. In order to use the volume correction procedure (see section 3.2.6), the RBC is meshed using 3 360 linear prismatic elements, with an effective resolution of $H = R_0/12.5$. The same procedure as the one used for the test case of section 3.3.1 is here used. As an external force, the force F is applied on the RBC membrane. The fluid thus starts moving, and the cell deforms. After a transient phase, the mechanical forces inside the membrane and the applied external force balance, and a steady deformation is obtained.

Figure 3.14 shows the deformation of the RBC for different values of the applied force F, which ranges from 0 to 193 pN. Each stretching force thus corresponds to one computation. Starting from the well known biconcave shape of the RBC, the cell is more and more elongated when increasing the force, and a large fold appears. Note that this kind of shape is also observed in the work of Mills *et al.* (2004) [131].

Figure 3.14: Visualisation of the red blood cell deformation over the entire range of stretching force. Only half of the cell is displayed.

Figure 3.15 shows the mechanical response of a RBC stretched by optical tweezers, as a function of the applied force. As the cell is more and more elongated when increasing the stretching force, it is seen that the axial diameter D_A increases. The elongation of the cell leads to its contraction in the orthogonal direction, resulting in a decreasing of the transverse diameter D_T. The present computation accurately captures experimental trends over the entire range of stretching force, and provides a good prediction of the diameters.

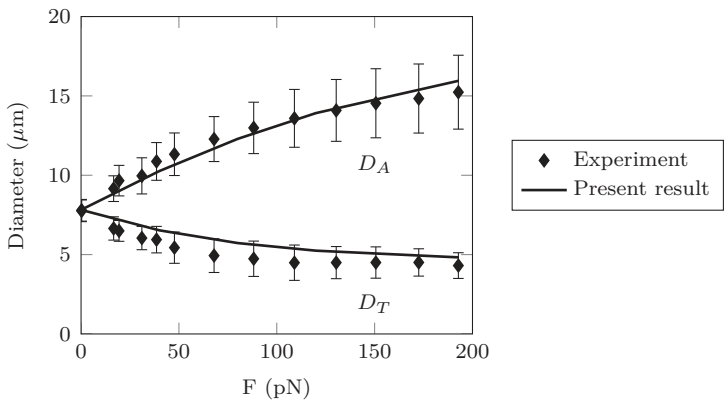

Figure 3.15: Axial (D_A) and transverse (D_T) diameters of the RBC stretched by optical tweezers. Comparison with the experimental data from Mills *et al.* (2004) [131].

As in section 3.3.3, the volume correction has only a small impact on the outcome of the simulation. For the maximum imposed force of 193 pN, there is no influence of this correction on the measured axial diameter D_A, whereas the transverse diameter D_T varies from 4.82 μm with correction (with $\approx 10^{-4}$ % volume variation) to 4.79 μm without correction (with 1.59% volume variation).

3.3.5 Flow-induced vibration of an elastic beam behind a cylinder

The last validation test case presented is the flow-induced vibration of an elastic beam behind a cylinder. This situation is more challenging than the former ones, since a periodic motion of the solid beam where inertia effects must be properly predicted is sought for. This test case was also selected because of the well-documented results obtained by numerous research groups which used different numerical methods for the FSI numerical resolution. These methods are summarized and briefly

described in Tab. 3.6. For more information, the reader is referred to the paper of Turek *et al.* (2010) [188]. The configuration of the problem, as introduced by Turek and Hron (2006) [187], is detailed in Fig. 3.16.

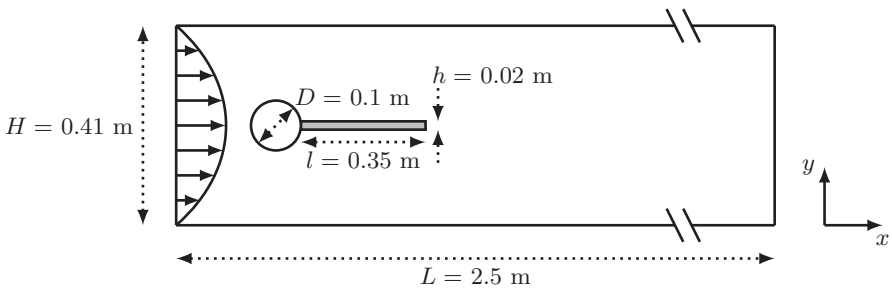

Figure 3.16: Details of the beam-cylinder configuration.

Method	**Description**
1 (Schäfer)	Implicit partitioned approach [166, 177] combining the finite-volume multigrid flow solver FASTEST and the finite-element structural solver FEAP, using an ALE formulation.
2a (Rannacher)	Monolithic variational formulation based on a unified Eulerian framework ("interface capturing").
2b (Rannacher)	Monolithic variational formulation based on the standard ALE approach ("interface fitting").
3 (Turek/Hron)	Fully implicit monolithic ALE-FEM approach.
4 (Breuer)	Partitioned approach combining the finite-volume scheme FASTEST-3D for the flow and the finite-element structural solver Carat, using an ALE formulation.
5 (Krafczyk/Rank)	Explicit partitioned approach which combines the Lattice-Boltzmann flow solver VirtualFluids (VF) and the structural p-FEM solver AdhoC.
6 (Wall)	A strongly coupled iterative staggered scheme [102, 193] based on an ALE formulation, Q2Q2 elements for the fluid and an EAS formulation for the structure.
7 (Bletzinger)	Partitioned approach based on a combination of three independent softwares: in-house codes CARAT++ and CoMA for structural shell analysis, coupling control and data transfer between non-matching grids, and the open source finite volume flow solver OpenFOAM.

Table 3.6: Summary of the different methods used in [188] to simulate the present test case.

The cylinder center is positioned at (0.2 m, 0.2 m) (measured from the left bottom corner of the channel). The right bottom corner of the elastic beam is positioned at (0.6 m, 0.19 m). Note that the setting is non-symmetric (the centerline of the

beam is at $y = 0.2$ m while the centerline of the channel is $y = 0.205$ m), preventing the extreme sensitivity of the results on the details of the flow computation. The problem is initially in 2D but is here extended to 3D by slightly extruding the 2D domain in the third direction, and imposing periodic boundary conditions on the upper and lower walls for both the fluid and the solid. A parabolic velocity profile is prescribed at the inlet of the channel:

$$v\left(0, y, z\right) = 1.5U \frac{y\left(H - y\right)}{\left(H/2\right)^2}, \tag{3.43}$$

where U is the bulk velocity. Two configurations were simulated, as referred to in [187, 188]: FSI1 and FSI3. The corresponding sets of parameters are gathered in Tab. 3.7. The elastic beam is modeled by a Saint-Venant law (Eq. (3.8)). The displacement of the beam extremity, initially positioned at (0.6 m, 0.2 m), is tracked during the computation for comparison with previous results.

	FSI1	**FSI3**
Flow parameters		
Density	$\rho = 1000$ kg/m^3	$\rho = 1000$ kg/m^3
Dynamic viscosity	$\mu = 1$ Pa.s	$\mu = 1$ Pa.s
Inlet velocity	$U = 0.2$ m/s	$U = 2$ m/s
Reynolds number	$\rho UD/\mu = 20$	$\rho UD/\mu = 200$
Beam parameters		
Density	$\rho_s = 1000$ kg/m^3	$\rho_s = 1000$ kg/m^3
Shear modulus	$G = 0.5$ MPa	$G = 2$ MPa
Poisson coefficient	$\nu = 0.4$	$\nu = 0.4$

Table 3.7: Parameters of the test case, two configurations are simulated: FSI1 and FSI3

	$\boldsymbol{M_1}$	$\boldsymbol{M_2}$	$\boldsymbol{M_3}$
Fluid			
Number of elements	160 707	971 069	6 582 336
Mesh resolution h	1.0 10^{-2} m	5.0 10^{-3} m	2.5 10^{-3} m
Solid			
Number of elements	72	560	4 480
Effective resolution H	1.0 10^{-2} m	5.0 10^{-3} m	2.5 10^{-3} m

Table 3.8: Characteristics of the fluid and solid meshes, three meshes are considered: M_1, M_2 and M_3.

For each configuration, three different meshes were tested as summarized in Tab. 3.8. For each of the meshes, the fluid mesh is tetrahedric, and the mesh of the beam is made of quadratic hexahedral elements. Concerning the fluid, the mesh resolution

is not constant over the whole fluid domain, the resolutions provided in Tab. 3.8 correspond to the mesh size around the elastic beam.

The FSI1 configuration is first simulated, leading to a stationary displacement of the elastic beam, consistent with [188]. Table 3.9 shows the two components of the displacement of the tracked point located at the extremity of the beam. The results obtained in [188] for different numerical methods are first displayed in the table. The present results are also displayed for the different meshes which have been tested in the study.

	$\boldsymbol{u_x}$ $[\times\mathbf{10^{-5}}]$ **(m)**	$\boldsymbol{u_y}$ $[\times\mathbf{10^{-4}}]$ **(m)**
2a	**2.4800**	**7.7800**
2b	2.2695	8.1556
3	2.2705	8.2088
5	**2.2160**	8.2010
6	2.2680	8.2310
7	2.2640	**8.2800**
M_1	2.8547	8.9378
M_2	2.6724	7.7917
M_3	2.5841	8.2243
M_∞	2.5012	8.4866
p	1.05	1.41
e_∞ (%)	3.32	3.09

Table 3.9: Results for the FSI1 configuration.

From the 3 levels of mesh M_1, M_2 and M_3 used to simulate the present test case, it is possible to calculate the apparent spatial order p of the method. Let dx_1, dx_2, dx_3 be the spatial resolutions of meshes M_1, M_2 and M_3, respectively (with $dx = h = H$ provided in Tab. 3.8), and $r = dx_1/dx_2 = dx_2/dx_3$ be the refinement factor, the apparent spatial order p is given by [26]:

$$p = \frac{1}{\ln(r)} \left| \ln \left| \frac{\phi_1 - \phi_2}{\phi_2 - \phi_3} \right| \right|, \tag{3.44}$$

where ϕ_k denotes the output variable of the simulation for the kth mesh. The extrapolated value ϕ_∞ can then be calculated as follows:

$$\phi_\infty = \frac{r^p \phi_3 - \phi_2}{r^p - 1} = \frac{r^p \phi_2 - \phi_1}{r^p - 1}. \tag{3.45}$$

The extrapolated relative error reads:

$$e_\infty = \left| \frac{\phi_\infty - \phi_3}{\phi_\infty} \right|. \tag{3.46}$$

The extrapolated values of the 2 components of the displacement of the beam extremity (corresponding to the infinitely refined mesh M_∞) as well as the corresponding apparent spatial order p and extrapolated relative error are also summarized in Tab. 3.9. Orders obtained from the output variables are greater than 1, which is satisfactory for an immersed boundary method. One can also note that extrapolated relative errors are small. For a better comparison, the whole results summarized in Tab. 3.9 are displayed in Fig. 3.17. A meaningful comparison between the reference results summarized in [188] and the present results is difficult to carry out for several reasons:

- In [188], the test case is 2D, and has been extended to 3D for the validation of the present method.

- Equivalent values of h and H for the simulations performed in [188] are not provided. Only the number of resolved unknowns is provided, and ranges from 11 250 (for method 2a) to 19 320 832 (for method 3), which is quite a wide range.

- It is difficult to determine if the results of the simulations performed in [188] are well converged for all the methods summarized, given the variability of the number of resolved unknowns.

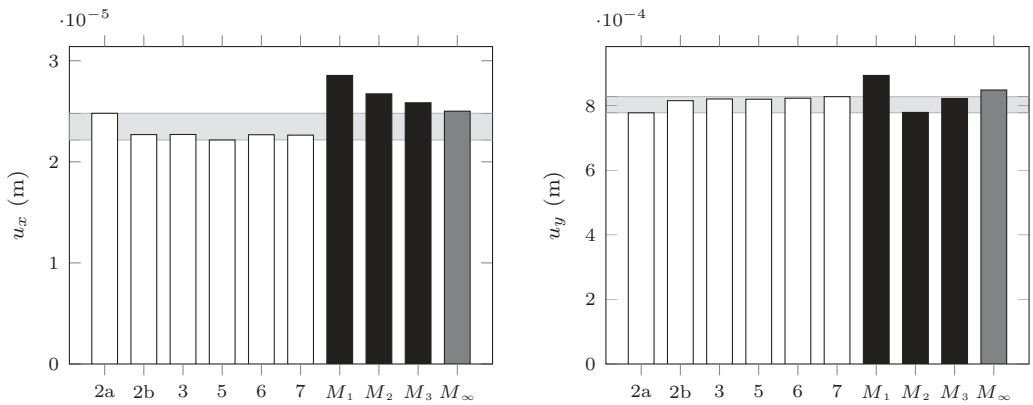

Figure 3.17: u_x and u_y components of the displacement of the beam extremity. The results obtained with the methods reported in [188] (displayed in white, and described in Tab. 3.6) can be compared with the present results, obtained for 3 different mesh resolutions (displayed in black). The extrapolated results are also provided (displayed in gray).

At least, one can say that the present method is able to retrieve a stationary displacement of the beam extremity which is in good agreement with values reported in [188]. Indeed, regarding extrapolated results displayed in Fig. 3.17, it is seen that the present results converge to the range of results reported in [188].

The set of parameters used for the FSI3 configuration leads to a periodic displacement of the beam extremity, as shown in Fig. 3.18. In this case, the mean displacement is provided in Tab. 3.10, with the amplitude of the oscillation. Two

frequencies can also be calculated from the oscillatory signal of u_x and u_y, respectively f_x and f_y. Again, spatial orders larger than unity are obtained for all the output variables. Extrapolated relative errors show that the present results are well converged with respect to the frequencies, almost converged with respect to the u_y displacement, but hardly converged with respect to the u_x displacement, which needs refinement to reach convergence. This may reflect the difficulty of the method to capture displacements tangent to the beam, coming from shear sollicitations.

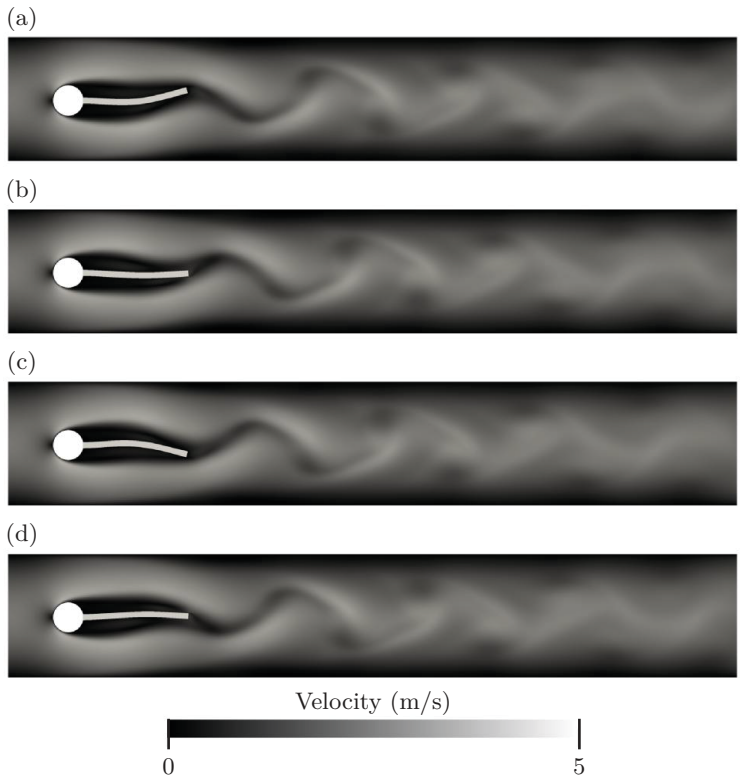

Figure 3.18: Visualisation of the flow-induced vibration of the elastic beam over one period of oscillation, for the FSI3 configuration. The velocity field around the beam is also displayed.

The results of Tab. 3.10 are also displayed in Fig. 3.19, for a better comparison. The variability of the results reported in [188] shows the extreme sensitivity of the present configuration. This time, the number of resolved unknowns reported in [188] ranges from 11 250 (for method 2a) to 2 480 814 (for method 5). The 3 meshes provide similar frequencies of oscillation, which are in good agreement with the results reported in [188]. However, regarding mean values and amplitudes of the displacement, it is seen that only meshes M_2 and M_3 provide a satisfactory comparison with the results reported in [188]. One can note that the extrapolated results are very close to the results obtained with method 5, which is the one resolving the most of unknowns.

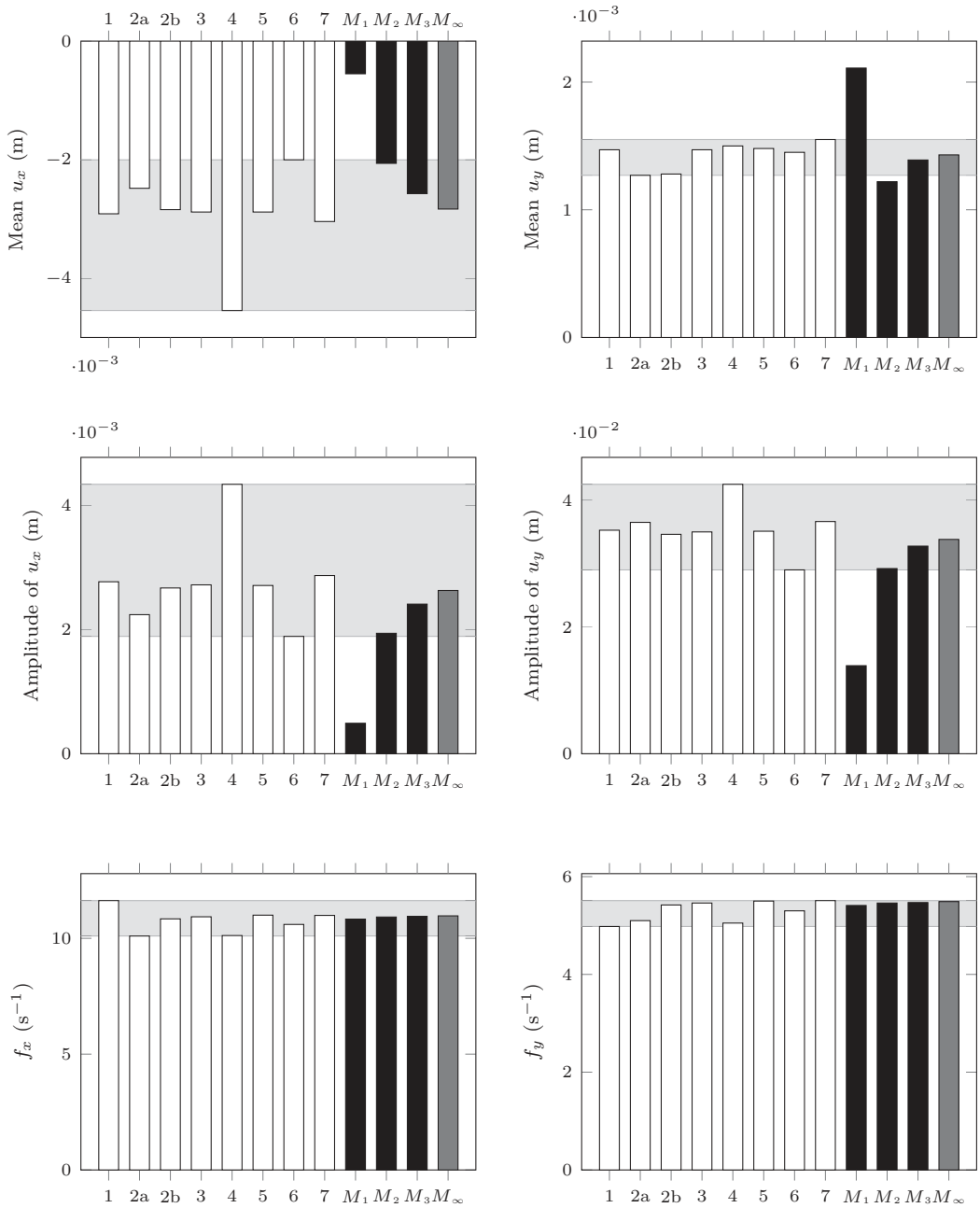

Figure 3.19: Results obtained for the FSI3 configuration. The first line shows the two components of the mean displacement, the second line the corresponding amplitudes, and the frequencies are displayed in the third line. The results obtained with the methods reported in [188] (displayed in white, and described in Tab. 3.6) can be compared with the present results, obtained for 3 different mesh resolutions (displayed in black). The extrapolated results are also provided (displayed in gray).

	u_x $[\times 10^{-3}]$ (m)	u_y $[\times 10^{-3}]$ (m)	f_x (s^{-1})	f_y (s^{-1})
1	-2.91 ± 2.77	1.47 ± 35.26	**11.63**	**4.98**
2a	-2.48 ± 2.24	**1.27** ± 36.50	**10.10**	5.10
2b	-2.84 ± 2.67	1.28 ± 34.61	10.84	5.42
3	-2.88 ± 2.72	1.47 ± 34.99	10.93	5.46
4	**-4.54** ± **4.34**	1.50 ± **42.50**	10.12	5.05
5	-2.88 ± 2.71	1.48 ± 35.10	11.00	5.50
6	**-2.00** ± **1.89**	1.45 ± **29.00**	10.60	5.30
7	-3.04 ± 2.87	**1.55** ± 36.63	10.99	**5.51**
M_1	-0.55 ± 0.49	2.11 ± 13.89	10.83	5.41
M_2	-2.06 ± 1.94	1.22 ± 29.21	10.92	5.46
M_3	-2.57 ± 2.41	1.39 ± 32.75	10.95	5.47
M_∞	-2.83 ± 2.63	1.43 ± 33.81	10.97	5.49
p	1.57 1.62	2.39 2.11	1.58	1.34
e_∞ (%)	9.18 8.59	2.78 3.15	0.14	0.20

Table 3.10: Results for the FSI3 configuration.

The same procedure as the one described in Eq. (3.44) can be used to determine the apparent temporal order of the method, considering 3 different time steps dt_1, dt_2 and dt_3 for the simulation, and using the mesh M_2. The beam displacements obtained for these 3 time steps are summarized in Tab. 3.11 with the corresponding extrapolated values, apparent orders and extrapolated relative errors. The apparent temporal orders obtained are around $p = 1$, and extrapolated relative errors are below 1%.

	u_x $[\times 10^{-3}]$ (m)	u_y $[\times 10^{-3}]$ (m)
$dt_1 = 5.00\ 10^{-5}$ s	-2.0489 ± 1.9274	1.1925 ± 29.1467
$dt_2 = 2.50\ 10^{-5}$ s	-2.0403 ± 1.9191	1.1843 ± 29.0895
$dt_3 = 1.25\ 10^{-5}$ s	-2.0363 ± 1.9150	1.1868 ± 29.0565
dt_∞	-2.0326 ± 1.9110	1.1878 ± 29.0109
p	1.07 1.00	1.74 0.79
e_∞ (%)	0.18 0.21	0.09 0.16

Table 3.11: Determination of the apparent temporal order.

3.4 Application: flow through an aortic valve

In this section, an application of the method is presented to illustrate its potential. The chosen application is the flow throught an aortic valve, which has been widely investigated in a number of works [21, 43, 44, 45, 91, 92, 96]. Figure 3.20 (left) shows the meshed fluid geometry used for the computation, corresponding to an idealized geometry of the aorta. The diameter of the aorta is chosen to be $D = 2$ cm. The fluid mesh is composed of 752 460 tetrahedral elements, with a constant mesh resolution of $h = 0.5$ mm. The geometry of the aortic valve is composed of three leaflets, and has been constructed to fit the arotic root, as displayed in Fig. 3.20 (right). The whole aortic valve is meshed using 450 quadratic hexahedral elements, with an effective resolution of $H = 0.5$ mm.

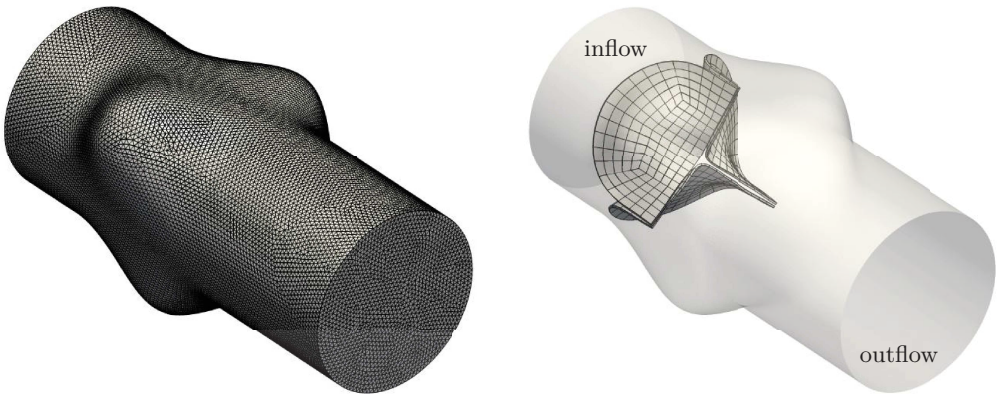

Figure 3.20: **Left:** Meshed geometry of the idealized aorta. **Right:** Meshed geometry of the model of aortic valve positioned inside the aorta.

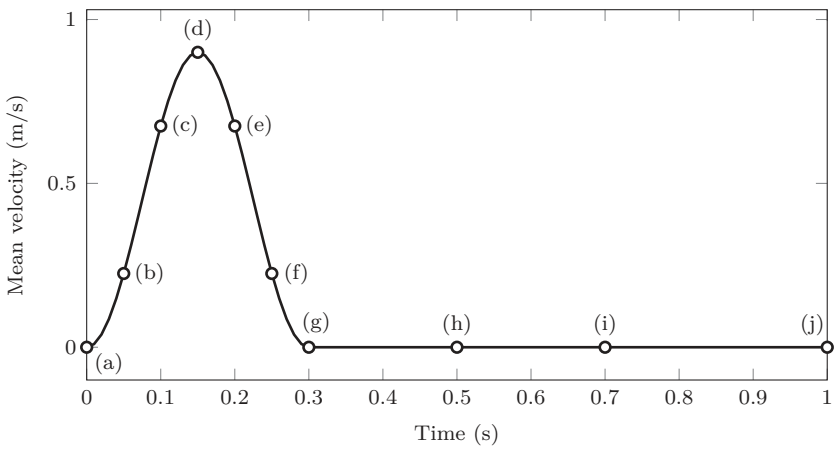

Figure 3.21: Mean velocity prescribed as inflow. The signal corresponds to one cycle for $F_I = 0.3$. Snapshots at instants (a) to (j) are displayed in Fig. 3.22-3.23.

The mean velocity prescribed as inflow is given, for $0 < t < T = \dfrac{60}{n_{bpm}}$:

$$U_{mean}(t) = \begin{cases} \dfrac{1}{2}\dfrac{\mu Re}{\rho D}\left[1 + \sin\left(\dfrac{2\pi}{F_I T}\left(t - \dfrac{F_I T}{4}\right)\right)\right] & \text{if } t \leq F_I T \\ 0 & \text{if } t > F_I T \end{cases} \tag{3.47}$$

where n_{bpm} stands for the number of beats per minutes and F_I is a parameter which allows to set the duration of the injection phase. Figure 3.21 shows the time evolution of the mean velocity $U_{mean}(t)$. The inlet velocity profile is chosen to be parabolic, even if this assumption is not suitable given the relatively high value of the Womersley number (greater than 10). The parameters of the present study are summarized in Tab. 3.12, and are inspired from the work of De Hart *et al.* [44]. The leaflets of the valve are modeled by a Neo-Hookean law. The flow solver represents the turbulent flow by Large Eddy Simulation and the Sigma model [142] is used to model the effect of the scales which are too small to be properly discretized by the fluid mesh.

Flow parameters	
Density	$\rho = 1000$ kg/m^3
Dynamic viscosity	$\mu = 4.0\ 10^{-3}$ Pa.s
Reynolds number	$Re = 4500$
Number of beats per minute	$n_{bpm} = 60$
Fraction of injection	$F_I = 0.3$
Valve parameters	
Shear modulus	$G = 3.0\ 10^4$ Pa
Poisson coefficient	$\nu = 0$
Thickness of the leaflets	$e = 0.2$ mm

Table 3.12: Parameters of the flow and the valve leaflets.

Four cycles were simulated, and different snapshots of the valve deformation over the fourth cycle are displayed in Fig. 3.22. Labels from (a) to (j) correspond to the ones displayed in Fig. 3.21. From (a) to (d), the inlet mean velocity is increasing, resulting in the opening of the valve. Regarding snapshot (b) in Fig. 3.22-3.23, it is seen that the valve inflates while the opening deformation initiates at the middle of the valve and then spreads toward the extremities. This observation is consistent with the work of Hsu *et al.* [92], where the same opening behavior was observed. From (d) to (g), the inlet velocity is decreasing, and the valve is gradually closing with a strong flapping of the leaflets. At the end of this phase, the inlet velocity is zero, but one leaflet remains open. Then, the leaflet is gradually closing from (g) to (j), and the valve is finally closed at the end of the cycle. One can notice that for the four cycles simulated, this phenomenon does not appear every time, or when appearing it is not always on the same leaflet (not shown). These cycle-to-cycle variations were expected, given the value of the Reynolds number.

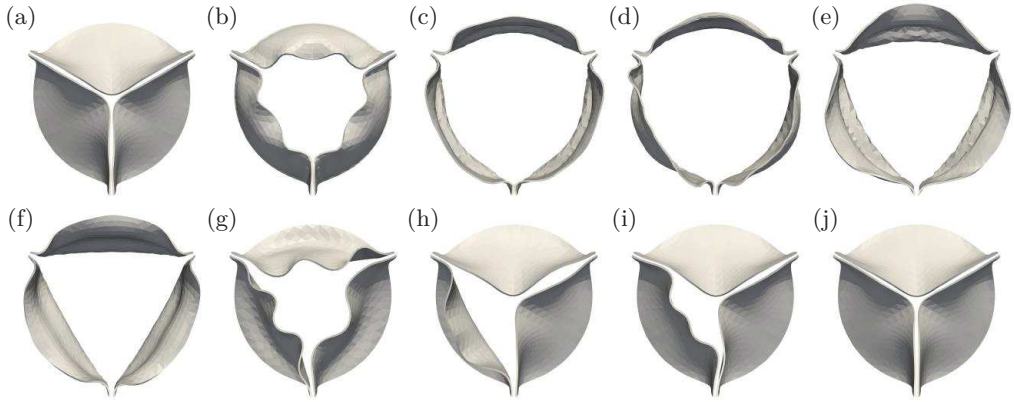

Figure 3.22: Snapshots of the valve deformation over the fourth cycle.

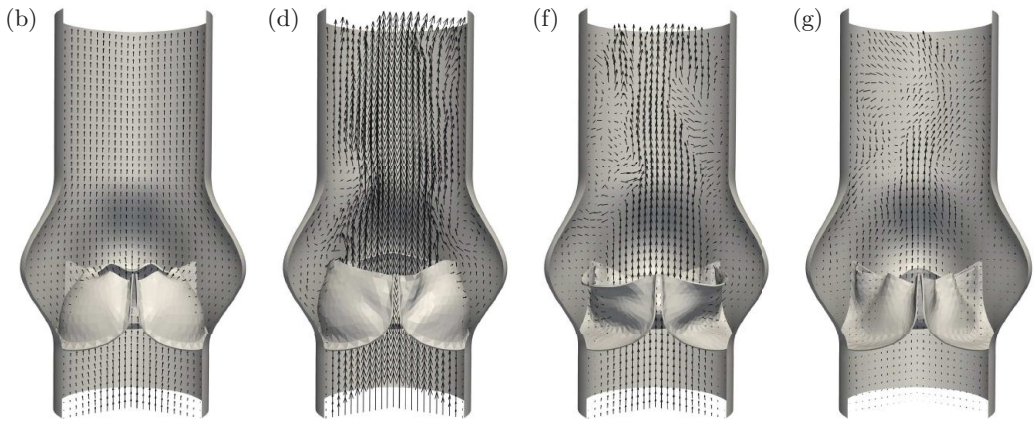

Figure 3.23: Snapshots of the instantaneous velocity vectors over the fourth cycle. Only four snapshots out of the ten displayed in Fig. 3.22 are shown.

Figure 3.23 shows four snapshots of the instantaneous velocity vectors over the fourth cycle. The flapping of the leaflets generates numerous of vortices downstream of the valve, reflecting the presence of flow instabilities, also observed in [21, 44, 92]. Further flow analysis could be conducted, but is out of the scope of this work. Still, the present simulation has proven the robustness of the ITBM, which leads to a realistic description of a very complex flow at high Reynolds number and non-trivial deformation of the membrane.

3.5 Conclusion

A numerical method for simulating the fluid-structure interaction problem in the case of highly deformable membranes has been presented. The approach is based on the immersed boundary method adapted to unstructured grids with the reproducing kernel particle method. The specificity of the approach is that the membrane constituting the immersed boundary is in fact a thick boundary, modeled as a 3D continuum. This enables to use a classical finite-element formulation to solve the membrane mechanics.

The computing accuracy of the method has been demonstrated by a number of test cases where the results provided by the present numerical tool were confronted to either previous numerical, analytical or experimental data. The test cases of section 3.3 showed that both closed and open membranes can be properly simulated with the ITBM. Simulating very thin membranes having a thickness much smaller than the fluid mesh resolution was expected to lead to problematic issues, especially regarding the procedures of regularization/convection (described in sections 3.2.2 and 3.2.4, respectively). The test cases of sections 3.3.3 and 3.3.4 however showed that this is actually well managed by the present method.

The ITBM was then used to simulate the flow through a tri-leaflet aortic valve, at a significantly high Reynolds number. The highly complex valve deformation and flow instabilities observed in this study demonstrated the strong robustness of the method, which however needs to be further validated on such a highly complex FSI problem.

Chapter 4

Application to aortic valve computation

Chapter contents

4.1 Introduction 82
4.2 Materials and Methods 83
4.2.1 Numerical method 83
4.2.2 Experimental setup 85
4.2.3 Computational setup 88
4.3 Results 89
4.3.1 Valve dynamics 89
4.3.2 Leaflets stress distribution 92
4.3.3 Flow dynamics 93
4.4 Discussion 97
4.5 Supplementary material 98
4.5.1 Overall PIV-vs-CFD comparison 98
4.5.2 Transvalvular pressure gradient 104

Preliminary remarks

This chapter corresponds to an article entitled "A combined experimental and numerical study of a polymeric aortic valve model" [171] which has been submitted in *Cardiovascular Engineering and Technology*, and aims at investigating, both experimentally and numerically, the complex FSI problem involved when the blood flows through the aortic valve. This FSI problem is first investigated experimentally, establishing an experimental configuration of a polymeric model of aortic valve under pulsatile flow conditions. This experimental configuration is then simulated using the YALES2BIO solver, and especially the immersed thick boundary method (ITBM) previously introduced in chapter 3. A short reminder of the numerical method is thus provided in section 4.2.1. This combined experimental and numerical study first

constitutes an excellent experimental validation, showing the ability of the ITBM to handle FSI simulations of the blood flow through the aortic valve. It also attempts to provide useful information that should be considered for future designs of flexible artificial aortic valves.

4.1 Introduction

The aortic heart valve separates the left ventricle from the aorta. It is composed of three thin deformable leaflets that open and close passively during the cardiac cycle, preventing blood from flowing back into the left ventricle, and thus ensuring an unidirectional blood flow through the cardiovascular system. Aortic valves may degenerate and lead to either insufficiency or stenosis, which can cause the death of the patient if not treated. Usually, medication is not a sufficient treatment option, and the diseased aortic valve needs to be replaced by a prosthesis.

The two types of prostheses mainly used are mechanical heart valves (MHV) and bio-prosthetic heart valves (BHV). MHVs are known for their durability but often lead to thrombosis (blood coagulation) complications [95]. Composed of three deformable leaflets, BHVs are closer to the natural aortic valve, providing better hemodynamic properties. They are however not as durable as MHVs and need to undergo an additional surgery after 10 to 15 years [208].

Over the last decades, a significant research effort has been carried out for the development of artificial aortic valves, particularly BHVs [137, 138]. A key milestone in the BHV development process is the understanding of the behavior and mechanics of the valve, and its complex fluid-structure interaction (FSI) with the blood flow. To this end, the leaflets kinematics and the fluid flow can be experimentally investigated on idealized in-vitro configurations, using either particle image velocimetry (PIV) [136] or laser Doppler velocimetry (LDV) [205]. On the other side, numerical simulation constitutes a powerful tool which provides a full access to all the details of the flow and physical quantities of interest, such as the stresses undergone by the leaflets. As a result, important research efforts have been made on the FSI modeling of native and prosthetic aortic valves, either by developing dedicated FSI models [21, 43, 44, 82, 83, 91, 92, 96] or by using commercial FSI software packages [159, 184, 199, 200].

Numerical approaches are however no substitute for experimental investigations, but should rather be considered to be a valuable supplement when aiming at understanding such highly complex physical phenomena. Moreover, FSI modeling needs to be supported by experimental data in order to establish the validity and reliability of the numerical results. As pointed out by Kheradvar *et al.* [98], experimental validations of FSI valve models mainly consider mechanical valves [3, 29, 75, 76, 87] rather than flexible native or bioprosthetic valves, and generally focus on the opening and forward-flow phases without considering the valve closure. Two main limitations are highlighted by Kheradvar *et al.* [98]: the ability of FSI valve models to perform

multiple cardiac cycles, and the difficulty to simulate the contact between the thin deformable leaflets when the valve is fully closed.

The present work aims at establishing one of the foremost combined experimental and numerical study existing to date about the dynamics of flexible aortic valves. A physiological and well-controlled experimental in-vitro configuration of an aortic valve under pulsatile flow conditions is set up and numerically simulated using the FSI model previously developed by Sigüenza *et al.* [168]. High-speed recording of the valve movement as well as PIV measurements are performed together to investigate, both experimentally and numerically, the leaflet kinematics and the flow dynamics. The opening and closure dynamics of the valve are carefully investigated, and the flow is analyzed over multiple cardiac cycles (24 cycles) to characterize the turbulence downstream of the valve.

4.2 Materials and Methods

4.2.1 Numerical method

The Fluid-Structure Interaction model used in the present study is based on the immersed thick boundary method (ITBM), which is presented and extensively validated in [168]. The ITBM was adapted from the original immersed boundary method (IBM) introduced by Peskin [152] to deal with 3D membranes having a finite thickness. The computational domain is decomposed into the solid part (i.e. the valve) and the fluid part, which are both discretized with independent meshes. The mechanics of the valve is solved on a Lagrangian mesh allowed to move with the deformation, whereas the fluid motion is solved on a fixed Eulerian unstructured mesh. The different steps of the ITBM are the following:

(1) The mechanical force $\overrightarrow{F}$ resulting from the valve deformation is calculated on the Lagrangian mesh.

(2) The volumetric force $\overrightarrow{f}$, which represents the force exerted by the valve on the fluid, is calculated by regularizing the mechanical force $\overrightarrow{F}$ on the Eulerian mesh, such as

$$\overrightarrow{f}\left(\overrightarrow{x},t\right)=\int_{\Omega_s}\overrightarrow{F}\left(\overrightarrow{X},t\right)\delta\left(\overrightarrow{x}-\overrightarrow{X}\right)dX,$$

where $\overrightarrow{x}$ and $\overrightarrow{X}$ respectively denote the coordinates vectors of the Eulerian nodes and Lagrangian nodes, Ω_s denotes the solid domain defining the valve, and δ is the well known Dirac function.

(3) The Navier-Stokes equations (forced by the regularized mechanical forces) are solved on the Eulerian mesh, yielding the velocity of the fluid $\overrightarrow{v}$.

(4) The velocity of the valve $\overrightarrow{V}$ is calculated by interpolating the fluid velocity $\overrightarrow{v}$ on the Lagrangian mesh, such as

$$\overrightarrow{V}\left(\overrightarrow{X},t\right)=\int_{\Omega_f}\overrightarrow{v}\left(\overrightarrow{x},t\right)\delta\left(\overrightarrow{x}-\overrightarrow{X}\right)dx,$$

where Ω_f denotes the fluid domain.

The Dirac function δ used in the procedures of regularization and interpolation of steps (2) and (4) is numerically represented by a smooth dicrete Dirac function, which is adapted to unstructured meshes using the Reproducing Kernel Particle Method (RKPM) [128, 153, 168]. Imposing the exact impermeability of the valve leaflets treated through the IBM framework is challenging. Indeed, interpolation procedures induce small leakage of the flow through the leaflets. Moreover, there is no particular treatment performed to solve the contact between the flexible leaflets during the valve closure. The present ITBM intrinsically prevents any penetration of the leaflets, the minimum gap between the leaflets depending on the size of the discrete Dirac function, which is typically chosen as being 4 times the fluid mesh resolution h.

The computation of the mechanical force $\overrightarrow{F}$ is performed by the in-house LMGC90 solid mechanics solver [157], using the classical finite-element method. In the present work, a quasi-incompressible Neo-Hookean material is used to model the valve, defined by its strain energy function:

$$W = \frac{G}{2}\left(\bar{I}_1 - 3\right) + \frac{K}{2}\left(\ln J\right)^2, \tag{4.1}$$

where G and K are the shear modulus and the bulk modulus, respectively. $\bar{I}_1$ is the first invariant of the isochoric Right Cauchy-Green deformation tensor $\bar{\mathbb{C}}$, and J is the Jacobian of the transformation. Provided that fluid and solid densities are of the same order of magnitude, and that the thickness of the valve is small enough, the inertia of the valve can be neglected.

The YALES2BIO flow solver is used solving the forced Navier-Stokes equations over the Eulerian unstructured mesh by using a projection method [37]. The momentum conservation equations reads:

$$\frac{\partial \overrightarrow{v}}{\partial t} + \overrightarrow{\nabla}.\left(\overrightarrow{v} \otimes \overrightarrow{v}\right) = -\frac{\overrightarrow{\nabla} p}{\rho} + \nu \Delta \overrightarrow{v} + \frac{\overrightarrow{f}}{\rho}, \tag{4.2}$$

where $\overrightarrow{v}$ and p are the velocity vector and pressure, ρ the density and ν the kinematic viscosity. For an incompressible flow, the mass conservation equation becomes:

$$\overrightarrow{\nabla}.\overrightarrow{v} = 0. \tag{4.3}$$

The fluid velocity is advanced using a 4th-order centred scheme in space and a 4th-order Runge-Kutta scheme in time. A divergence-free velocity field is obtained at the end of the time-step by solving a Poisson equation for pressure and correcting the predicted velocity. A Deflated Preconditioned Conjugate Gradient algorithm is used to solve this Poisson equation. More details about the employed numerical methods can be found in [34, 123, 140]. The flow solver represents the turbulent flow by Large Eddy Simulation and the Sigma model [14, 142] is used to model the effect of the scales which are too small to be properly discretized by the fluid mesh.

The present fluid solver was validated on the benchmark of idealized cardiovascular device proposed by the U.S. Food and Drug Administration (FDA) [215], as well as on a variety of test cases [124, 128].

4.2.2 Experimental setup

A self-made heart valve prosthesis with a rigid frame made with PEEK material and leaflets manufactured as thin polyurethane foil is used. The cylindrical shaped leaflet is heat treated and mechanically closed, enabling to obtain an almost closed design of the valve (see Fig. 4.1 (a)). This prosthesis is placed inside an aortic anatomy, cast inside a rigid silicone model. The aortic anatomy is based on physiological data, including the three sinuses of Valsalva after the calculations by Reul *et al.* [160]. The aortic root diameter is 25 mm, chosen equal to the outer diameter of the prosthesis. The ascending aorta is designed with a diameter of 31 mm.

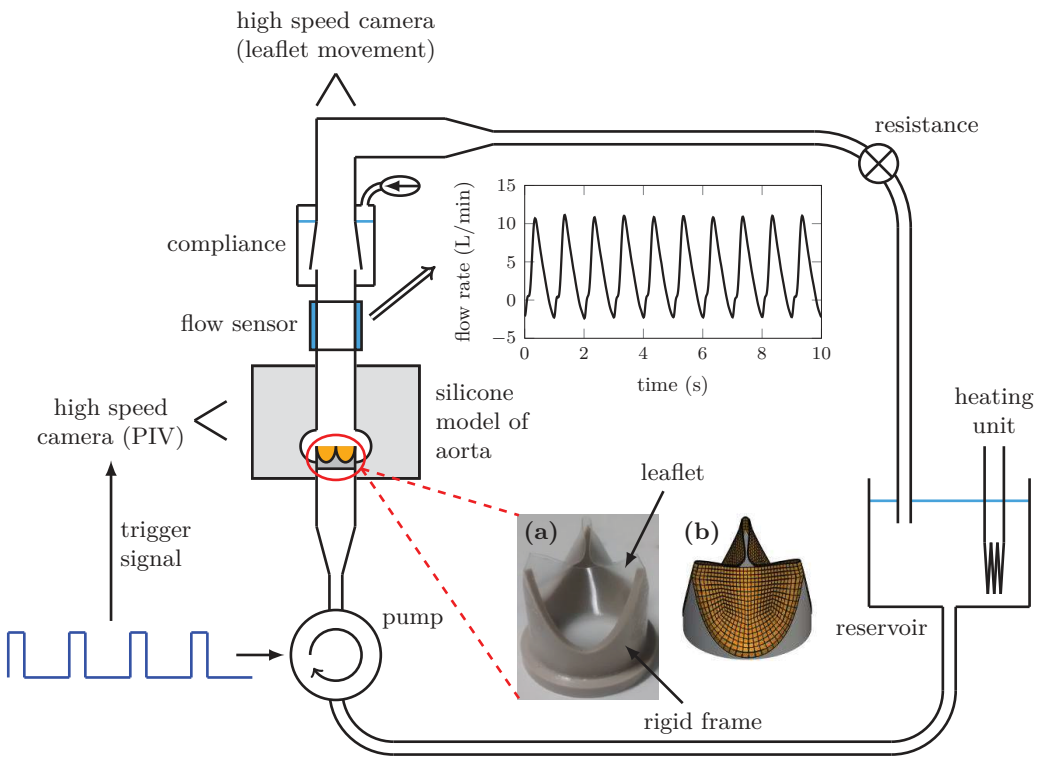

Figure 4.1: In-vitro pulse duplicator designed to reproduce physiological flow conditions.

The silicone model with the inserted prosthesis is connected to a pulse duplicator which consists of a rotatory pump (dp3, Medos Medizintechnik AG, Stolberg, Germany), an adjustable compliance and resistance, tubing and a reservoir with a heating unit. A sketch is shown in Fig. 4.1. Data acquisition and controlling of the pulse duplicator is achieved by in-house written programs (LabVIEW, Austin, TX, USA). The rotatory pump is controlled by a program which delivers a square-wave signal, leading to an oscillatory rotation of the pump which enables to generate a

pulsatile flow allowing fully opening and closure of the valve. As shown in Fig. 4.1, the flow measured by an ultrasonic flow meter downstream of the aortic valve is quasi-periodic with reduced cycle-to-cycle variations (less than 5% of variations). One typical cycle is displayed in Fig. 4.2 (a). The experimental flow rate curve is characteristic from the physiological flow rate observed in the aorta, with a first flow pulse corresponding to systole, followed by a reversed flow rate, corresponding to diastole. Compared to a physiological signal, the present signal has a short diastole, the study focusing on the opening and closure of the valve.

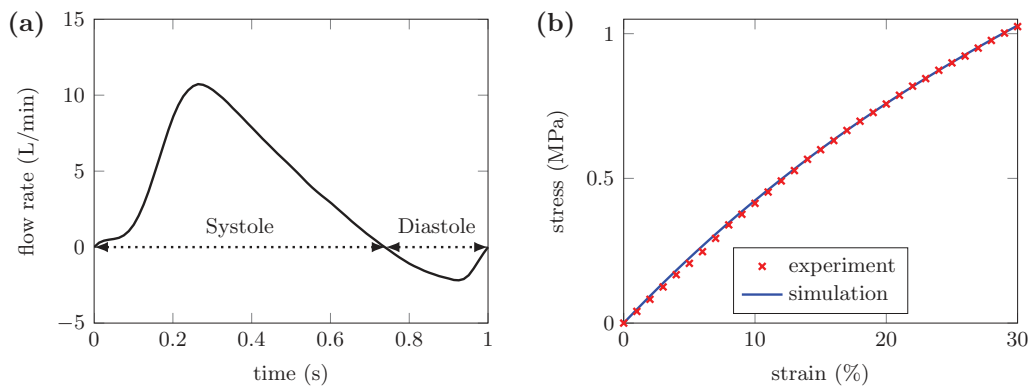

Figure 4.2: **(a)** One typical cycle of the flow rate signal measured during the experiment, used as inlet boundary condition of the simulation. **(b)** Stress-strain relationship extracted from the uniaxial tensile test. The material parameters G and K are determinated by fitting the simulation with the experiment.

As blood analogue fluid, a transparent solution of 56.4% glycerol and 43.6% water by mass is used inside the flow circuit as working fluid. At 45°C, it matches the refractive index of the silicone model to eliminate optical distortions and it possesses a viscosity of 3.6 mPa.s. Both the flow and the valve can be characterized by a set of parameters summarized in Tab. 4.1.

In view of the Reynolds number R_e and Womersley number W_0 of the flow, the blood flow can be assumed to be Newtonian, so that the blood analogue fluid is of constant viscosity, corresponding to the high-shear limit values [161]. Determination of the material parameters of the leaflet is carried out by means of experimental tensile tests and parameter identification using the LMGC90 solid mechanics solver. First, an uniaxial tensile test is performed on a stick of polyurethane, giving the stress-strain relationship of the material (see Fig. 4.2 (b)). Then, the experimental tensile test is simulated with the LMGC90 solid mechanics solver. A dedicated algorithm enables to determine the material parameters which provide the best fit between the experiment and the simulation, as shown in Fig. 4.2 (b). The quasi-incompressible Neo-Hookean strain energy function introduced in Eq. (4.1) enables a very good representation of the material mechanical behaviour over the range of 0-30% deformation.

Flow parameters	
Density	$\rho = 1100$ kg/m^3
Dynamic viscosity	$\mu = 3.6\ 10^{-3}$ Pa.s
Heart rate	$n_{bpm} = 60$
Mean cardiac output	$Q_{mean} = 3.48$ L/min
Reynolds number	$Re = 1388$
Womersley number	$W_0 = 17$
Valve parameters	
Density	$\rho_s = 1000$ kg/m^3
Shear modulus	$G = 2.4$ MPa
Bulk modulus	$K = 1.6$ MPa
Thickness of the frame	$e_f = 1.45$ mm
Thickness of the leaflet	$e = 0.15$ mm
Radius of the leaflet	$R = 12.5$ mm

Table 4.1: Flow and valve parameters.

The movement of the valve leaflets is recorded from the top of the valve by a high-speed camera (CMOS, 1280x1024, 10 bit). Furthermore, two-dimensional PIV measurements are performed to determine the experimental flow field in the centerplane (through the commissure of the prosthesis) of the aortic geometry behind the prosthesis. A two-cavity Nd:Ylf laser (Pegasus, New Wave Research Inc.) operated as light source. The laser light beam is expanded into a thin light sheet of approximately 1 mm thickness by an arrangement of lenses. The laser light illuminates the tracer particles (diameter of 10.5 μm, Intelligent Laser Applications, Jülich, Germany), seeded into the circuit and carried by the fluid, twice within a defined time interval Δt to obtain pair images. A Nanosense MKIII 1280x1024 CMOS High-Speed camera (IDT, Redlake) with a 105 mm Nikon Makro Nikkor 105mm F2.8D lens recorded the particle images. The camera was positioned at an angle of 90° to the illuminated laser light plane.

For data acquisition and PIV post-processing, the software Dynamic Studio 2.3 (Dantec Dynamics A/S, Skovlunde, Denmark) is used. 24 cycles were recorded with a time interval Δt between the image pairs of 950 μs to obtain an optimal pixel displacement for further analysis. The data acquisition of the particle images is set to 100 Hz, i.e. 100 pair images are recorded per cycle. As calibration method, a target with a mm scale which is aligned in the centerplane, is recorded. With knowledge of the displacement of the particles and the time delay between the image pairs, the velocity can be calculated. For the evaluation, the recorded pair images are divided into small subareas called interrogation areas. By means of statistical methods, i.e., adaptive correlation, the local velocity vectors for the pair images is determined. The final interrogation area size is 32x32 pixels with an overlap of 50%. The resolution of the resulting vector field is 0.0425x0.0425 mm^2/px^2. The resulting mesh of the PIV data is 63x79 points (radial/axial).

4.2.3 Computational setup

From the computational point of view, the geometry of interest is separated into the solid and the fluid domains. The solid domain is composed of the polyurethane leaflet whose geometry after manufacturing is cylindrical of radius R and thickness e. After performing the heat treatment on the valve, the geometry of the leaflet is closed. To reproduce this heat treatment in the numerical simulation, several preprocessing steps are performed. First a CAD model of the open leaflet before heat treatment is designed. The initially cylindrical geometry of the leaflet is constructed by introducing a shrinkage parameter r, mimicking a possible shrinkage of the leaflet resulting from the heat treatment. The bottom of the leaflet is circular and fits the tri-commissure frame. Then, going from the bottom to the top, the leaflet is shrinked by using a small offset r to define the apex (see Fig. 4.3 (a), (b)). The higher is the value of r, the more important is the shrinkage. A zero value of r corresponds to no shrinkage of the leaflet. In this study, a value of $r = 2$ mm is considered. Then a structural computation performed with the LMGC90 solver enables to close the leaflet by imposing a normal pressure onto the outer surface of the leaflet, thus mimicking the mechanical closure performed in the experiment (see Figs. 4.1 (b) and 4.3 (c)). The obtained geometry is then used as the initial and unconstrained leaflet geometry for the FSI computation.

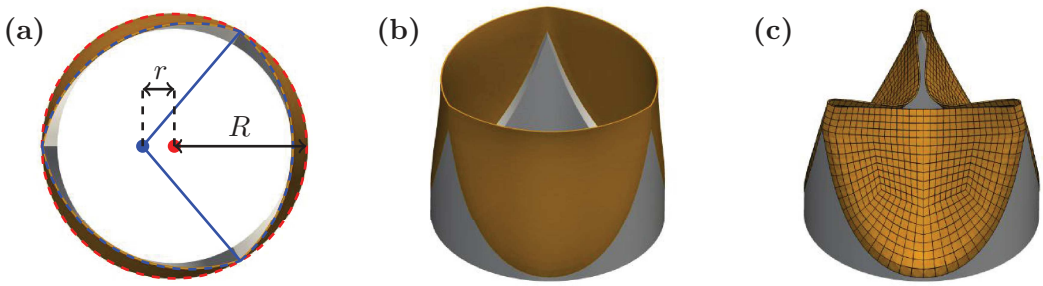

Figure 4.3: Procedure used to generate the geometry of the leaflet obtained after heat treatment. An almost cylindrical leaflet is first designed, and then closed by performing a structural computation.

Both the aortic and the frame geometry are given by the CAD models of the experimental setup, and are used to design the geometry of the fluid domain. The silicone aorta and the frame are defined as rigid bodies whose borders are non-slip wall boundary conditions of the fluid domain. The flow is generated using inlet and outlet conditions, imposed far from the zone of interest. One typical cycle of the flow rate signal measured during the experiment is imposed as a periodic inlet condition (see Fig 4.2 (a)). Given the relatively high value of the Womersley number W_0, the assumption of a flat velocity profile is made to impose the inlet flow rate signal. The inlet velocity is imposed as a Dirichlet condition normal to the inlet boundary, whereas the outlet is defined by imposing a uniform convective velocity which insures the global mass conservation. In order to avoid incoming flow at the outlet boundary, the inlet and outlet boundaries are switched depending if the flow rate

is positive or negative. The systole is thus imposed upstream of the valve, whereas the diastole is imposed downstream.

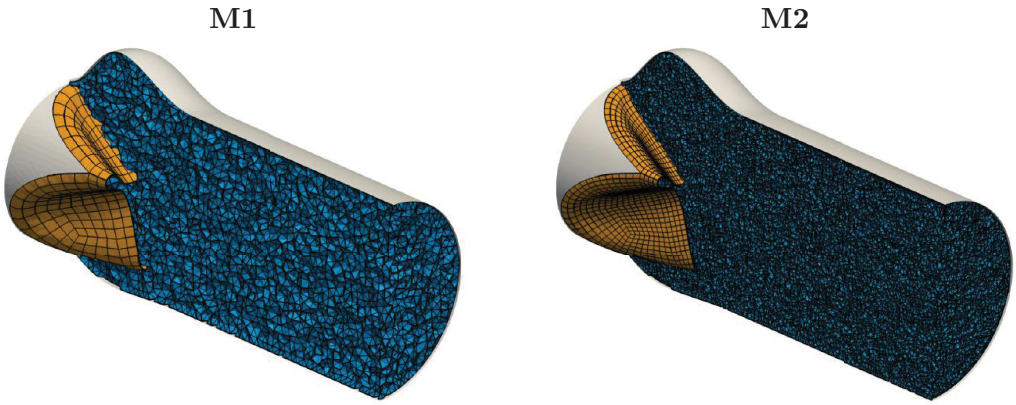

Figure 4.4: Computational zone of interest composed of the valve solid mesh and the aortic fluid mesh. Two levels of mesh are considered, the coarse mesh M_1 and the fine mesh M_2.

The whole computational zone of interest is displayed in Fig. 4.4. Two different levels of mesh are considered in the present study. The mesh M_1 referred to as the coarse mesh, whose fluid mesh is composed of 470 791 tetrahedral elements with a uniform mesh resolution of 1 mm, and whose solid mesh is composed of 384 quadratic hexahedral elements with a mesh resolution of 1 mm. The mesh M_2 referred to as the fine mesh, whose fluid mesh is composed of 3 381 583 tetrahedral elements with a uniform mesh resolution of 0.5 mm, and whose solid mesh is composed of 1536 quadratic hexahedral elements with a mesh resolution of 0.5 mm. Note that similar mesh resolutions are used for the fluid and the solid mesh, which is recommended when using the ITBM. One cycle takes about 1 hour to compute on 24 Intel E5-2690 @2.6GHz processors for mesh M_1, and about 10 hours on 48 processors for mesh M_2.

4.3 Results

4.3.1 Valve dynamics

Figure 4.5 (a) shows several snapshots of the valve movement recorded from the top by the high-speed camera, extracted over different instants of the cardiac cycle (depicted with red dots on the flow rate curve). Corresponding snapshots of the valve deformation extracted from a typical cycle of the simulation are displayed in Fig. 4.5 (b). The 3 leaflets are labeled to ease results presentation. The evolution of the opening area of the valve is also provided in Fig. 4.5 (c), as well as the evolution of the tips locations (midpoints of leaflets edges) of the 3 leaflets in Fig. 4.5 (d).

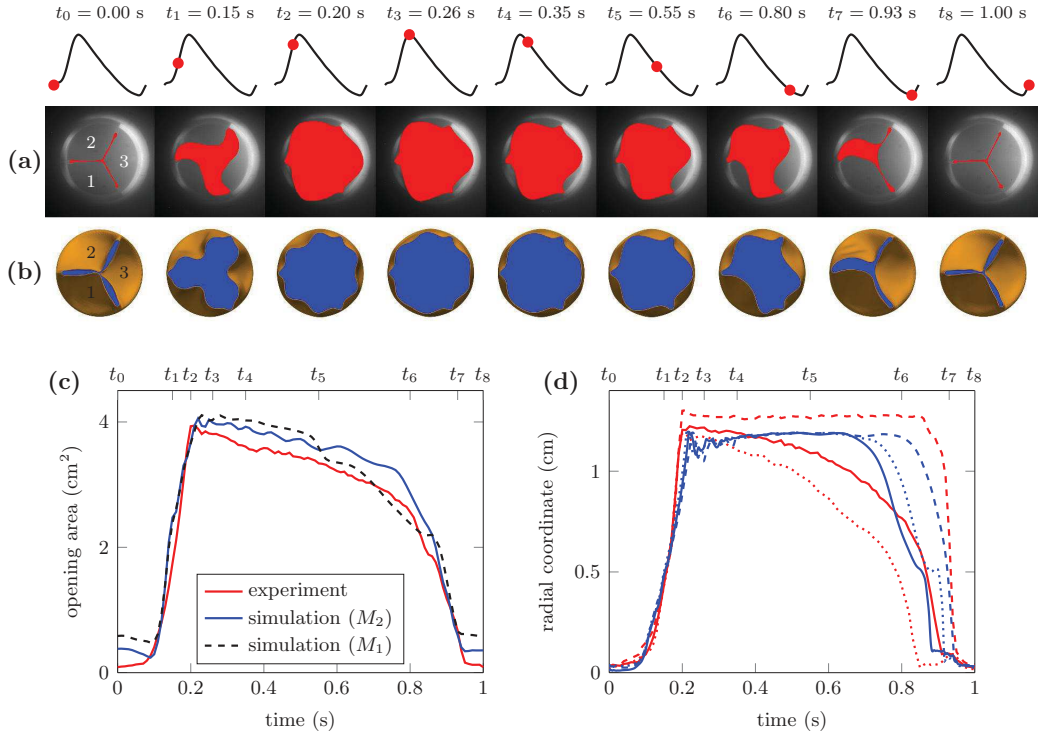

Figure 4.5: **(a)** Snapshots extracted from the valve movement recording at various instants of the cardiac cycle (depicted with red dots on the flow rate curve). **(b)** Corresponding snapshots of the valve deformation extracted from a typical cycle of the simulation. **(c)** Evolution of the opening area of the valve during the cardiac cycle. **(d)** Evolution of the tips locations of the 3 leaflets. Solid line corresponds to leaflet 1, dashed line to leaflet 2, and dotted line to leaflet 3. (red: experiment, blue: simulation for the fine mesh M_2).

In both the experiment and the simulation, the valve shows a strong resistance to flexural deformation. The openings of the experimental and simulated valve are comparable. As seen in Fig. 4.5 (d), the 3 leaflets open simultaneously at the same opening times (between t_0 and t_2). After complete valve opening (after t_2), the 3 leaflets of the experimental valve behave slightly differently. Leaflets 1 and 3 start closing directly after the peak flow rate (which is reached at t_3) when the flow rate decreases, with an earlier closure for leaflet 3. Conversely, leaflet 2 reaches an equilibrium state indicating a buckling phenomenon. Closure of the leaflet suddenly occurs between t_6 and t_7, due to the unbuckling of the leaflet resulting from the diastolic backflow.

In the simulation, the valve opening is followed by a fluttering of the leaflets tips (between t_2 and t_4), as also observed in the experimental study of Moore and Dasi [136]. All the 3 leaflets then reach an equilibrium buckled state. For the cardiac cycle considered, leaflet 1 is the first one to close, followed by leaflet 3, and finally leaflet 2, which closes at the same time than in the experiment (see also snapshots of t_7 in Fig. 4.5 (a), (b)).

Although the detailed dynamics of the experimental and simulated valves slightly

differ regarding the evolution of the tips locations of the 3 leaflets, a good quantitative agreement is obtained regarding the global dynamics given by the evolution of the opening area of the valve (Fig. 4.5 (c)), even when the coarse mesh M_1 is considered. The opening area first quickly increases during valve opening, resulting from the simultaneous opening of the leaflets. The opening section of the valve then gradually decreases, due to the progressive closure of leaflets 1 and 3 in the experiment, and due to a reduction of the opening area near the commissures of the valve in the simulation (see instants t_4 and t_5 in Fig. 4.5 (b)). While a strong fluttering of the leaflets tips is observed between t_2 and t_4 (in Fig. 4.5 (d)), a fluttering phenomenon on the opening area evolution is still observed between t_4 and t_6, induced by the commissures of the valve which fluctuate (not shown).

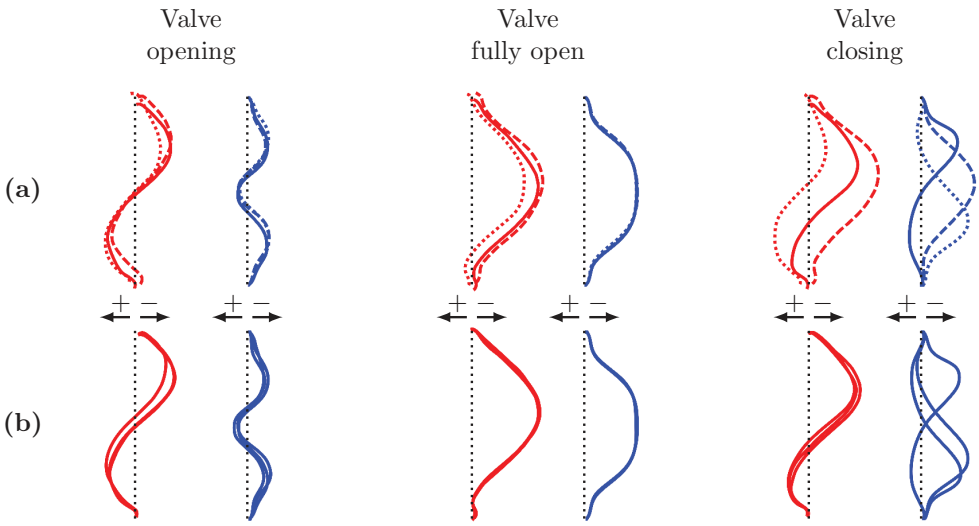

Figure 4.6: **(a)** Shape of the 3 leaflet edges observed during valve opening ($t_1 = 0.15$ s), valve open position ($t_4 = 0.35$ s) and valve closure ($t_6 = 0.80$ s). Solid line corresponds to leaflet edge 1, dashed line to leaflet edge 2, and dotted line to leaflet edge 3. **(b)** Shape of the leaflet edge 1 observed during valve opening, valve fully open and valve closure, for 3 successive cycles. (+: outer radial direction, −: inner radial direction) (red: experiment, blue: simulation for the fine mesh M_2).

The dynamic of the leaflet edges during valve opening, valve open position and valve closure is further analyzed in Fig. 4.6. The shapes of the 3 leaflets are first compared for a given cardiac cycle in Fig. 4.6 (a). In the experiment, the leaflets open with 2 curvature modes with a clockwise propagating curvature. In the simulation however, the deformation of the leaflets is symmetric and composed of 3 modes of curvature. Note that such 3-mode openings were already observed in previous experimental studies performed on BHVs [74, 198]. When the valve is fully open, the curvature of the valve is completely reversed with one unique mode of deformation. A small dissymmetry of the experimental valve is observed whereas the simulated valve is perfectly symmetric. During the experimental valve closure, the leaflets recover their closed configuration again with 2 curvature modes, with

this time a counterclockwise propagating curvature. In the simulation the leaflets also close with 2 curvature modes but the curvature propagates either toward one commissure or the other.

In order to see if this dynamic is reproducible on several cardiac cycles, the shape of leaflet 1 is compared for 3 successive cycles. It is seen that the dynamic of the experimental valve is virtually reproducible, but the simulated valve exhibits some cycle-to-cycle variations, especially during the valve closure. There is actually no privileged direction, from one cycle to the other, for the propagation of the curvature when the leaflets unbuckle. We also observed that the order of closure of the leaflets (visible in Fig. 4.5 (d)) can change from one cycle to the other (not shown). These cycle-to-cycle variations come from the buckling of the leaflets which is a very sensitive and unstable phenomenon. In the experiment, the dynamic of the valve is more reproducible due to the dissymmetry of the valve which enables one leaflet only to properly buckle (as seen in Fig. 4.5 (d)).

4.3.2 Leaflets stress distribution

Figure 4.7 shows the leaflets Von Mises stress distribution obtained from the simulation during valve opening, valve fully open and valve closure. Stress patterns are mostly located in the region where the leaflets experience high flexural deformation. Maximum stresses are observed along the junction between leaflets and the rigid frame, particularly in the basal region. The ideal valve design should thus minimize regions of high curvature. In this sense, the 2-mode curvature observed during the opening of the experimental valve (in Fig. 4.6) would minimize the stresses undergone by the valve leaflets compared to the 3-mode curvature observed on the simulated valve. Conversely, the reproducible counterclockwise curvature propagation observed during the experimental valve closure would privilege regions of repeated stresses which can lead to the fatigue rupture of the leaflets. The cycle-to-cycle variations observed during the simulated valve closure enable a more uniform stress repartition over the leaflets surface.

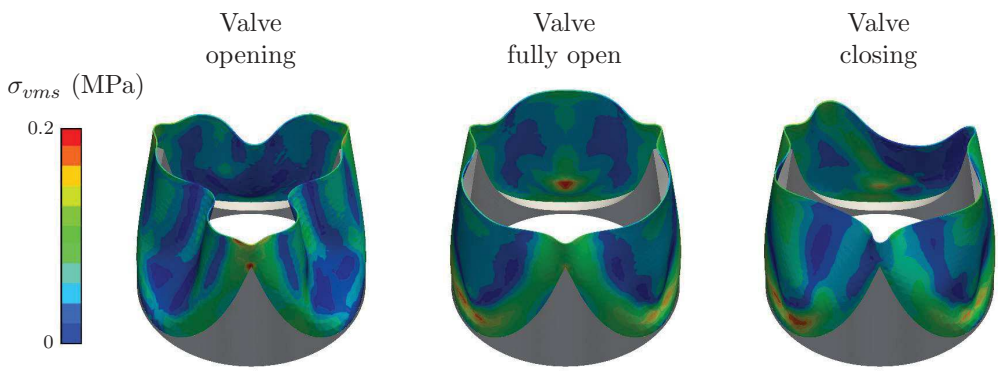

Figure 4.7: Leaflets Von Mises stress distribution during valve opening ($t_1 = 0.15$ s), valve open position ($t_4 = 0.35$ s) and valve closure ($t_6 = 0.80$ s).

4.3.3 Flow dynamics

The two-dimensional velocity field (u, v) downstream of the valve is reconstructed from the PIV measurements in the centerplane of the aortic geometry, where u is the streamwise velocity component and v the transverse velocity component. The streamwise velocity fields obtained from both the experiment and the simulation are displayed in Fig. 4.8. Four characteristic instants of the cardiac cycle are shown: $t = 0.20$ s, just before the flow rate reaches its maximum value, referred to as Early Systole (ES); $t = 0.26$ s, when the flow rate is maximum, referred to as Peak Systole (PS); $t = 0.35$ s, just after the flow rate reaches its maximum value and begins to decrease, referred to as Mid-Systole (MS); $t = 0.55$ s, when the flow rate is decreasing, referred to as Late Systole (LS). The color scale was chosen such that red regions correspond to positive velocity, whereas negative velocity regions appear in blue. The velocity fluctuations downstream of the valve are also investigated by calculating the experimental and numerical streamwise root-mean square (RMS) velocity fields on 24 successive cardiac cycles, as seen in Fig. 4.9. The local extrema of the velocity RMS fields are indicated by different labels (black labels for the experiment, and white labels for the simulation), enabling to identify different flow features. The same labels are reported in the velocity fields of Fig. 4.8 in order to characterize the source of these fluctuations.

At ES, a jet starts to emerge from the valve. In the experiment, the jet is widely spread compared to the simulation, and seems to be slightly tilted towards the sinus side of the aorta. Patterns of fluctuations are observed along the contour of the jet (see labels 1a, 2a, 3a). In the simulation, most of the fluctuations are observed along the leaflet (see label 1b).

At PS, the jet propagates downstream of the valve and grows broader in its shape. Recirculation of the flow is observed along both the sinus and commissure sides of the aorta, as indicated by the negative velocities. Coherent patterns of fluctuations are observed at different critical locations of the jet structure: At the tip of the leaflet (see labels 5a vs. 2b), near to the shear layers generated by the recirculation of the jet (see labels 6a vs. 3b and 7a vs. 4b), and at the apex of the jet towards the sinus side of the aorta (see labels 8a vs. 5b). Regarding the structure of the jet, the flow seems to remain laminar, the fluctuations of velocity being related to cycle-to-cycle variations in the shear layer positions and in the dynamics of coherent structures.

At MS, the jet progresses further downstream of the valve, and the recirculation zones get stronger near the aorta wall, both at the commissure and the sinus sides. The flow seems to transition from laminar to turbulent along the shear layers: larger patterns of fluctuations are indeed observed at the commissure side (see labels 11a, 12a, 13a vs. 6b, 7b) and at the sinus side of the aorta (see labels 14a, 15a vs. 8b, 9b), in the wake of the valve. Such spread patterns indicate a production of turbulence downstream of the valve. For both the experiment and the simulation, the maximum fluctuations are observed at the commissure side of the aorta.

At LS, when the flow rate decreases, the jet decelerates and the recirculation velocities decrease. The two large patterns of fluctuations observed at MS are still identifiable at the commissure side (see labels 16a, 17a, 18a vs. 10b, 11b) and sinus side of the aorta (see labels 19a, 20a, 21a vs. 12b). Patterns are however more spread and start to dissipate downstream of the valve.

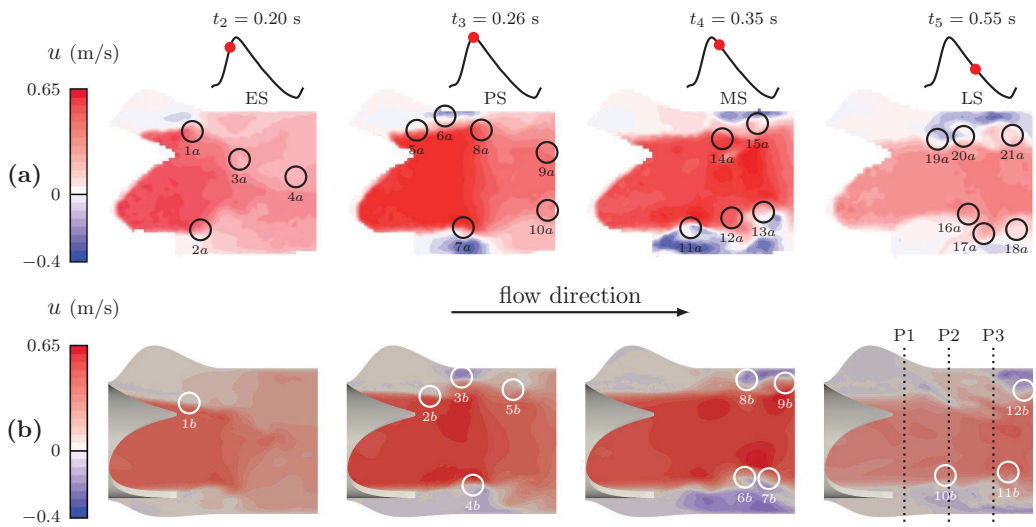

Figure 4.8: **(a)** Fields of instantaneous streamwise velocity obtained from the experiment. **(b)** Fields of instantaneous streamwise velocity obtained from the simulation for the fine mesh M_2. Four different instants of the cardiac cycle are depicted (ES, PS, MS and LS).

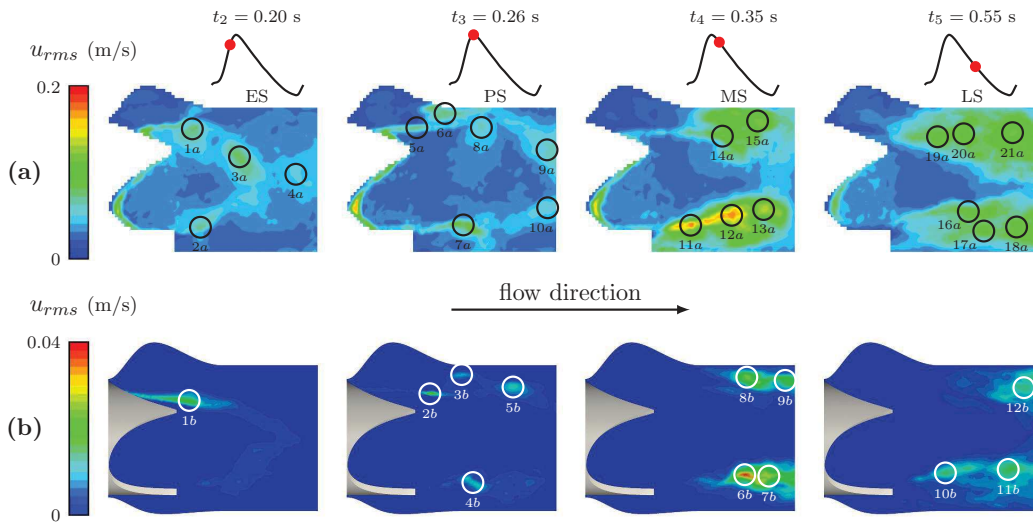

Figure 4.9: **(a)** Fields of streamwise RMS velocity obtained from the experiment. **(b)** Fields of streamwise RMS velocity obtained from the simulation for the fine mesh M_2. Four different instants of the cardiac cycle are depicted (ES, PS, MS and LS).

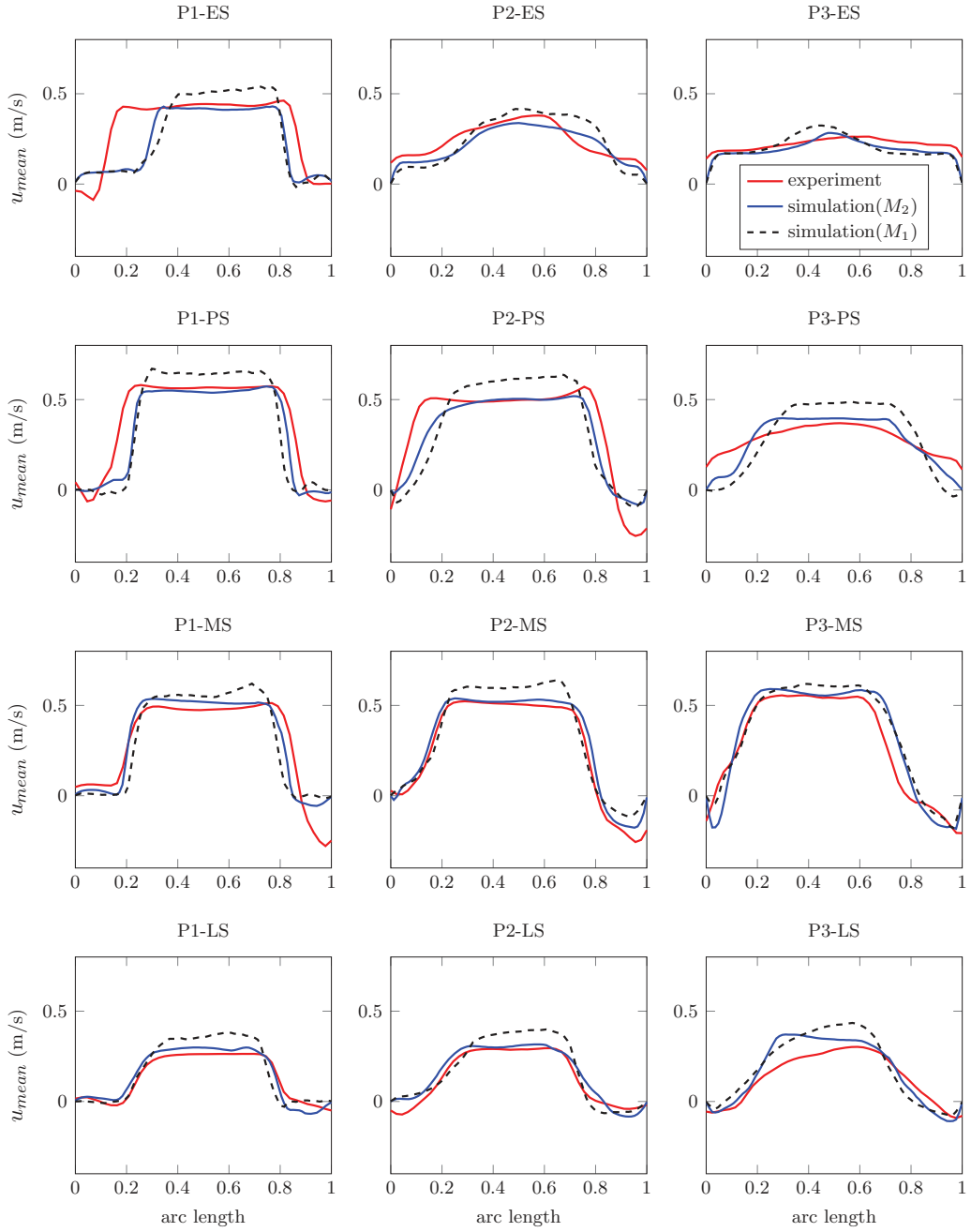

Figure 4.10: Comparison of the experiment (red) and the simulations for meshes M_1 (black) and M_2 (blue), for 3 successive phase-averaged velocity profiles downstream of the valve. Four different instants of the cardiac cycle are depicted (ES, PS, MS and LS).

The experiment and the simulation results are thus qualitatively in good agreement. The main flow features and patterns of fluctuations are similar (both for the coarse mesh M_1 and the fine mesh M_2). However, the simulation seems to underestimate the backflow induced by the recirculation of the jet compared to the experiment. Note also that the magnitude of the fluctuations observed in the experiment is much higher than in the simulation (with maximum fluctuations of 0.2

m/s in the experiment against 0.04 m/s in the simulation, both for meshes M_1 and M_2). Moreover, the patterns are much more concentrated in the simulation, and are conversely more spread in the experiment. This difference is further commented in the discussion section.

In order to quantitatively compare the experimental flow and the numerical flow, phase-averaged velocity profiles are displayed in Fig. 4.10. Three successive velocity profiles downstream of the valve are compared, referred to as profile 1 (P1) which is located directly behind the valve, profile 2 (P2) and profile 3 (P3) which are located further downstream of the valve (see Fig. 4.8 for the exact locations). Given the high complexity of the flow, the experimental and numerical velocity profiles are generally in a very satisfactory agreement, even when the coarse mesh M_1 is used. The fine mesh M_2 however seems to provide a better agreement with the experiment. However, few discrepancies are observed. A more pinched numerical velocity profile is observed on P1 when the jet emerges from the valve at ES (see P1-ES). In addition, the simulation does not show the strong backflow observed along the commissure side of the aorta (see P2-PS and P1-MS) in the experiment. Note that these differences are robust to the change of mesh, so that they are not the result of an insufficient mesh resolution. These discrepancies were expected given that the detailed dynamics (notably the buckling dynamics) of the three leaflets differ in the experiment and in the simulation (see Fig. 4.6 (d)).

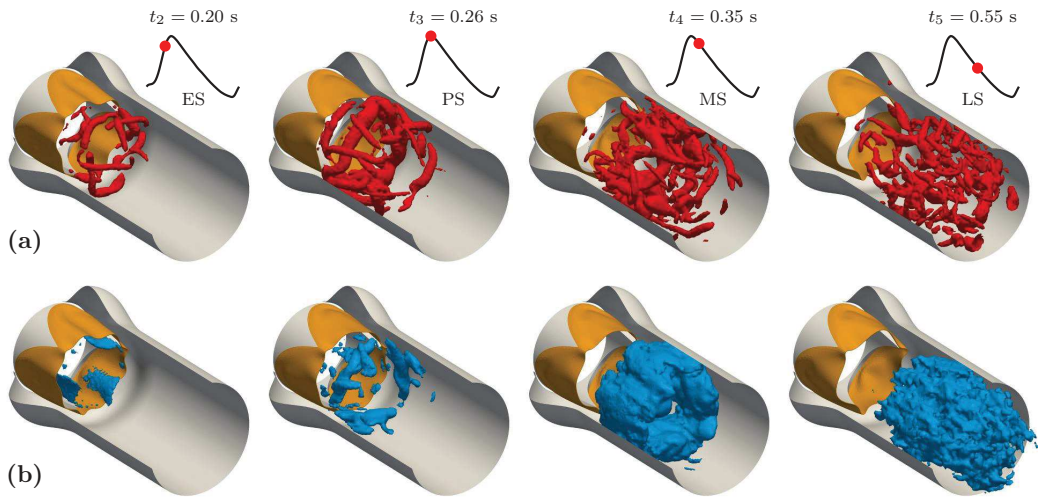

Figure 4.11: **(a)** Iso-surfaces of the instantaneous Q-criterion for the iso-value of 5000 s^{-2}. **(b)** Iso-surfaces of the fluctuating kinetic energy for the iso-value of 0.08 $J.m^{-3}$. Four different instants of the cardiac cycle are depicted (ES, PS, MS and LS).

Figure 4.11 (a) shows iso-surfaces of the instantaneous Q-criterion [94] to visualize instantaneous vortical structures. Figure 4.11 (b) shows iso-surfaces of the fluctuating kinetic energy (b), defined as $FKE = \frac{\rho}{2}\left(u_{rms}^2 + v_{rms}^2 + w_{rms}^2\right)$. At ES, vortical structures (Fig. 4.11 (a)) are shed downstream of the valve commissures, at

the tips of the rigid frame. These structures propagate between ES and MS over an annular region in the wake of the valve. At LS, the vortical structures are smaller and spread over the lumen of the aorta.

Figure 4.11 (b) enables to better visualize the organization of the velocity fluctuations patterns, partially presented in Fig. 4.9 over the centerplane of the aortic geometry. At ES, velocity fluctuations are related to the fluctuations of position of the shear layers along the leaflets. On the contrary, at PS, high FKE values are related to strong vortices shed downstream of the valve commissures. At PS, the iso-surface of FKE demonstrates that fluctuations are much higher downstream of the commissure than downstream of the leaflet: remarkably, the fixed part of the valve generates more turbulence than the leaflets. Between PS and MS, the transition from laminar to turbulent is clearly suspected by the strong increase and spreading of the FKE level in the wake of the valve. The iso-surface of FKE is rather toroidal at MS, showing that the turbulence region is localized in the valve wake. At LS, the FKE iso-surface spreads over a wider volume of the aorta, as anticipated from the Q-criterion view.

4.4 Discussion

In the present work, the complex fluid-structure interaction problem involved when blood flows out of the left ventricle and passes through the aortic valve is investigated. Experimental investigations carried out on an in-vitro configuration of an artificial flexible aortic valve are combined with numerical simulation performed with a dedicated FSI model.

Investigations of the valve kinematics show that despite a similar global dynamic observed between the experimental and simulated valves, the detailed dynamics of the valve leaflets are significantly different, due to a symmetry breaking in the experiment. This potentially leads to different leaflets stresses distribution. The characterization of valve designs should thus rely on a detailed analysis of the individual dynamic of the valve leaflets, rather than on a global analysis.

Investigations of the flow downstream of the valve reveal that the flow transitions to turbulence. This transition occurs after peak systole, when the flow starts to decelerate. Patterns of fluctuating kinetic energy are observed in the wake of the valve, and then spread in the lumen of the aorta. The authors originally expected a maximum level of fluctuations at the sinus side of the aorta, in the wake of the leaflets tips. However, the present study shows that fluctuations are maximum at the commissure side of the aorta, both in the experiment and the simulation. This should be induced by the significant thickness of the rigid frame maintaining the leaflets, which is seen as a backward-facing step known to generate turbulence [97]. These observations should be considered for future valve developments.

Discrepancies are observed when analyzing the individual dynamic of the leaflets, with a 2-mode opening observed in the experiment against a 3-mode opening observed in the simulation. This symmetric 3-mode opening is expected given the symmetry of the geometry and flow conditions of the computational setup. The non-symmetric swirl motion observed in the experiment can be explained by the dissymmetry observed in the experimental valve, probably induced by the manual heat treatment performed on the leaflets to obtain the closed design of the valve. In spite of these differences, the phase-averaged velocity fields are very similar in the simulation and in the experiment. However, the simulation underestimates the levels of velocity fluctuations measured in the experiment, even if it provides a good qualitative agreement with the experiment in terms of velocity fluctuations structure. In the experiment, much higher levels of fluctuations are observed upstream of the valve, which indicates a possible production of turbulence of the rotatory pump which is used to generate the flow. In addition, the flow rate measured in the experiment exhibits some cycle-to-cycle variations which are not taken into account in the simulation (the same flow rate is imposed for all the cycles simulated). This points out the complexity of carrying out such a combined experimental and numerical study, especially in this very sensitive configuration involving fluid-structure interaction.

The FSI model used in the present study has demonstrated its ability to compute the flow through aortic valves, and could be used for potential clinical applications. As pointed out by Sotiropoulos *et al.* [176], the location and orientation of prosthetic valve implantation play an important role in the resulting hemodynamics, and can affect the long-term success of valve replacement. Such a numerical tool could thus be used to predict the procedure outcome for the patient after valve implantation, and further improve the development of new flexible valve prostheses.

4.5 Supplementary material

4.5.1 Overall PIV-vs-CFD comparison

A more comprehensive PIV-vs-CFD comparison is provided in the present section. Note that some figures previously shown are reproduced here for completeness.

- The fields of instantaneous streamwise velocity at both the centerplane and the 6 mm offplane of the aortic geometry are displayed in Figs. 4.12 and 4.13, respectively. Note that Fig. 4.12 corresponds to Fig. 4.8 of section 4.3.3.
- The fields of averaged streamwise velocity at both the centerplane and the 6 mm offplane of the aortic geometry are displayed in Figs. 4.14 and 4.15, respectively.
- The fields of streamwise RMS velocity at both the centerplane and the 6 mm offplane of the aortic geometry are displayed in Figs. 4.16 and 4.17, respectively. Note that Fig. 4.16 corresponds to Fig. 4.9 of section 4.3.3.

- Averaged streamwise and transverse velocity profiles are displayed in Figs. 4.18 and 4.19, respectively. Note that Fig. 4.18 corresponds to Fig. 4.10 of section 4.3.3.

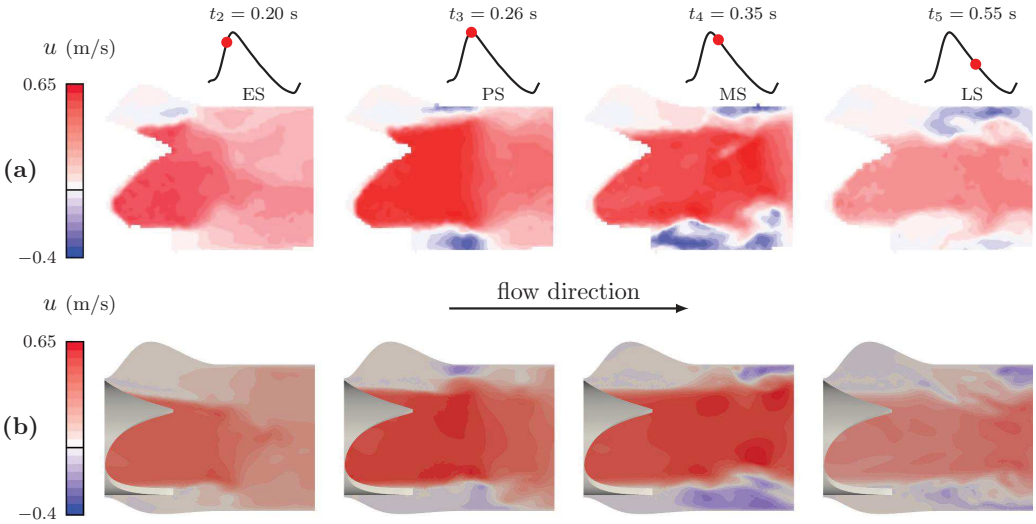

Figure 4.12: Fields of instantaneous streamwise velocity at the centerplane of the aortic geometry. **(a)** Experiment; **(b)** Simulation (M_2).

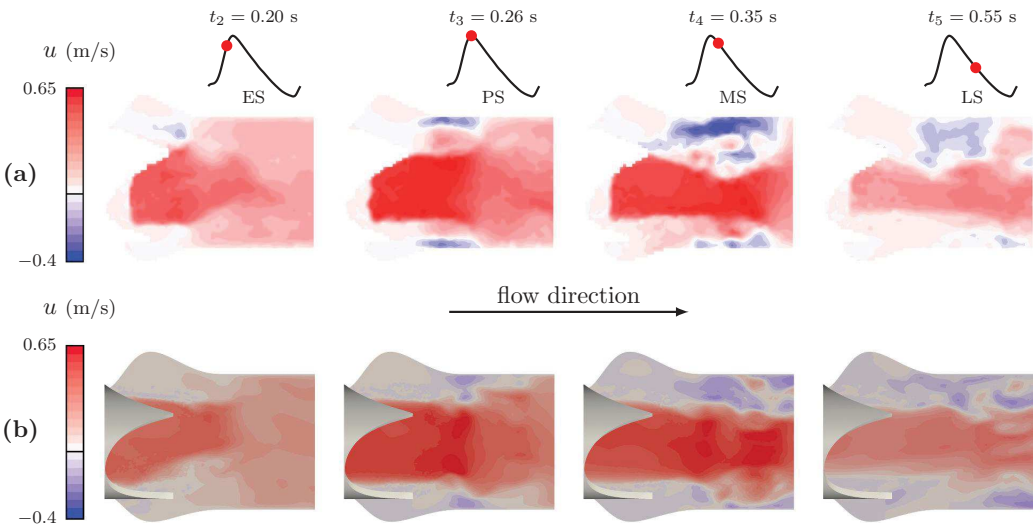

Figure 4.13: Fields of instantaneous streamwise velocity at the 6 mm offplane of the aortic geometry. **(a)** Experiment; **(b)** Simulation (M_2).

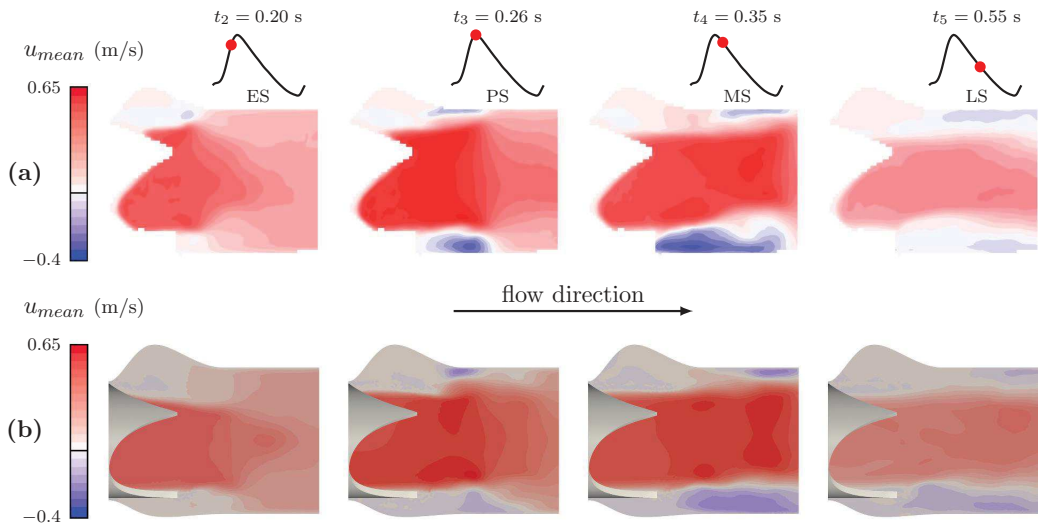

Figure 4.14: Fields of averaged streamwise velocity at the centerplane of the aortic geometry. **(a)** Experiment; **(b)** Simulation (M_2).

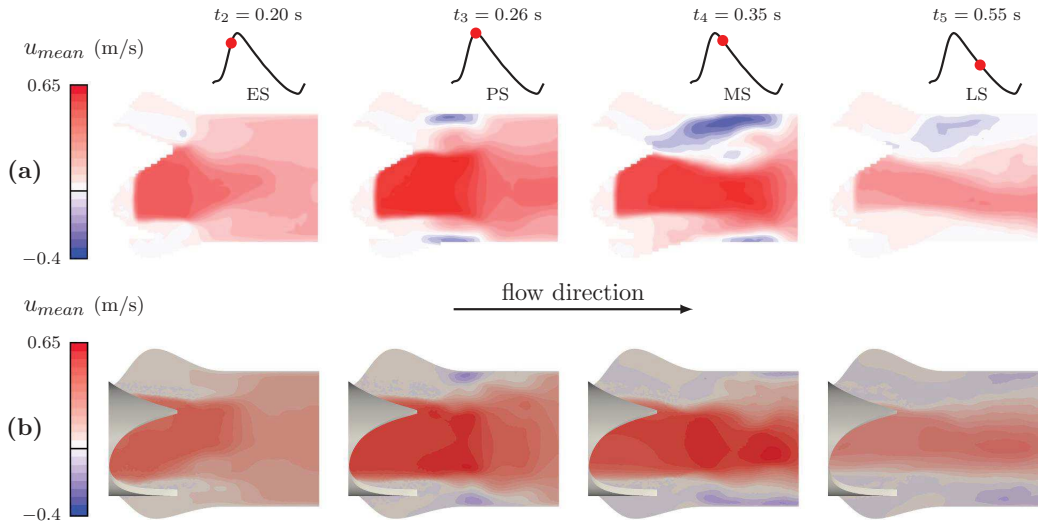

Figure 4.15: Fields of averaged streamwise velocity at the 6 mm offplane of the aortic geometry. **(a)** Experiment; **(b)** Simulation (M_2).

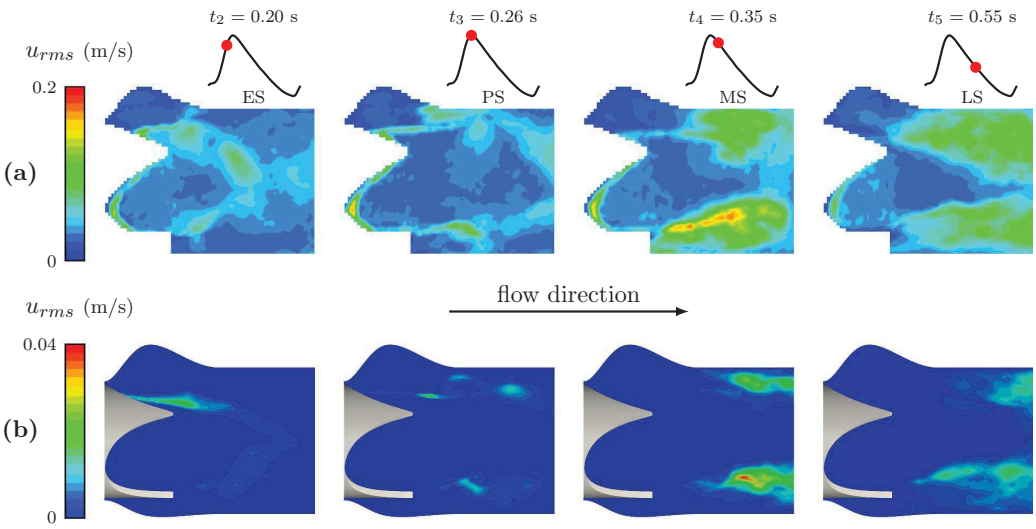

Figure 4.16: Fields of streamwise RMS velocity at the centerplane of the aortic geometry. **(a)** Experiment; **(b)** Simulation (M_2).

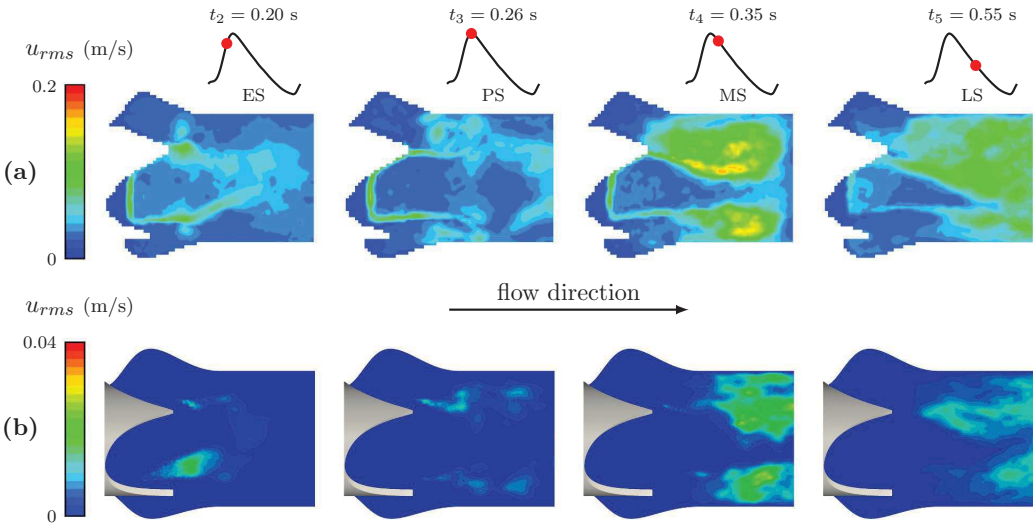

Figure 4.17: Fields of streamwise RMS velocity at the 6 mm offplane of the aortic geometry. **(a)** Experiment; **(b)** Simulation (M_2).

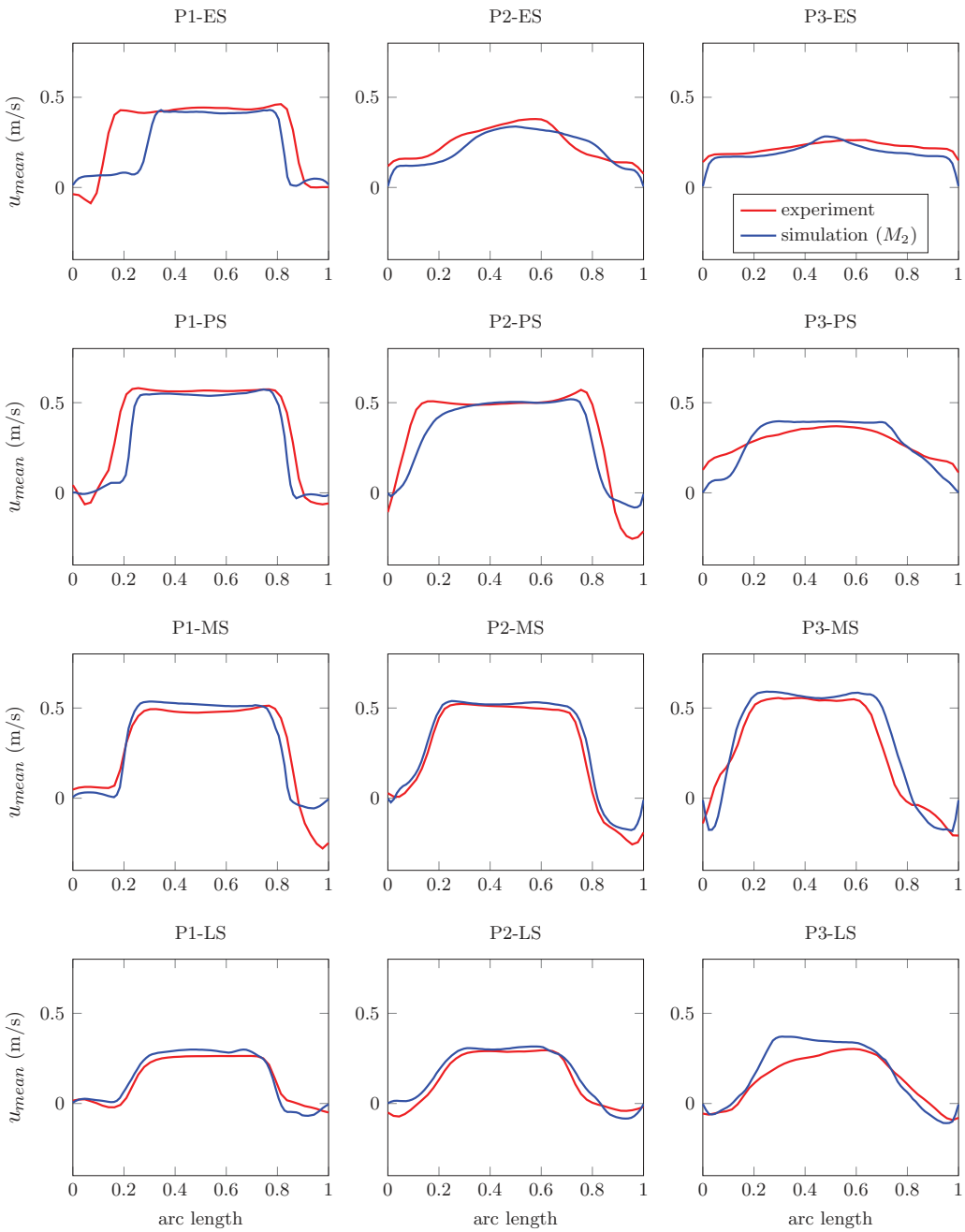

Figure 4.18: Averaged streamwise velocity profiles. (red: experiment, blue: simulation).

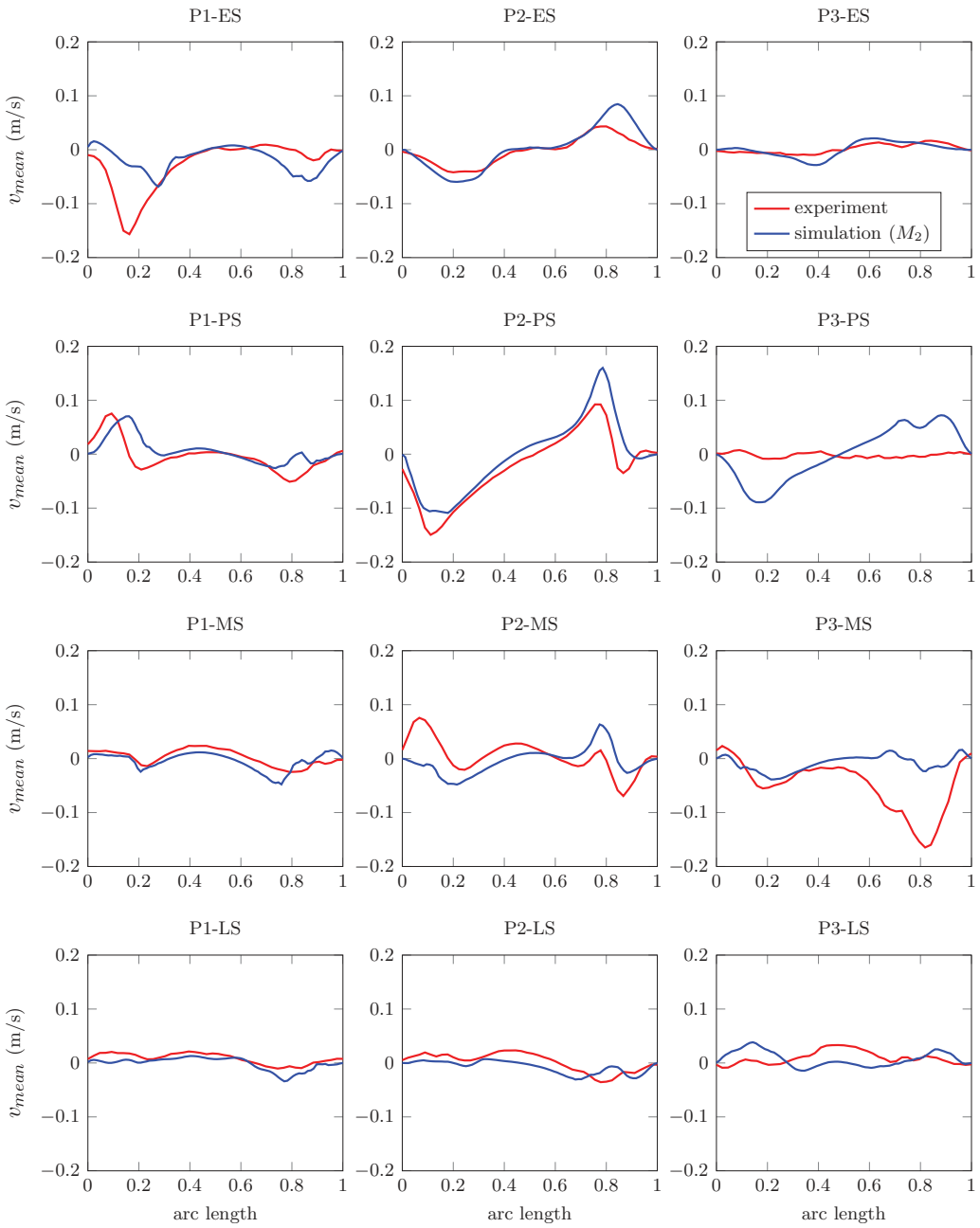

Figure 4.19: Averaged transverse velocity profiles. (red: experiment, blue: simulation).

The good agreement previously obtained between the experiment and the simulation is corroborated by the present comprehensive comparison, which enables to give more confidence to the validation. The main features of the flow are faithfully captured by the simulation, both at the centerplane (Figs. 4.12, 4.14 and 4.16) and at the 6 mm offplane (Figs. 4.13, 4.15 and 4.17) of the aortic geometry. Regarding the averaged streamwise and transverse velocity profiles (Figs. 4.18 and 4.19, respectively), it is seen that a less satisfactory comparison between the experiment and the simulation is obtained for the transverse velocity, which is most probably more sensitive to the detailed dynamics of the valve leaflets.

4.5.2 Transvalvular pressure gradient

Another quantity of interest when studying the dynamics of aortic valves is the transval-vular pressure gradient (TPG), introduced in chapter 1 (section 1.1.1). Pressure has thus been recorded at two locations downstream (ventricular side) and upstream (aortic side) of the valve. The evolution of the TPG is displayed in Fig. 4.20 (a), where the experimental measurement is compared with the numerical prediction. Note that two shrinkage parameters (see section 4.2.3) are tested for the simulation: $r = 2$ mm and $r = 3$ mm. The evolution of the TPG can be correlated with the global dynamics of the valve, in terms of opening area (Fig. 4.20 (b)).

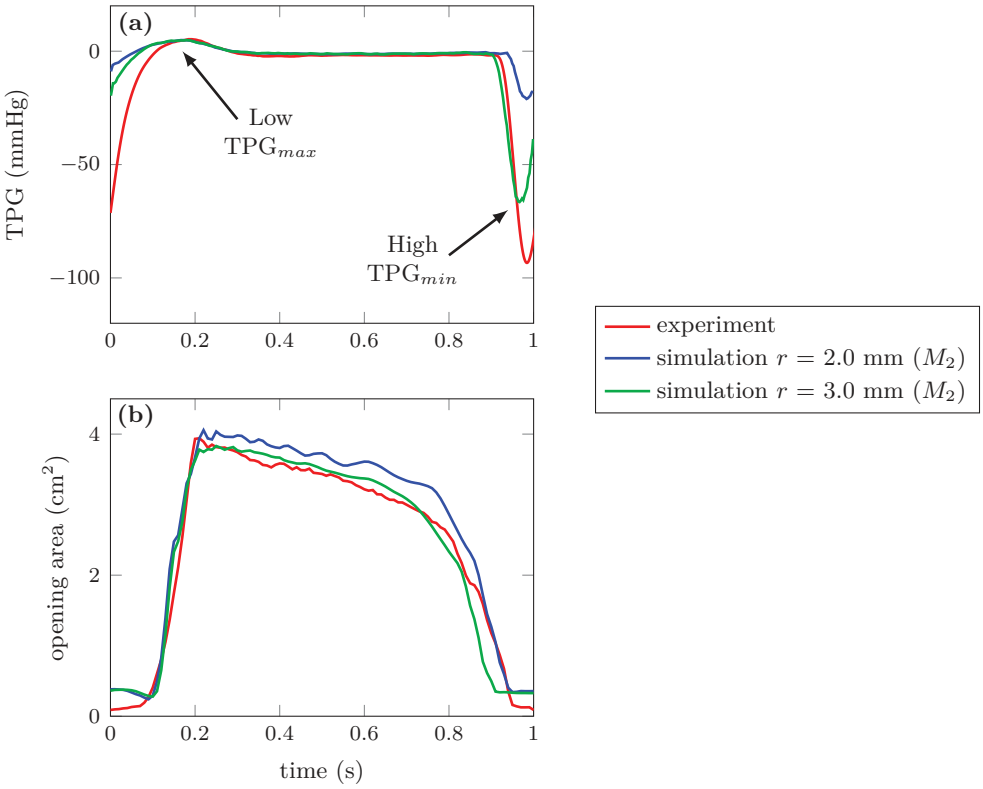

Figure 4.20: **(a)** Evolution of the transvalvular pressure gradient (TPG). **(b)** Evolution of the valve opening area. (red: experiment, blue: $r = 2$ mm, green: $r = 3$ mm).

It is seen that a low positive peak of TPG is reached at the beginning of the systole, when the valve is opening. Conversely, a high negative peak of TPG is reached during the diastole, when the valve is fully closed. This observation is consistent with the physiological dynamics of the aortic valve, described in chapter 1 (section 1.1.1): the TPG required to drive the blood through the aortic valve during systole is of the order of only few mmHg, whereas the aortic valve undergoes a negative TPG of about 80 mmHg during diastole. The maximum and minimum values of the TPG are displayed in Tab. 4.2, where experimental values can be compared with numerical values. It can first be noted that the experimental maximum and minimum TPG values are close to physiological values. Indeed, a TPG of 5.28 mmHg is required to open the valve during systole, whereas the TPG undergone by the valve during diastole is -93.35 mmHg. Comparing the experimental TPG values with the numerical ones, it is seen that the simulation faithfully reproduce the systolic TPG_{max}. Both tested shrinkage parameters predict the same value of TPG_{max}, which is slightly lower than the experimental value. The simulation however fails to reproduce the diastolic TPG_{min} measured during the experiment. The value of TPG_{min} predicted for the shrinkage parameter $r = 2$ mm is drastically lower than the experimental value. A possible explanation for this discrepancy is the short delay in the valve closure observed for $r = 2$ mm as compared to the experiment (see Fig. 4.20 (b)). Using a shrinkage parameter $r = 3$ mm, the valve this time closes slightly earlier than in the experiment, which should lead to an overestimation of the diastolic TPG_{min}. Yet the predicted value of TPG_{min} is still lower than the experimental value, although in better agreement than for $r = 2$ mm.

	Experiment	Simulation (M_2)	
		$r = 2$ mm	$r = 3$ mm
TPG_{max} (mmHg)	5.28	4.90	4.90
TPG_{min} (mmHg)	-93.35	-21.05	-66.52

Table 4.2: Maximum and minimum values of the TPG obtained in the experiment and the simulation.

Valve leakage

This underestimation of the diastolic TPG_{min} is most probably due to a leakage of the valve in the simulation: the flow going through the valve, the TPG is no longer sustained by the valve, as in the case of aortic valve insufficiency (see chapter 1, section 1.1.1). Indeed, there are two main reasons why a valve leakage is heavily suspected:

- The poor closure of the valve observed in the simulation, meaning that the valve leaflets never directly get into contact (see Fig. 4.21 (a)).
- The small permeability of the valve leaflets, which is inherent to the IBM formalism.

Figure 4.21 shows that the first option is hardly conceivable. When the valve is supposed to be closed at $t = 0.95$ s (see Fig. 4.21 (a)), a small gap between the leaflets still remains. This however does not imply that the flow goes through this gap, and that the valve is leaking. As a matter of fact, the fluid sees the valve through the volumetric force $\overrightarrow{f}$ which comes from the regularization of the valve mechanical force $\overrightarrow{F}$ (see section 4.2.1). This mechanical force $\overrightarrow{F}$ is regularized on a patch of fluid elements located at the neighboring of the valve (see Fig. 4.21 (b)), via the smooth discrete Dirac function. One thus easily understands that when there is an overlapping of two patches of fluid elements, corresponding to two different leaflets, this induces a local repulsion of the valve leaflets which are not able to get closer. As seen in (see Fig. 4.21 (b)), when the valve is closed at $t = 0.95$ s, the overlapped patches of fluid elements describe a fully closed valve without any gap.

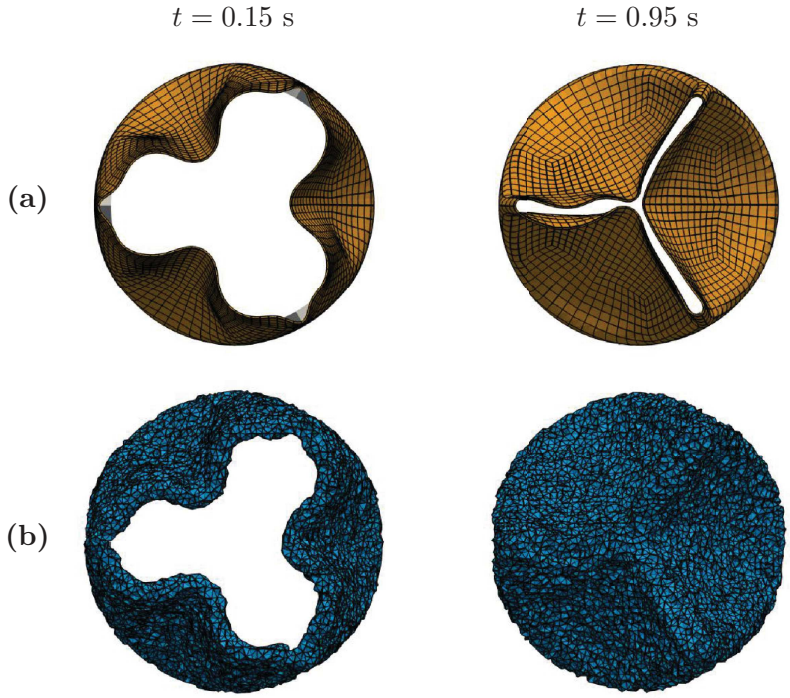

Figure 4.21: **(a)** Deformation of the valve at two different instants of the cardiac cycle ($t = 0.15$ s when the valve is opening, and $t = 0.95$ s when the valve is fully closed). **(b)** Patch of fluid elements on which the mechanical force is regularized, illustrating how the valve is seen by the fluid.

It is thus likely that porous leakage through the leaflets is the origin of the underestimation of the diastolic TPG_{min}. Indeed, the valve may experience continuous leakage during the whole cardiac cycle, because of the errors generated by interpolation procedures of the IBM. The valve leakage is however difficult to quantify, and is expected to increase when the valve highly resists to the flow. Given that the valve slightly resists to forward flow during systole and highly resists to backward flow during diastole, this would explain the large underestimation of the diastolic TPG_{min} and the slight underestimation of the systolic TPG_{max}.

Chapter 5

Conclusion

Chapter contents

5.1 Red blood cells modeling 107
5.2 The immersed thick boundary method 108
5.2.1 Aortic valve computation 109
5.2.2 Perspectives 110

This concluding chapter aims at highlighting the actual research contribution of the present thesis work, and raises some relevant perspectives. The general topic "fluid-structure interaction problems involving deformable membranes" gathers many scientific aspects which have been encountered in this thesis:

- The algorithmic aspect, namely the methodology used to solve these FSI problems,
- The validation strategy used to demonstrate the reliability of the methodology used to solve these FSI problems,
- The modeling strategy used to establish a proper mathematical representation of the physical objects involved in these FSI problems,
- The physical aspect, the ultimate purpose being to understand the physics of these FSI problems.

5.1 Red blood cells modeling

This thesis has first focused on a specific FSI problem, which is the interaction of the red blood cell membrane with its inner and outer fluids. The main question that has been raised is: how to model the complex microstructure of the red blood cell membrane? (described in chapter 1, section 1.1.2). A major stake behind this question is the ability to provide accurate predictions of red blood cells deformation in a wide range of flow conditions, including the ones encountered in blood analyzers (described in chapter 1, section 1.1.3).

Establishing a suitable model of the red blood cell membrane requires to fully characterize its complex mechanics. This can be achieved computing a well-controlled experimental configuration for studying the red blood cell deformation characteristics. By using different membrane models, analysing the discrepancies between numerical and experimental results is a way to determine which one is the most suitable to represent the mechanics of the red blood cell membrane. A literature review has led to select the optical tweezers experiment, which is one of the few experiments which enables to investigate the mechanical behavior of the red blood cells in a large range of deformation. This literature review also revealed that the optical tweezers experiment is widely used to probe the accuracy of solvers dedicated to the study of the red blood cell dynamics under flow, such as the YALES2BIO solver.

Then, the first contribution of this work has been to propose an innovative and easy-to-implement methodology to faithfully simulate the optical tweezers experiment. The idea was then to "play" with the membrane mechanics solver implemented in the solver (described in chapter 1, section 1.4), testing various models of the red blood cell membrane. The initial objective which was to establish a suitable model of the red blood cell membrane has been partially achieved. This numerical study has indeed enabled to identify relevant membrane models, which provide a good matching with the experimental data provided by the optical tweezers experiment. However, the major contribution of this work has been to demonstrate the simplistic nature of these experimental data, which are not selective enough to discriminate between appropriate and inappropriate models. This shows that computing the optical tweezers experiment does not constitute a true validation test case, thus questioning the validity of (some of) the models proposed in the literature for representing the red blood cell membrane. The last contribution of this work has been to show the interest of additional measurements, that could be performed during the optical tweezers experiment. Such data, like for example lengths measured in the direction perpendicular to the plane of the cell, could be more selective and would thus enable to push aside inappropriate membrane models that currently provide a good matching with the optical tweezers experimental data.

5.2 The immersed thick boundary method

This thesis work has also enabled to substantially broaden the field of application of the YALES2BIO solver, which was hitherto limited to the study of the dynamics of red blood cells under flow. The basic idea has been to replace the existing membrane mechanics solver (described in chapter 1, section 1.4), which was especially dedicated to solve the complex mechanics of the red blood cell membrane, by a classical finite element solver: the LMGC90 solver. This finite element solver computes the membrane force on a 3-dimensional Lagrangian mesh, which is handle with the same IBM formalism as previously. The algorithmic work has thus consisted in coupling the fluid mechanics and solid mechanics solvers, without further developments in the IBM formalism itself. The IBM being originally restricted to infinitely thin membranes, this gave rise to a new method called immersed thick boundary

method (ITBM). Numerous test cases have been performed to demonstrate the robustness and accuracy of the method. The main objective has been to demonstrate how highly specialized fluid and solid solvers can be coupled to simulate a wide variety of FSI problems involving 3D continuum membranes, using the ITBM. The result is a numerical tool which benefits from both the high computing capacities of the YALES2 flow solver in complex geometries, and the wide library of materials available in the LMGC90 solid mechanics solver. Moreover, the present method has revealed to be robust enough to handle computations at significantly high Reynolds numbers, thus showing its potential.

Nonetheless, the present ITBM suffers from a major drawback, which is the leakage problem inherent to the IBM formalism. Indeed, the procedures of regularization/interpolation which enable communications between the non-conforming meshes are known to generate numerical errors, which are characterized by a small permeability of the immersed membrane. It has been seen that in the case of closed membranes, the membrane permeability induces a loss of the volume contained within the membrane, which can be corrected with a specific algorithm (detailed in chapter 3, section 3.2.6). In the case of open membranes however, there is no correction performed to compensate the membrane permeability. Still, some of the test cases performed in chapter 3 (section 3.3), especially the one of section 3.3.5, have shown promising results despite of this leakage problem.

Another question that should be considered is the inertia of the membrane, which is presently neglected in the ITBM despite of the finite thickness of the membrane. It has been explained in chapter 3 (section 3.2.1) that this assumption is valid as long as the membrane is thin enough and that the fluid-to-solid density ratio is close to unity. The validity of this assumption should however be quantified for a given thickness and fluid-to-solid density ratio, in order to determine the range of validity of this assumption. It remains that such an assumption restrains the field of application of the present ITBM. Integrating the inertia of the membrane to the ITBM would thus be a valuable improvement of the method.

5.2.1 Aortic valve computation

The ITBM has then been applied to a highly complex FSI problem, which is the interaction of a pulsatile (blood) flow with the aortic valve. The resulting FSI problem is indeed very challenging to simulate, given the significantly high Reynolds number of the flow, and the contact that occurs between the valve leaflets during aortic valve closure. The ability of the ITBM to simulate this FSI problem has been demonstrated comparing numerical simulations, performed with the YALES2BIO solver, with experimental investigations carried out on an in-vitro configuration of a polymeric model of aortic valve under pulsatile flow conditions. This combined experimental and numerical study has led to very promising results, showing that the ITBM is able to faithfully capture the global dynamics of the valve, as well as the main features of the flow downstream of the valve.

The proposed numerical method however showed some limitations in the prediction of the transvalvular pressure gradient (TPG) through the valve, especially the high diastolic TPG observed when the valve is fully closed and undergoes the high pressure from the aorta. This limitation has been attributed to the leakage problem inherent to the IBM formalism, which has been previously mentioned. The development of an algorithm able to correct this valve leakage would thus be of great interest. Indeed, such an algorithm could correct the volume swept by the valve, knowing the flow rate and the actual fluid volume flowing through the valve opening section.

Another issue that needs to be addressed in the near future is the solving of the contact that occurs between the valve leaflets. The results obtained during this thesis support the idea that the ITBM is able to handle the leaflets contact without causing numerical issues. However, it remains unclear if this contact is accurately solved, given that the current IBM formalism prevents the valve leaflets to get into direct contact. In this context, the establishment of a basic test case with contact solving would help in evaluating the ability of the ITBM to accurately solve FSI problems where contacts between deformable membranes are involved.

5.2.2 Perspectives

Despite of the few improvements that are required within the ITBM, the YALES2BIO solver can now be used to tackle a wide variety of FSI problems encountered with biomedical devices.

A first obvious application is the design of artificial flexible heart valves. Indeed, such a numerical tool is expected to bring new insights into the assessment of the prosthetic valve performance [86], which would be a valuable help for the improvement of heart valve designs. The ability of the ITBM to predict complex flow features downstream of a flexible artificial valve has been demonstrated. Performance indicators such as the flow turbulence, fluid shear stresses, blood stagnation and flow separation regions could thus be assessed using the ITBM.

The YALES2BIO solver has also been used to compute the flow within the total artificial heart developed by the CARMAT society[1] [106], showing another relevant application of the ITBM. This very complex device is composed of two cavities (left and right heart) which are covered by large membranes. A pump system is used to put into motion a working fluid (silicon oil), which induces an oscillation of the membranes that enables the blood circulation. Figure 5.1 shows an overview of the computation of the flow within the left cavity of the device performed with the YALES2BIO solver, illustrating the complex interaction of the blood and working fluid with the large membrane covering the cavity.

[1] http://www.carmatsa.com/fr/

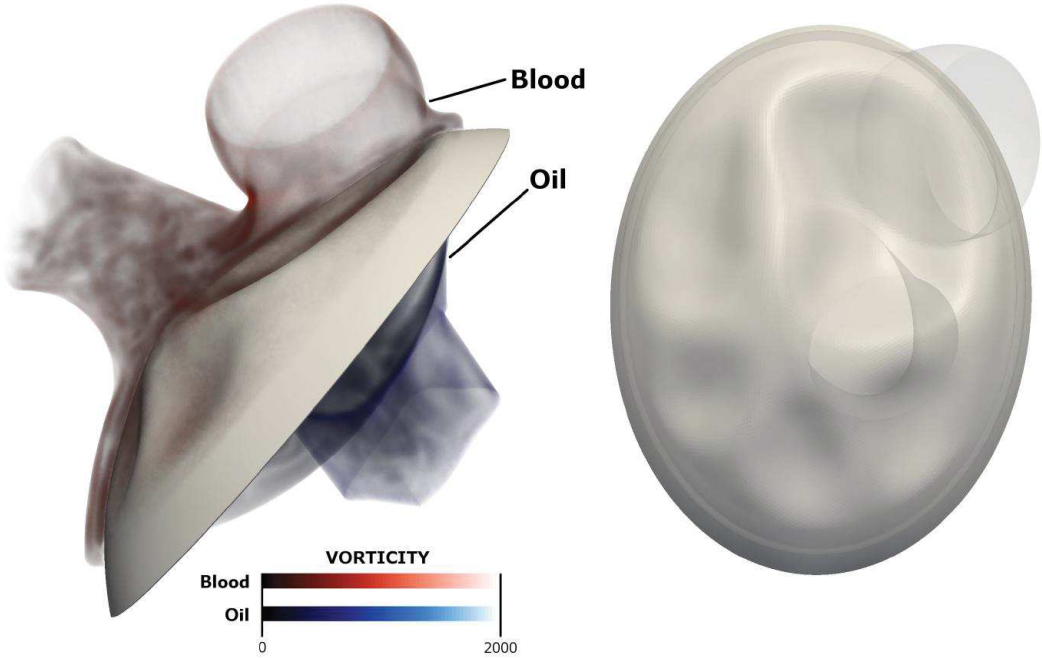

Figure 5.1: Computation of the flow within the left cavity of the total artificial heart developed by the CARMAT society, performed with the YALES2BIO solver (from [106]).

The applications of the present thesis work have been mainly focused on blood flows, simulating FSI problems at the macroscopic and microscopic scales. Although FSI problems involving deformable membranes are widely encountered in biomedical applications, they are also encountered in other areas in which the ITBM could be used. As an example, one can cite the increasing interest in Micro-Air-Vehicles (MAVs) that has pushed research and adaption of bio-inspired membrane wing structures (see Fig. 5.2 for examples). Recent studies show that these thin and flexible membrane wings can improve aerodynamic flight performances [19, 162], creating longer flow attachment and enhancing edge vortex shedding.

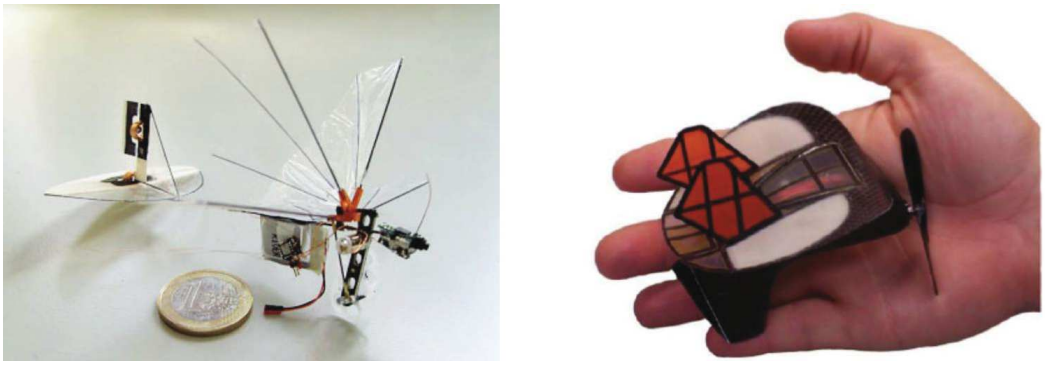

Figure 5.2: Typical examples of Micro-Air-Vehicles using membrane wing structures. (left image from [47], right image from [24]).

Bibliography

[1] M. Abkarian, M. Faivre, R. Horton, K. Smistrup, C. A. Best-Popescu, and H. A. Stone. Cellular-scale hydrodynamics. *Biomed. Mater.*, 3(034011), 2008.

[2] M. Abkarian and A. Viallat. *Fluid-Structure Interactions in Low-Reynolds-Number Flows*, chapter On the importance of red blood cells deformability in blood flow, pages 347–462. Royal Society of Chemistry, 2016.

[3] S. Annerel, T. Claessens, J. Degroote, P. Segers, and J. Vierendeels. Validation of a numerical FSI simulation of an aortic BMHV by in vitro PIV experiments. *Med. Eng. Phys.*, 36:1014–1023, 2014.

[4] M. Astorino, J. F. Gerbeau, O. Pantz, and K.-F. Traoré. Fluid-structure interaction and multi-body contact: Application to aortic valves. *Comput. Meth. Appl. Mech. Eng.*, 198:3603–3612, 2009.

[5] S. Badia, F. Nobile, and C. Vergara. Fluid-structure partitioned procedures based on Robin transmission conditions. *J. Comput. Phys.*, 227:1027–7051, 2008.

[6] P. Bagchi and R. M. Kalluri. Rheology of a dilute suspension of liquid-filled elastic capsules. *Phys. Rev. E*, 81(056320), 2010.

[7] P. Bagchi and R. M. Kalluri. Dynamic rheology of a dilute suspension of elastic capsules: effect of capsule tank-treading, swinging and tumbling. *J. Fluid Mech.*, 669(498–526), 2011.

[8] P. Bagchi and A. Z. K. Yazdani. Analysis of membrane tank-tread of non-spherical capsules and red blood cells. *Eur. Phys. J. E*, 35(12103), 2012.

[9] K. Balachandran, P. Sucosky, H. Jo, and A. P. Yoganathan. Elevated cyclic stretch alters matrix remodeling in aortic valve cusps: implications for degenerative aortic valve disease. *Am. J. Physiol. Heart Circ. Physiol.*, 296(3):H756–H764, 2009.

[10] K. Balachandran, P. Sucosky, H. Jo, and A. P. Yoganathan. Elevated cyclic stretch induces aortic valve calcification in a bone morphogenic protein-dependent manner. *Am. J. Pathol.*, 177(1):49–57, 2010.

[11] D. Barthès-Biesel. Capsule motion in flow: Deformation and membrane buckling. *Comp. Rend. Phys.*, 10(8):764–774, 2009.

[12] D. Barthès-Biesel. Modeling the motion of capsules in flow. *Curr. Op. Coll. & Interf. Sc.*, 16:3–12, 2011.

[13] D. Barthès-Biesel, A. Diaz, and E. Dhenin. Effect of constitutive laws for two-dimensional membranes on flow-induced capsule deformation. *J. Fluid Mech.*, 460:211–222, 2002.

[14] H. Baya Toda, O. Cabrit, K. Truffin, G. Bruneaux, and F. Nicoud. Assessment of subgrid-scale models with a large-eddy simulation-dedicated experimental database: The pulsatile impinging jet in turbulent cross-flow. *Phys. Fluids*, 26(075108), 2014.

[15] J. Beaucourt, F. Rioual, T. Séon, T. Biben, and C. Misbah. Steady to unsteady dynamics of a vesicle in a flow. *Phys. Rev. E*, 69(011906), 2004.

[16] J. G. Betts, P. Desaix, E. Johnson, J. E. Johnson, O. Korol, D. Kruse, B. Poe, J. A. Wise, M. Womble, and K. A. Young. *Anatomy & Physiology.* 2013.

[17] T. Biben, A. Farutin, and C. Misbah. Three-dimensional vesicles under shear flow: Numerical study of dynamics and phase diagram. *Phys. Rev. E*, 83(031921), 2011.

[18] T. Biben and C. Misbah. Tumbling of vesicles under shear flow within an advected-field approach. *Phys. Rev. E*, 67(031908), 2003.

[19] R. Bleischwitz, R. de Kat, and B. Ganapathisubramani. Aeromechanics of membrane and rigid wings in and out of ground-effect at moderate Reynolds numbers. *J. Fluids Struct.*, 62:318–331, 2016.

[20] G. Boedec, M. Leonetti, and M. Jaeger. 3D vesicle dynamics simulations with a linearly triangulated surface. *J. Comput. Phys.*, 230:1020–1034, 2011.

[21] I. Borazjani. Fluid-structure interaction, immersed boundary-finite element method simulations of bio-prosthetic heart valves. *Comput. Meth. Appl. Mech. Eng.*, 257:103–116, 2013.

[22] C. Bui, V. Lleras, and O. Pantz. Dynamics of red blood cells in 2D. *ESAIM: Proc.*, 28:182–194, 2009.

[23] J. T. Butcher, S. Tressel, T. Johnson, D. Turner, G. Sorescu, H. Jo, and R. M. Nerem. Transcriptional profiles of valvular and vascular endothelial cells reveal phenotypic differences. *Arterioscl. Throm. Vas.*, 26:69–77, 2006.

[24] J. T. Cantrell, B. W. LaCroix, and P. G. Ifju. Passive roll compensation on Micro Air Vehicles with perimeter reinforced membrane wings. *Int. J. Micro Air Veh.*, 5(3):163–177, 2013.

[25] P. Causin, J. F. Gerbeau, and F. Nobile. Added-mass effect in the design of partitioned algorithms for fluid-structure problems. *Comput. Meth. Appl. Mech. Eng.*, 194:4506–4527, 2005.

[26] I. B. Celik, U. Ghia, P. J. Roache, C. J. Freitas, H. Coleman, and P. E. Raad. Procedure for estimation and reporting of uncertainty due to discretization in cfd applications. *J. Fluids Eng.*, 130, 2008. article id 078001.

[27] J.-M. Charrier, S. Shrivastava, and R. Wu. Free and constrained inflation of elastic membranes in relation to thermoforming non-axisymmetric problems. *The Journal of Strain Analysis for Engineering Design*, 24(2):55–74, 1989.

[28] M. Chen and F. J. Boyle. Investigation of membrane mechanics using spring networks: Application to red-blood-cell modelling. *Mat. Sci. Eng. C*, 43:506–516, 2014.

[29] R. Cheng, Y. G. Lai, and K. B. Chandran. Three-dimensional fluid-structure interaction simulation of bileaflet mechanical heart valve flow dynamics. *Ann. of Biomed. Eng.*, 32(11):1471–1483, 2004.

[30] S. Chien. Shear dependence of effective cell volume as a determinant of blood viscosity. *Science*, 168:977–979, 1970.

[31] C. Chnafa. *Using image-based large-eddy simulations to investigate the intracardiac flow and its turbulent nature.* PhD thesis, Université Montpellier II, 2014.

[32] C. Chnafa, S. Mendez, R. Moreno, and F. Nicoud. *The Cardio-Circulatory System : from Modeling to Clinical Applications*, chapter Using image-based CFD to investigate the intracardiac turbulence. Springer, 2014.

[33] C. Chnafa, S. Mendez, and F. Nicoud. Multi-cycle large-eddy simulations of the flow in a left heart. In *8th Symposium on Turbulent and Shear Flow Phenomena, 28-30 August 2013, Poitiers, FRANCE*, 2013.

[34] C. Chnafa, S. Mendez, and F. Nicoud. Image-based large-eddy simulation in a realistic left heart. *Comput. Fluids*, 94:173–187, 2014.

[35] C. Chnafa, S. Mendez, and F. Nicoud. Image-based simulations show important flow fluctuations in a normal left ventricle: What could be the implications? *accepted for publication in Ann. of Biomed. Eng.*, 2016.

[36] C. Chnafa, S. Mendez, F. Nicoud, R. Moreno, S. Nottin, and I. Schuster. Image-based patient-specific simulation: a computational modelling of the human left heart haemodynamics. *Comput. Meth. Biomech. Biomed. Eng.*, 15(supp1):74–75, 2012.

[37] A. Chorin. Numerical solution of the Navier–Stokes equations. *Math. Comp.*, 22:745–762, 1968.

[38] T. Claessens, J. Degroote, J. Vierendeels, P. V. Ransbeeck, P. Segers, and P. Verdonck. *Image-Based Computational Modeling of the Human Circulatory and Pulmonary Systems*, chapter Mechanical Valve Fluid Dynamics and Thrombus Initiation, pages 437–462. Springer, 2011.

[39] G.-H. Cottet and E. Maitre. A level set method for fluid-structure interactions with immersed surfaces. *Math. Mod. Meth. App. Sc.*, 16(3):415–438, 2006.

[40] M. Dao, J. Li, and S. Suresh. Molecularly based analysis of deformation of spectrin network and human erythrocyte. *Mat. Sci. Eng. C*, 26:1232–1244, 2006.

[41] M. Dao, C. T. Lim, and S. Suresh. Mechanics of the human red blood cell deformed by optical tweezers. *J. Mech. Phys. Sol.*, 51:2259–2280, 2003.

[42] J. De Hart, F. P. T. Baaijens, G. W. M. Peters, and P. J. G. Schreurs. A computational fluid-structure interaction analysis of a fiber-reinforced stentless aortic valve. *J. Biomech.*, 36:699–712, 2003.

[43] J. De Hart, G. W. M. Peters, P. J. G. Schreurs, and F. P. T. Baaijens. A two-dimensional fluid-structure interaction model of the aortic value. *J. Biomech.*, 33:1079–1088, 2000.

[44] J. De Hart, G. W. M. Peters, P. J. G. Schreurs, and F. P. T. Baaijens. A three-dimensional computational analysis of fluid-structure interaction in the aortic valve. *J. Biomech.*, 36:103–112, 2003.

[45] J. De Hart, G. W. M. Peters, P. J. G. Schreurs, and F. P. T. Baaijens. Collagen fibers reduce stresses and stabilize motion of aortic valve leaflets during systole. *J. Biomech.*, 37:303–311, 2004.

[46] J. Degroote, P. Bruggeman, R. Haelterman, and J. Vierendeels. Stability of a coupling technique for partitioned solvers in fsi applications. *Comput. Struct.*, 86:2224–2234, 2008.

[47] S. Deng, M. Percin, B. van Oudheusden, B. Remes, and H. Bijl. Experimental investigation on the aerodynamics of a bio-inspired flexible flapping wing Micro Air Vehicle. *Int. J. Micro Air Veh.*, 6(2):105–115, 2014.

[48] V. Deplano, Y. Knapp, L. Bailly, and E. Bertrand. Flow of a blood analogue fluid in a compliant abdominal aortic aneurysm model: Experimental modelling. *J. Biomech.*, 47:1262–1269, 2014.

[49] P. Dimitrakopoulos. Analysis of the variation in the determination of the shear modulus of the erythrocyte membrane: Effects of the constitutive law and membrane modeling. *Phys. Rev. E*, 85(041917), 2012.

[50] D. E. Discher, N. Mohandas, and E. A. Evans. Molecular maps of red cell deformation: Hidden elastic and in situ connectivity. *Science*, 266:1032–1035, 1994.

[51] S. K. Doddi and P. Bagchi. Effect of inertia on the hydrodynamic interaction between two liquid capsules in simple shear flow. *Int. J. Multiph. Flow*, 34:375–392, 2008.

[52] S. K. Doddi and P. Bagchi. Lateral migration of a capsule in a plane Poiseuille flow in a channel. *Int. J. Multiph. Flow*, 34:966–986, 2008.

[53] S. K. Doddi and P. Bagchi. Three-dimensional computational modeling of multiple deformable cells flowing in microvessels. *Phys. Rev. E*, 79(046318), 2009.

[54] W. R. Dodson III and P. Dimitrakopoulos. Dynamics of strain-hardening and strain-softening capsules in strong planar extensional flows via an interfacial spectral boundary element algorithm for elastic membranes. *J. Fluid Mech.*, 641:263–296, 2009.

[55] N. D. dos Santos, J.-F. Gerbeau, and J. F. Bourgat. A partitioned fluid-structure algorithm for elastic thin valves with contact. *Comput. Meth. Appl. Mech. Eng.*, 197(19–20):1750–1761, 2008.

[56] C. Dupont, A.-V. Salsac, B. Barthès-Biesel, M. Vidrascu, and P. Le Tallec. Influence of bending resistance on the dynamics of a spherical capsule in shear flow. *Phys. Fluids*, 27(051902), 2015.

[57] C. D. Eggleton and A. S. Popel. Large deformation of red blood cell ghosts in a simple shear flow. *Phys. Fluids*, 10(8):1834–1845, 1998.

[58] E. A. Evans. New membrane concept applied to the analysis of fluid shear- and micropipette-deformed red blood cells. *Biophys. J.*, 13:941–954, 1973.

[59] E. A. Evans and Y. C. Fung. Improved measurements of the erythrocyte geometry. *Microv. Res.*, 4:335–347, 1972.

[60] C. Farhat, M. Lesoinne, and P. LeTallec. Load and motion transfer algorithms for fluid/structure interaction problems with non-matching discrete interfaces: Momentum and energy conservation, optimal discretization and application to aeroelasticity. *Comput. Meth. Appl. Mech. Eng.*, 157:95–114, 1998.

[61] C. Farhat, K. G. van der Zee, and P Geuzaine. Provably second-order time-accurate loosely-coupled solution algorithms for transient nonlinear computational aeroelasticity. *Comput. Meth. Appl. Mech. Eng.*, 195:1973–2001, 2006.

[62] A. Farutin, T. Biben, and C. Misbah. 3D numerical simulations of vesicle and inextensible capsule dynamics. *J. Comput. Phys.*, 275:539–568, 2014.

[63] D. A. Fedosov. *Multiscale Modeling of Blood Flow and Soft Matter*. PhD thesis, Brown University, 2010.

[64] D. A. Fedosov, B. Caswell, and G. E. Karniadakis. A multiscale red blood cell model with accurate mechanics, rheology, and dynamics. *Biophys. J.*, 98:2215–2225, 2010.

[65] D. A. Fedosov, B. Caswell, A. S. Popel, and G. E. Karniadakis. Blood flow and cell-free layer in microvessels. *Microcirc.*, 17:615–628, 2010.

[66] D. A. Fedosov, M. Dao, G. E. Karniadakis, and S. Suresh. Computational biorheology of human blood flow in health and disease. *Ann. of Biomed. Eng.*, 42(2):368–387, 2013.

[67] D. A. Fedosov, H. Noguchi, and G. Gompper. Multiscale modeling of blood flow: from single cells to blood rheology. *Biomech. Model. Mechanobiol.*, 13:239–258, 2014.

[68] D. A. Fedosov, W. Pan, B. Caswell, G. Gompper, and G. E. Karniadakis. Predicting human blood viscosity in silico. *Proc. Natl Acad. Sc. USA*, 108(29):11772–11777, 2011.

[69] D. A. Fedosov, M. Peltomäki, and G. Gompper. Deformation and dynamics of red blood cells in flow through cylindrical microchannels. *Soft Mat.*, 10:4258–4267, 2014.

[70] M. A. Fernandez and J.-F. Gerbeau. *Cardiovascular Mathematics. Modeling and simulation of the circulatory system*, volume 1 of *Modeling, Simulation and Applications*, chapter Algorithms for fluid-structure interaction problems, pages 307–346. Springer, 2009.

[71] M. A. Fernandez, J.-F. Gerbeau, and C. Grandmont. A projection semi-implicit scheme for the coupling of an elastic structure with an incompressible fluid. *Int. J. Numer. Meth. Eng.*, 69(4):794–821, 2007.

[72] C. I. Fisher, J. Chen, and W. D. Merryman. Calcific nodule morphogenesis by heart valve interstitial cells is strain dependent. *Biomech. Model. Mechanobiol.*, 12(1):5–17, 2013.

[73] T. Gao and H. H. Hu. Deformation of elastic particles in viscous shear flow. *J. Comput. Phys.*, 228:2132–2151, 2009.

[74] Z. B. Gao, S. Pandya, N. Hosein, M. S. Sacks, and N. H. C. Hwang. Bioprosthetic heart valve leaflet motion monitored by dual camera stereo photogrammetry. *J. Biomech.*, 33:199–207, 2000.

[75] L. Ge, L. P. Dasi, F. Sotiropoulos, and A. P. Yoganathan. Characterization of hemodynamic forces induced by mechanical heart valves: Reynolds vs. viscous stresses. *Ann. of Biomed. Eng.*, 36(2):276–297, 2007.

[76] L. Ge, H.-L. Leo, F. Sotiropoulos, and A. P. Yoganathan. Flow in a mechanical bileaflet heart valve at laminar and near-peak systole flow rates: CFD simulations and experiments. *J. Biomech. Eng.*, 127(5):782–797, 2005.

[77] G. Ghigliotti, T. Biben, and C. Misbah. Rheology of a dilute two-dimensional suspension of vesicles. *J. Fluid Mech.*, 653:489–518, 2010.

[78] E. Gibaud. *Numerical simulation of red blood cells flowing in a blood analyzer.* PhD thesis, Université de Montpellier, 2015.

[79] E. Gibaud, S. Mendez, D. Isèbe, and F. Nicoud. Numerical modelling of the dynamics of isolated red blood cells flowing in a cytometer. In *6th European Conference on Computational Fluid Dynamics (WCCM XI - ECCM V - ECFD VI), Barcelona, SPAIN, 20-25 July 2014.*, 2014.

[80] E. Gibaud, J. Sigüenza, S. Mendez, and F. Nicoud. Towards numerical prediction of red blood cells dynamics within a cytometer. *Comput. Meth. Biomech. Biomed. Eng.*, 16(supp1):9–10, 2013.

[81] F. J. H. Gijsen, F. N. van de Vosse, and J. D. Janssen. The influence of the non-Newtonian properties of blood on the flow in large arteries: steady flow in a carotid bifurcation model. *J. Biomech.*, 32(6):601–608, 1999.

[82] A. Gilmanov, T. B. Le, and F. Sotiropoulos. A numerical approach for simulating fluid structure interaction of flexible thin shells undergoing arbitrarily large deformations in complex domains. *J. Comput. Phys.*, 300:814–843, 2015.

[83] B. E. Griffith. Immersed boundary model of aortic heart valve dynamics with physiological driving and loading conditions. *Int. J. Numer. Meth. Biomed. Eng.*, 28:317–345, 2012.

[84] B. E. Griffith, R. D. Hornung, D. M. McQueen, and C. S. Peskin. An adaptive, formally second order accurate version of the immersed boundary method. *J. Comput. Phys.*, 223:10–49, 2007.

[85] B. E. Griffith, X. Luo, D. M. McQueen, and C. S. Peskin. Simulating the fluid dynamics of natural and prosthetic heart valves using the immersed boundary method. *Int. J. of Appl. Mech.*, 1(1):137–177, 2009.

[86] C. Guivier, V. Deplano, and Pibarot. P. New insights into the assessment of the prosthetic valve performance in the presence of subaortic stenosis through a fluid-structure interaction model. *J. Biomech.*, 40:2283–2290, 2007.

[87] C. Guivier-Curien, V. Deplano, and E. Bertrand. Validation of a numerical 3-D fluid-structure interaction model for a prosthetic valve based on experimental PIV measurements. *Med. Eng. Phys.*, 31:986–993, 2009.

[88] W. Helfrich. Elastic properties of lipid bilayers: Theory and possible experiments. *Z. Naturforsch*, 28 c:693–703, 1973.

[89] S. Hénon. A new determination of the shear modulus of the human erythrocyte membrane using optical tweezers. *Biophys. J.*, 76:1145–1151, 1999.

[90] G. Hou, J. Wang, and A. Layton. Numerical methods for fluid-structure interaction – A review. *Commun. Comput. Phys.*, 12(2):337–377, 2012.

[91] M-C. Hsu, D. Kamensky, Y. Bazilevs, M. S. Sacks, and T. J. R. Hughes. Fluid-structure interaction analysis of bioprosthetic heart valves: significance of arterial wall deformation. *Comput. Mech.*, 54:1055–1071, 2014.

[92] M-C. Hsu, D. Kamensky, F. Xu, J. Kiendl, C. Wang, M. C. H. Wu, J. Mineroff, A. Reali, Y. Bazilevs, and M. S. Sacks. Dynamic and fluid-structure interaction simulations of bioprosthetic heart valves using parametric design with T-splines and Fung-type material models. *Comput. Mech.*, 55:1211–1225, 2015.

[93] B. Hübner, E. Walhorn, and D. Dinkler. A monolithic approach to fluid-structure interaction using space-time finite elements. *Comput. Meth. Appl. Mech. Eng.*, 193:2087–2104, 2004.

[94] J. C. R. Hunt, A. A. Wray, and P. Moin. Eddies, streams, and convergence zones in turbulent flows. In *Proc. of the Summer Program, Stanford NASA C.T.R*, pages 193–208, 1988.

[95] W. R. Jamieson, L. H. Burr, W. N. Anderson Jr., J. B. Chambers, J. P. Gams, and C. M. Dowd. Prosthesis-related complications: first-year annual rates. *J. Heart Valve Dis.*, 11:758–763, 2002.

[96] D. Kamensky, M-C. Hsu, D. Schillinger, J. A. Evans, A. Aggarwal, Y. Bazilevs, M. S. Sacks, and T. J. R. Hughes. An immersogeometric variational framework for fluid-structure interaction: Application to bioprosthetic heart valves. *Comput. Meth. Appl. Mech. Eng.*, 284:1005–1053, 2015.

[97] N. Kasagi and A. Matsunaga. Three-dimensional particle-tracking velocimetry measurement of turbulence statistics and energy budget in a backward-facing step flow. *Int. J. Heat Fluid Flow*, 16:477–485, 1995.

[98] A. Kheradvar, E. M. Groves, A. Falahatpisheh, M. K. Mofrad, S. H. Alavi, R. Tranquillo, L. P. Dasi, C. A. Simmons, K. J. Grande-Allen, C. J. Goergen, F. Baaijens, S. H. Little, S. Canic, and B. Griffith. Emerging trends in heart valve engineering: Part iv. computational modeling and experimental studies. *Ann. of Biomed. Eng.*, 43(10):2314–2333, 2015.

[99] Y. Kim and M.-C. Lai. Simulating the dynamics of inextensible vesicles by the penalty immersed boundary method. *J. Comput. Phys.*, 229:4840–4853, 2010.

[100] T. Klöppel and W. A. Wall. A novel two-layer, coupled finite element approach for modeling the nonlinear elastic and viscoelastic behavior of human erythrocytes. *Biomech. Model. Mechanobiol.*, 10:445–459, 2011.

[101] D. N. Ku. Blood flow in arteries. *Ann. Rev. Fluid Mech.*, 29:399–434, 1997.

[102] U. Küttler and W. A. Wall. Fixed-point fluid-structure interaction solvers with dynamic relaxation. *Comput. Mech.*, 43:61–72, 2008.

[103] A. Laadhari, P. Saramito, and C. Misbah. Vesicle tumbling inhibited by inertia. *Phys. Fluids*, 24:031901, 2012.

[104] E. Lac, D. Barthès-Biesel, N. A. Pelekasis, and J. Tsamopoulos. Spherical capsules in three-dimensional unbounded Stokes flows: effect of the membrane constitutive law and onset of buckling. *J. Fluid Mech.*, 516:303–334, 2004.

[105] E. Lac, A. Morel, and D. Barthès-Biesel. Hydrodynamic interaction between two identical capsules in simple shear flow. *J. Fluid Mech.*, 573:149–169, 2007.

[106] A. Larroque. Haemodynamic simulations in a total artificial heart. Master's thesis, Institut Montpelliérain Alexander Grothendieck, 2015.

[107] D.-V. Le. Large deformation of liquid capsules enclosed by thin shells immersed in the fluid. *J. Comput. Phys.*, 229:4097–4116, 2010.

[108] D.-V. Le. Subdivision elements for large deformation of liquid capsules enclosed by thin shells. *Comput. Meth. Appl. Mech. Eng.*, 199:2622–2632, 2010.

[109] D.-V. Le and K.-H. Chiam. Hydrodynamic interaction between two nonspherical capsules in shear flow. *Phys. Rev. E*, 84(056322), 2011.

[110] D.-V. Le, B. C. Khoo, and J. Peraire. An immersed interface method for viscous incompressible flows involving rigid and flexible boundaries. *J. Comput. Phys.*, 220:109–138, 2006.

[111] D. V. Le, J. White, J. Peraire, K. M. Lim, and B. C. Khoo. An implicit immersed boundary method for three-dimensional fluid-membrane interactions. *J. Comput. Phys.*, 228:8427–8445, 2009.

[112] L. Lee and R. J. Leveque. An immersed interface method for incompressible Navier–Stokes equations. *SIAM J. Sci. Comput.*, 25(3):832–856, 2003.

[113] G. Lenormand, S. Hénon, A. Richet, J. Siméon, and F. Gallet. Direct measurement of the area expansion and shear moduli of the human red blood cell membrane skeleton. *Biophys. J.*, 81:43–56, 2001.

[114] J. Li, M. Dao, C. T. Lim, and S. Suresh. Spectrin-level modeling of the cytoskeleton and optical tweezers stretching of the erythrocyte. *Biophys. J.*, 88:3707–3719, 2005.

[115] G. H. W. Lim, M. Wortiz, and R. Mukhopadhyay. Stomatocyte-discocyte-echinocyte sequence of the human red blood cell: Evidence for the bilayer-couple hypothesis from membrane mechanics. *Proc. Natl Acad. Sc. USA*, 99(26):16766–16769, 2002.

[116] G. H. W. Lim, M. Wortiz, and R. Mukhopadhyay. *Red Blood Cell Shapes and Shape Transformations: Newtonian Mechanics of a Composite Membrane*, volume Lipid Bilayers and Red Blood Cells of *Soft Matter*, chapter 2, pages 94–269. WILEY-VCH Verlag GmbH & Co. KGaA, 2008.

[117] W. K. Liu, S. Jun, and Y. F. Zhang. Reproducing kernel particle methods. *Int. J. Numer. Meth. Fluids*, 20:1081–1106, 1995.

[118] W. K. Liu, D.-W. Kim, and S. Tang. Mathematical foundations of the immersed finite element method. *Comput. Mech.*, 39:211–222, 2007.

[119] W. K. Liu, Y. Liu, D. Farrell, L. Zhang, X. S. Wang, Y. Fukui, N. Patankar, Y. Zhang, C. Bajaj, J. Lee, J. Hong, X. Chen, and H. Hsu. Immersed finite element method and its applications to biological systems. *Comput. Meth. Appl. Mech. Eng.*, 195:1722–1749, 2006.

[120] E. Loiseau, G. Massiera, S. Mendez, P. Aguilar Martinez, and M. Abkarian. Microfluidic study of enhanced deposition of sickle cells at acute corners. *Biophys. J.*, 108:2623–2632, 2015.

[121] E. Maitre, T. Milcent, G.-H. Cottet, A. Raoult, and Y. Usson. Applications of level set methods in computational biophysics. *Math. Comput. Mod.*, 49(11–12):2161–2169, 2009.

[122] M. Malandain. *Simulation massivement parallèle des écoulement turbulents à faible nombre de Mach.* PhD thesis, Institut National des Sciences Appliquée de Rouen, 2012.

[123] M. Malandain, N. Maheu, and V. Moureau. Optimization of the deflated conjugate gradient algorithm for the solving of elliptic equations on massively parallel machines. *J. Comput. Phys.*, 238:32–47, 2013.

[124] M. Martins Afonso, S. Mendez, and F. Nicoud. On the damped oscillations of an elastic quasi-circular membrane in a two-dimensional incompressible fluid. *J. Fluid Mech.*, 746:300–331, 2014.

[125] J. L. McWhirter, H. Noguchi, and G. Gompper. Flow-induced clustering and alignment of vesicles and red blood cells in microcapillaries. *Proc. Natl Acad. Sc. USA*, 106(15):6039–6043, 2009.

[126] J. L. McWhirter, H. Noguchi, and G. Gompper. Deformation and clustering of red blood cells in microcapillary flows. *Soft Mat.*, 7:10967–10977, 2011.

[127] S. Mendez, C. Chnafa, E. Gibaud, J. Sigüenza, V. Moureau, and F. Nicoud. YALES2BIO: a computational fluid dynamics software dedicated to the prediction of blood flows in biomedical devices. In *5th International Conference on Biomedical Engineering in Vietnam*, volume 46 of *IFMBE Proceedings Series*, pages 7–10, 2015.

[128] S. Mendez, E. Gibaud, and F. Nicoud. An unstructured solver for simulations of deformable particles in flows at arbitrary Reynolds numbers. *J. Comput. Phys.*, 256(1):465–483, 2014.

[129] C. Michler, S. J. Hulshoff, E. H. van Brummelen, and R. de Borst. A monolithic approach to fluid-structure interaction. *Comput. Fluids*, 33:839–848, 2004.

[130] J. D. Miller, R. M. Weiss, and D. D. Heistad. Calcific aortic valve stenosis: methods, models, and mechanisms. *Circ. Res.*, 108(11):1392–1412, 2011.

[131] J. P. Mills, L. Qie, M. Dao, C. T. Lim, and S. Suresh. Nonlinear elastic and viscoelastic deformation of the human red blood cell with optical tweezers. *Mech. Chem. Biosys.*, 1(3):169–180, 2004.

[132] C. Misbah. Vesicles, capsules and red blood cells under flow. *J. Phys.: Conf. Series*, 392:012005, 2012.

[133] M. Misfeld and H.-H. Sievers. Heart valve macro- and microstructure. *Phil. Trans. R. Soc. B*, 362:1421–1436, 2007.

[134] N. Mohandas and E. A. Evans. Mechanical properties of the red cell membrane in relation to molecular structure and genetic defects. *Ann. Rev. Biophys. Biomol. Struct.*, 23:787–818, 1994.

[135] N. Mohandas and P. G. Gallagher. Red cell membrane: past, present, and future. *Blood*, 112(10):3939–3948, 2008.

[136] B. Moore and L. P. Dasi. Spatiotemporal complexity of the aortic sinus vortex. *Exp. Fluids*, 55:1770, 2014.

[137] Y. S. Morsi, I. E. Birchall, and F. L. Rosenfeldt. Artificial aortic valves: an overview. *Int. J. Artif. Organs*, 27:445–451, 2004.

[138] Y. S. Morsi and C. S. Wong. Current developments and future challenges for the creation of aortic heart valve. *J. Mech. Med. Biol.*, 8(1):1–15, 2008.

[139] V. Moureau and O. Desjardins. A second-order ghost-fluid method for the primary atomization of liquid fuel in air-blast type injectors. In *Center for Turbulence Research. Proceedings of the Summer Program 2008*, 2008.

[140] V. Moureau, P. Domingo, and L. Vervisch. Design of a massively parallel CFD code for complex geometries. *Comp. Rend. Méc.*, 339(2-3):141–148, 2011.

[141] V. Moureau, P. Domingo, and L. Vervisch. From large-eddy simulation to direct numerical simulation of a lean premixed swirl flame: Filtered laminar flame-PDF modelling. *Combust. Flame*, 158:1340–1357, 2011.

[142] F. Nicoud, H. Baya Toda, O. Cabrit, S. Bose, and J. Lee. Using singular values to build a subgrid-scale model for large eddy simulations. *Phys. Fluids*, 23(085106), 2011.

[143] F. Nicoud and T. Schönfeld. Integral boundary conditions for unsteady biomedical CFD applications. *Int. J. Numer. Meth. Fluids*, 40:457–465, 2002.

[144] H. Noguchi and G. Gompper. Fluid vesicles with viscous membranes in shear flow. *Phys. Rev. Lett.*, 93(258102), 2004.

[145] H. Noguchi and G. Gompper. Dynamics of fluid vesicles in shear flow: Effect of membrane viscosity and thermal fluctuations. *Phys. Rev. E*, 72(011901), 2005.

[146] H. Noguchi and G. Gompper. Shape transitions of fluid vesicles and red blood cells in capillary flows. *Proc. Natl Acad. Sc. USA*, 102(40):14159–14164, 2005.

[147] H. Noguchi and G. Gompper. Swinging and tumbling of fluid vesicles in shear flow. *Phys. Rev. Lett.*, 98:128103, 2007.

[148] W. Pan, B. Caswell, and G. E. Karniadakis. A low-dimensional model for the red blood cell. *Soft Mat.*, 6:4366–4376, 2010.

[149] Z. Peng, R. J. Asaro, and Q. Zhu. Multiscale modelling of erythrocytes in Stokes flow. *J. Fluid Mech.*, 686:299–337, 2011.

[150] C. S. Peskin. Numerical analysis of blood flow in the heart. *J. Comput. Phys.*, 25:220–252, 1977.

[151] C. S. Peskin. The fluid dynamics of heart valves: Experimental, theoretical, and computational methods. *Ann. Rev. Fluid Mech.*, 14:235–259, 1982.

[152] C. S. Peskin. The immersed boundary method. *Acta Num.*, 11:479–517, 2002.

[153] A. Pinelli, I. Z. Naqavi, U. Piomelli, and J. Favier. Immersed-boundary methods for general finite-difference and finite-volume Navier–Stokes solvers. *J. Comput. Phys.*, 229:9073–9091, 2010.

[154] I. V. Pivkin and G. E. Karniadakis. Accurate coarse-grained modeling of red blood cells. *Phys. Rev. Lett.*, 101(118105), 2008.

[155] C. Pozrikidis. *Boundary Integral and Singularity Methods for Linearized Viscous Flow.* Cambridge University Press., 1992.

[156] C. Pozrikidis. Numerical simulation of the flow-induced deformation of red blood cells. *Ann. of Biomed. Eng.*, 31:1194–1205, 2003.

[157] F. Radjai and F. Dubois, editors. *Discrete Numerical Modeling of Granular Materials.* Wiley-ISTE, 2011.

[158] S. Ramanujan and C. Pozrikidis. Deformation of liquid capsules enclosed by elastic membranes in simple shear flow: large deformations and the effect of fluid viscosities. *J. Fluid Mech.*, 361:117–143, 1998.

[159] A. Ranga, O. Bouchot, R. Mongrain, P. Ugolini, and R. Cartier. Computational simulations of the aortic valve validated by imaging data: evaluation of valve-sparing techniques. *Interact. CardioVasc. Thorac. Surg.*, 5:373–378, 2006.

[160] H. Reul, A. Vahlbruch, M. Giersiepen, T. Schmitz-Rode, V. Hirtz, and S. Effert. The geometry of the aortic root in health, at valve disease and after valve replacement. *J. Biomech.*, 23(2):181–191, 1990.

[161] A. M. Robertson, A. Sequeira, and R. G. Owens. *Cardiovascular Mathematics. Modeling and simulation of the circulatory system*, volume 1 of *Modeling, Simulation and Applications*, chapter Rheological models for blood, pages 211–241. Springer, 2009.

[162] P. Rojratsirikul, Z. Wang, and I. Gursul. Effect of pre-strain and excess length on unsteady fluid-structure interactions of membrane airfoils. *J. Fluids Struct.*, 26:359–376, 2010.

[163] P. B. Ryzhakov, R. Rossi, S. R. Idelsohn, and E. Oñate. A monolithic lagrangian approach for fluid-structure interaction problems. *Comput. Mech.*, 46:883–899, 2010.

[164] M. S. Sacks, W. D. Merryman, and D. E. Schmidt. On the biomechanics of heart valve function. *J. Biomech.*, 42:1804–1824, 2009.

[165] D. Salac and M. Miksis. A level set projection model of lipid vesicles in general flows. *J. Comput. Phys.*, 230:8192–8215, 2011.

[166] M. Schäfer, M. Heck, and S. Yigit. *Fluid-Structure Interaction: Modelling, Simulation, Optimisation*, volume 53, chapter An Implicit Partitioned Method for the Numerical Simulation of Fluid-Structure Interaction, pages 171–194. Springer, 2006.

[167] K. Schenke-Layland, U. A. Stock, A. Nsair, J. Xie, E. Angelis, C. G. Fonseca, R. Larbig, A. Mahajan, M. C. Shivkumar, K. Fishbein, and W. R. MacLellan. Cardiomyopathy is associated with structural remodelling of heart valve extracellular matrix. *Eur. Heart J.*, 30:2254–2265, 2009.

[168] J. Sigüenza, S. Mendez, D. Ambard, F. Dubois, F. Jourdan, R. Mozul, and F. Nicoud. Validation of an immersed thick boundary method for simulating fluid-structure interactions of deformable membranes. *J. Comput. Phys.*, 322:723–746, 2016.

[169] J. Sigüenza, S. Mendez, and F. Nicoud. Characterisation of a dedicated mechanical model for red blood cells: numerical simulations of optical tweezers experiment. *Comput. Meth. Biomech. Biomed. Eng.*, 17(supp. 1):28–29, 2014.

[170] J. Sigüenza, S. Mendez, and F. Nicoud. How should the optical tweezers experiment be used to characterize the red blood cell membrane mechanics? Submitted in Biomech. Model. Mechanobiol., 2016.

[171] J. Sigüenza, D. Pott, S. Mendez, S. Sonntag, U. Steinseifer, and F. Nicoud. A combined experimental and numerical study of a polymeric aortic valve model. Submitted to Cardiov. Eng. Tech., 2016.

[172] J. C. Simo and K. S. Pister. Remarks on rate constitutive equations for finite deformation problems: computational implications. *Comput. Meth. Appl. Mech. Eng.*, 46:201–215, 1984.

[173] K. Sinha and M. D. Graham. Dynamics of a single red blood cell in simple shear flow. *Phys. Rev. E*, 92(042710), 2015.

[174] R. Skalak, A. Tozeren, R. P. Zarda, and S. Chien. Strain energy function of red blood cell membranes. *Biophys. J.*, 13:245–264, 1973.

[175] K. E. Smith, S. A. Metzler, and J. N. Warnock. Cyclic strain inhibits acute pro-inflammatory gene expression in aortic valve interstitial cells. *Biomech. Model. Mechanobiol.*, 9(1):117–125, 2010.

[176] F. Sotiropoulos, T. B. Le, and A. Gilmanov. Fluid mechanics of heart valves and their replacements. *Ann. Rev. Fluid Mech.*, 48:259–83, 2016.

[177] D. C. Sternel, M. Schäfer, M. Heck, and S. Yigit. Efficiency and accuracy of fluid-structure interaction simulations using an implicit partitioned approach. *Comput. Mech.*, 43:103–113, 2008.

[178] P. Sucosky, K. Balachandran, A. Elhammali, H. Jo, and A. P. Yoganathan. Elevated cyclic stretch alters matrix remodeling in aortic valve cusps: implications for degenerative aortic valve disease. *Arterioscl. Throm. Vas.*, 29:254–260, 2009.

[179] Y. Sui, X. B. Chen, Y. T. Chew, P. Roy, and H. T. Low. Numerical simulation of capsule deformation in simple shear flow. *Comput. Fluids*, 39:242–250, 2010.

[180] Y. Sui, Y. T. Chew, P. Roy, Y. P. Cheng, and H. T. Low. Dynamic motion of red blood cells in simple shear flow. *Phys. Fluids*, 20(112106), 2008.

[181] Y. Sui, H. T. Low, Y. T. Chew, and P. Roy. Tank-treading, swinging, and tumbling of liquid-filled elastic capsules in shear flow. *Phys. Rev. E*, 77(016310), 2008.

[182] L. Sun, S. Chandra, and P. Sucosky. Ex vivo evidence for the contribution of hemodynamic shear stress abnormalities to the early pathogenesis of calcific bicuspid aortic valve disease. *PLoS One*, 7(10):e48843, 2012.

[183] T. Sun and H. Morgan. Single-cell microfluidic impedance cytometry: a review. *Microfluid. Nanofluid.*, 8:423–443, 2010.

[184] G. B. K. Sundaram, K. R. Balakrishnan, and R. K. Kumar. Aortic valve dynamics using a fluid structure interaction model - The physiology of opening and closing. *J. Biomech.*, 48:1737–1744, 2015.

[185] S. Suresh, J. Spatz, J. P. Mills, A. Micoulet, M. Dao, C. T. Lim, M. Beil, and T. Seufferlein. Connections between single-cell biomechanics and human disease states: gastrointestinal cancer and malaria. *Acta Biomaterialia*, 1:15–30, 2005.

[186] K. Y. Sze, X. H. Liu, and S. H. Lo. Popular benchmark problems for geometric nonlinear analysis of shells. *Finite Elem. Anal. Des.*, 40:1551–1569, 2004.

[187] S. Turek and J. Hron. *Fluid-Structure Interaction: Modelling, Simulation, Optimisation*, volume 53, chapter Proposal for numerical benchmarking of fluid-structure interaction between an elastic object and laminar incompressible flow, pages 371–385. Springer, 2006.

[188] S. Turek, J. Hron, M. Razzaq, H. Wobker, and M. Schäfer. *Fluid-Structure Interaction II - Modelling, Simulation, Optimization*, volume 73, chapter Numerical Benchmarking of Fluid-Structure Interaction: A Comparison of Different Discretization and Solution Approaches, pages 413–424. Springer, 2010.

[189] Stijn Vantieghem. *Numerical simulations of quasi-static magnetohydrodynamics using an unstructured finite volume solver: development and applications.* PhD thesis, Université Libre de Bruxelles, 2011.

[190] S. K. Veerapaneni, D. Gueyffier, D. Zorin, and G. Biros. A boundary integral method for simulating the dynamics of inextensible vesicles suspended in a viscous fluid in 2D. *J. Comput. Phys.*, 228:2334–2353, 2009.

[191] J. Vierendeels, K. Dumont, and P. R. Verdonck. A partitioned strongly coupled fluid-structure interaction method to model heart valve dynamics. *J. Comput. Appl. Math.*, 215:602–609, 2008.

[192] A. M. Walker, C. R. Johnston, and Rival D. E. On the characterization of a non-Newtonian blood analog and its response to pulsatile flow downstream of a simplified stenosis. *Ann. of Biomed. Eng.*, 2013.

[193] W. A. Wall, D. P. Mok, and E. Ramm. Partitioned analysis approach of the transient coupled response of viscous fluids and flexible structures. In W. Wunderlich, editor, *Solids, Structures and Coupled Problems in Engineering, Proc. ECCM '99. Munich, August/September 1999*, 1999.

[194] J. Walter, A.-V. Salsac, D. Barthès-Biesel, and P. Le Tallec. Coupling of finite element and boundary integral methods for a capsule in a Stokes flow. *Int. J. Numer. Meth. Eng.*, 83:829–850, 2010.

[195] X. Wang and W. K. Liu. Extended immersed boundary method using FEM and RKPM. *Comput. Meth. Appl. Mech. Eng.*, 193:1305–1321, 2004.

[196] X. S. Wang. An iterative matrix-free method in implicit immersed boundary/continuum methods. *Comput. Struct.*, 85:739–748, 2007.

[197] X. S. Wang. *Computational Modeling in Biomechanics*, chapter Immersed Boundary/Continuum Methods, pages 3–48. Springer, 2010.

[198] P. N. Watton, X. Y. Luo, X. Wang, G. M. Bernacca, P. Molloy, and D. J. Wheatley. Dynamic modelling of prosthetic chorded mitral valves using the immersed boundary method. *J. Biomech.*, 40:613–626, 2007.

[199] E. J. Weinberg and M. R. K. Mofrad. Transient, three-dimensional, multiscale simulations of the human aortic valve. *Cardiov. Eng.*, 7:140–155, 2007.

[200] E. J. Weinberg and M. R. K. Mofrad. A multiscale computational comparison of the bicuspid and tricuspid aortic valves in relation to calcific aortic stenosis. *J. Biomech.*, 41:3482–3487, 2008.

[201] J. H. Williamson. Low-storage Runge-Kutta schemes. *J. Comput. Phys.*, 35:48–56, 1980.

[202] C. Wood, A. J. Gil, O. Hassan, and J. Bonet. Partitioned block-Gauss-Seidel coupling for dynamic fluid-structure interaction. *Comput. Struct.*, 88:1367–1382, 2010.

[203] H. C. Woolfenden and M. G. Blyth. Motion of a two-dimensional elastic capsule in a branching channel flow. *J. Fluid Mech.*, 669:3–31, 2011.

[204] Y. Xing, J. N. Warnock, Z. He, S. L. Hilbert, and A. P. Yoganathan. Cyclic pressure affects the biological properties of porcine aortic valve leaflets in a magnitude and frequency dependent manner. *Ann. of Biomed. Eng.*, 32(11):1461–1470, 2004.

[205] C. H. Yap, N. Saikrishnan, G. Tamilselvan, and A. P. Yoganathan. Experimental measurement of dynamic fluid shear stress on the aortic surface of the aortic valve leaflet. *Biomech. Model. Mechanobiol.*, 11:171–182, 2012.

[206] A. Z. K. Yazdani and P. Bagchi. Influence of membrane viscosity on capsule dynamics in shear flow. *J. Fluid Mech.*, 718:569–595, 2013.

[207] O. H. Yeoh. Some forms of the strain energy function for rubber. *Rubber Chem. Technol.*, 66(5):754–771, 1993.

[208] A. P. Yoganathan, Z. He, and S. C. Jones. Fluid mechanics of heart valves. *Ann. Rev. Biomed. Eng.*, 6:331–62, 2004.

[209] L. Zhang, A. Gerstenberger, X. Wang, and W. K. Liu. Immersed finite element method. *Comput. Meth. Appl. Mech. Eng.*, 193:2051–2067, 2004.

[210] L. T. Zhang and M. Gay. Immersed finite element method for fluid-structure interactions. *J. Fluids Struct.*, 23:839–857, 2007.

[211] W. Zhang, Y. Jiang, and Z. Ye. Two better loosely coupled solution algorithms of cfd based aeroelastic simulation. *Eng. Appl. Comp. Fluid*, 1(4):253–262, 2007.

[212] H. Zhao, A. H. G. Isfahani, L. N. Olson, and J. B. Freund. A spectral boundary integral method for flowing blood cells. *J. Comput. Phys.*, 229:3726–3744, 2010.

[213] H. Zhao and E. S. G. Shaqfeh. The dynamics of a vesicle in simple shear flow. *J. Fluid Mech.*, 674:578–604, 2011.

[214] O. Y. Zhong-can and W. Helfrich. Bending energy of vesicle membranes: General expressions for the first, second, and third variation of the shape energy and applications to spheres and cylinders. *Phys. Rev. A*, 39(10):5280–5288, 1989.

[215] V. Zmijanovic, S. Mendez, V. Moureau, and F. Nicoud. About the numerical robustness of biomedical benchmark cases: Interlaboratory FDA's idealized medical device. *accepted for publication in Int. J. Numer. Meth. Biomed. Eng.*, 2016.